



**University of  
Zurich**<sup>UZH</sup>

# Experimental Approach for Quantifying Operator and Protocol Related Uncertainties of Field Spectroscopy Measurements

GEO 511 Master's Thesis

**Author**

Carmen Meiller  
14-703-177

**Supervised by**

Dr. Andreas Hüni

**Faculty representative**

Prof. Dr. Meredith Christine Schuman

29.04.2021

Department of Geography, University of Zurich



**University of  
Zurich**<sup>UZH</sup>

DEPARTMENT OF GEOGRAPHY  
REMOTE SENSING LABORATORIES — RSL

MSC THESIS — SPRING SEMESTER 2021

---

**Experimental Approach for Quantifying  
Operator and Protocol Related  
Uncertainties of Field Spectroscopy  
Measurements**

---

*Author:*  
Carmen MEILLER  
carmen.meiller@uzh.ch  
14-703-177

*Supervisor:*  
Dr. Andreas HUENI  
ahueni@geo.uzh.ch

*Faculty member:*  
Prof. Dr. Meredith C. SCHUMAN

April 2021

# Contents

|          |   |           |
|----------|---|-----------|
| <b>1</b> | <b>Introduction</b>   | <b>1</b>  |
| 1.1      | Scientific Relevance . . . . .  | 1         |
| 1.2      | Field Spectroscopy . . . . .  | 2         |
| 1.3      | Uncertainty . . . . .   | 3         |
| 1.3.1    | Work Flow of the Assessment of Uncertainty . . . . .  | 3         |
| 1.4      | Uncertainty in Field Spectroscopy: State of the Art and Motivation . . . . .                                    | 9         |
| 1.5      | Terminology . . . . .   | 11        |
| <b>2</b> | <b>Experiments</b>  | <b>12</b> |
| 2.1      | Introduction to the Experiments . . . . .   | 12        |
| 2.2      | Performed Experiments . . . . .   | 13        |
| 2.3      | Used Devices and Setup . . . . .  | 14        |
| 2.3.1    | Field Spectroradiometers . . . . .  | 14        |
| 2.3.2    | White Reference Panel . . . . .   | 16        |
| 2.4      | Default Setup . . . . .   | 17        |
| <b>3</b> | <b>Introduction to the Exemplary Experiment: Distance From the Fibre Optic Tip to the White Reference Panel</b> | <b>20</b> |
| <b>4</b> | <b>Research Questions and Hypotheses</b>  | <b>21</b> |
| <b>5</b> | <b>Method</b>   | <b>23</b> |
| 5.1      | Experimental Setup and Procedure . . . . .  | 23        |
| 5.2      | Data Analysis . . . . .   | 25        |
| 5.2.1    | Cross-Calibration of the Instruments and Panels . . . . .   | 25        |
| 5.2.2    | Correction of the Pistol Grip Offset . . . . .  | 28        |
| 5.2.3    | Correction for the Change in Solar Irradiance Over Time . . . . .   | 29        |
| 5.2.4    | <i>Excursus</i> : Broken Fibres and Bending of the Fibre Optic Cable . . . . .                                  | 31        |
| 5.2.5    | Calculation of the Correction Model . . . . .   | 32        |
| 5.3      | Propagation of Uncertainty . . . . .  | 35        |
| 5.3.1    | Uncertainty Estimation of the Cross-Calibration . . . . .   | 37        |
| 5.3.2    | Uncertainty Estimation of the Pistol Grip Offset Correction . . . . .   | 39        |
| 5.3.3    | Uncertainty Estimation of the Correction for the Solar Irradiance Change Over Time . . . . .                    | 40        |
| 5.3.4    | Uncertainty Estimation of the Correction Model . . . . .  | 42        |
| 5.3.5    | Uncertainty Estimation of the Applied Correction Model . . . . .  | 43        |
| <b>6</b> | <b>Results</b>  | <b>44</b> |
| 6.1      | Correction Model . . . . .  | 44        |
| 6.2      | Model of the Combined Standard Uncertainty . . . . .  | 50        |
| 6.3      | Goodness of Fit Evaluation of the Models . . . . .  | 54        |
| 6.4      | Applied Correction Model . . . . .  | 57        |
| <b>7</b> | <b>Discussion</b>   | <b>60</b> |
| <b>8</b> | <b>Conclusion</b>   | <b>66</b> |
| <b>9</b> | <b>Outlook</b>  | <b>69</b> |

|  |           |
|--|-----------|
| <b>Appendices</b>  | <b>77</b> |
| <b>A Correction Model: Individual Wavelength Ranges</b>                      | <b>77</b> |
| A.1 Fitted Mean Quadratic Functions of the Correction Model . . . . .        | 77        |
| A.2 Mean <i>Monte Carlo</i> Values . . . . .                                 | 79        |
| A.3 Residuals (Correction Model) . . . . .                                   | 80        |
| <b>B Uncertainty Model: Individual Wavelength Ranges</b>                     | <b>81</b> |
| B.1 Fitted Mean Quadratic Functions of the Uncertainty Model . . . . .       | 81        |
| B.2 Combined Standard Uncertainty Values for the Initial Eight Distances . . | 82        |
| B.3 Residuals (Uncertainty Model) . . . . .                                  | 83        |
| <b>C Conducted Experiments</b>   | <b>84</b> |
| C.1 Tilted Versus Levelled Reference Panel . . . . .                         | 84        |
| C.2 Distance of the Operator to the Panel . . . . .                          | 86        |
| C.3 Position of the Operator in Relation to the Sun . . . . .                | 88        |
| C.4 Rest vs. Free-Hand Operating . . . . .                                   | 89        |
| C.5 Ideal Number of Target Measurements . . . . .                            | 91        |
| C.6 Measurement Patterns for the Target Acquisition . . . . .                | 93        |
| C.7 Warm-Up of the Instrument . . . . .                                      | 94        |
| C.8 Ideal Time Frame of Acquisition . . . . .                                | 95        |

## List of Figures

|    |  |    |
|----|--|----|
| 1  | Ratio of the spectral radiances at different times during the warm-up period to the spectral radiance at the start of the experiment conducted by Hemmer and Westphal [23]. (Figure from Hemmer and Westphal [23].) . . .  | 15 |
| 2  | The design of the fibre holder used for the conducted experiments. . . . .   | 17 |
| 3  | The reference setup installed to collect spectral data. . . . .  | 18 |
| 4  | The location and setup. . . . .  | 23 |
| 5  | The data flow diagram, illustrating the main steps of the derivation of the correction model. . . . .  | 26 |
| 6  | The mean measured spectra used for the cross-calibration of the instruments and panels. . . . .  | 27 |
| 7  | Mean pre and post cross-calibration factors and mean time-interpolated cross-calibration factors per distance measurement as well as their interpolated uncertainty for the entire wavelength range of the instruments (350 - 2500 nm). . . . .  | 28 |
| 8  | Zoom (470 - 510 nm) on the mean pre and post cross-calibration factors and mean time-interpolated cross-calibration factors per distance measurement as well as their interpolated uncertainty. . . . .  | 28 |
| 9  | The reference measurement at a distance of 12 cm to the panel and the cross-calibrated experimental measurement at the same distance revealing the influence of the pistol grip. . . . .   | 29 |
| 10 | Removal of the solar irradiance change over time from the cross-calibrated and pistol grip offset corrected experiments at the exemplary wavelength 1650 nm. <i>1</i> : Reference measurements, <i>2</i> : Experimental measurements, <i>3</i> : Solar irradiance change detrended reference measurements, <i>4</i> : Solar irradiance change detrended experimental measurements. . . . . | 30 |
| 11 | Standard deviations of the test measurements obtained with the three instruments. Once the fibre optic cables were twisted by hand and once in a static state. . . . .   | 32 |
| 12 | Visualisation of the 100 first <i>Monte Carlo</i> iterations to generate the correction model at the exemplary wavelength 1650 nm (SWIR). . . . .  | 33 |
| 13 | An example of the quadratic fits applied to the <i>Monte Carlo</i> simulations: The first 100 iterations for the wavelength 1650 nm (SWIR). . . . .  | 34 |
| 14 | The tree diagram presenting the uncertainty propagation of the data analysis. . . . .  | 36 |
| 15 | The final correction model per wavelength and distance to the panel (mean fitted quadratic function) with absorption features removed. . . . .   | 44 |
| 16 | Exemplary correction model functions with their corresponding uncertainties to be applied to distances to the panel from 2 to 28 cm (UV - Orange). . . . .   | 45 |
| 17 | Exemplary correction model functions with their corresponding uncertainties to be applied to distances to the panel from 2 to 28 cm (Red - SWIR). . . . .  | 46 |
| 18 | Factors of the <i>combined standard uncertainty</i> of the correction model per wavelength (fitted quadratic functions) with absorption features removed (the black part consists of many overlapping NIR wavelengths due to the 3D structure). . . . .  | 50 |
| 19 | All statistical uncertainties of the data sets and their propagation along the data processing for a distance to the panel of 12 cm. . . . .   | 52 |
| 20 | 3D visualisation of the mean <i>Monte Carlo</i> simulations and the corresponding residuals. . . . .   | 54 |

|    |   |    |
|----|---|----|
| 21 | The <i>RMSE</i> of the eight distances to the panel per wavelength of the correction model. . . . .   | 55 |
| 22 | 3D visualisations of the propagated uncertainty values and the residuals. . . . .   | 55 |
| 23 | The <i>RMSE</i> of the eight distances to the panel per wavelength of the uncertainty model. . . . .  | 55 |
| 24 | Exemplary applied correction model functions for distances to the panel from 2 to 28 cm and their associated uncertainties (UV - orange). . . . .                             | 58 |
| 25 | Exemplary applied correction model functions for distances to the panel from 2 to 28 cm and their associated uncertainties (Red - SWIR). . . . .                              | 59 |
| 26 | The mean quadratic functions of the correction model per wavelength range accompanied by their <i>combined standard uncertainty</i> . . . . .                                 | 77 |
| 27 | The mean quadratic functions of the correction model per wavelength range accompanied by their <i>expanded uncertainty</i> . . . . .  | 78 |
| 28 | The mean <i>Monte Carlo</i> values to which the functions per wavelength range were fitted. . . . .   | 79 |
| 29 | The residuals (difference between the mean quadratic fits of the correction model and the mean <i>Monte Carlo</i> values). . . . .  | 80 |
| 30 | The mean quadratic functions of the uncertainty model per wavelength range. . . . .   | 81 |
| 31 | The initial eight <i>combined standard uncertainty</i> values to which the functions per wavelength range were fitted. . . . .  | 82 |
| 32 | The residuals (difference between the mean quadratic fits of the uncertainty model and the initial eight <i>combined standard uncertainty</i> values). . . . .                | 83 |
| 33 | A sketch of the experiment investigating potential differences between a tilted and a levelled reference panel. . . . .   | 85 |
| 34 | A sketch of the experiment that investigates potential interference effects when the operator stands in close proximity to the reference panel. . . . .                       | 87 |
| 35 | A sketch of all the operator's cardinal and intercardinal positions where the measurements were obtained, together with the azimuth position of the sun at that time. . . . . | 88 |
| 36 | The designed appliance to serve as a rest for the monopod. . . . .  | 89 |
| 37 | The experimental setup to investigate the matter of the ideal number of target measurements to be obtained. . . . .   | 91 |
| 38 | The installation of the three field spectroradiometers for the warm-up experiment and the use of the integrating sphere. . . . .  | 94 |

## List of Tables

|   |  |    |
|---|--|----|
| 1 | Selected specifications of the field spectroradiometers used [2] [3]. . . . .                                    | 14 |
| 2 | Overview of the field spectroradiometers used and their number of functioning fibres. . . . .                    | 16 |
| 3 | Summary of all specifications of the default setup. . . . .  | 19 |
| 4 | The specifications of the experimental setup. . . . .  | 22 |
| 5 | Correction to the default distance in +/- percent of the measured spectral radiance. . . . .                     | 47 |
| 6 | Mean <i>combined standard uncertainty</i> per wavelength range and distance to the panel in percent [%]. . . . . | 51 |
| 7 | The different distances to the panel at which measurements were collected.                                       | 86 |

## **Nomenclature**

ASD Analytical Spectral Devices

CCD Charge-Coupled Device

CEST Central European Summer Time

CLT Central Limit Theorem

DC Dark Current

DN Digital Number

DRF Directional Response Function

EM Electromagnetic

FOV Field Of View

GUM Guide to the Expression of Uncertainty in Measurements

HCRF Hemispherical-Conical Reflectance Factor

InGaAs Indium Gallium Arsenide

NIR Near-infrared

NIST National Institute of Standards and Technology

RMSE Root mean square error

RSL Remote Sensing Laboratories

SI International System of Units

SSE Size-of-Source Effect

SVC Spectra Vista Corporation

SWIR Short-wavelength infrared

TRUTHS Traceable Radiometry Underpinning Terrestrial- and Helio- Studies

UV Ultraviolet

VNIR Visible and near-infrared



## Abstract

The calibration and validation of airborne or space-based optical instruments (hyper- or multispectral imaging sensors) is a critical part to receive valuable and reliable Earth observation products, particularly in the context of today's changing climate. Often, such calibrations or validations are performed using ground measurements obtained with field spectroradiometers. However, field spectroscopy measurements are not as easy to obtain as is often assumed. A number of operator or protocol related errors can occur during the measurement process, introducing uncertainties to the spectral data measured. One of several potential sources of error was investigated in this study, namely the possible influence of different distances of the fibre optic tip (sensor aperture) of an *Analytical Spectral Devices FieldSpec 3* field spectroradiometer to the surface of the reference panel. An experiment was designed and conducted in which spectral data sets were acquired at heights of 2, 5, 10, 12, 15, 20, 25 and 28 cm above the panel. Simultaneously, spectral reference measurements were obtained at a predefined default distance of 12 cm to the panel. The data sets were corrected for several influencing parameters to receive the sole influence of the different distances. A correction model was calculated that normalises measurements acquired at different distances to the panel between 2 and 28 cm to the chosen default distance of 12 cm. The *combined standard uncertainty* of the correction model was calculated as well. Compared to the default distance at 12 cm, the ultraviolet and partly the violet range showed lower spectral radiance values at shorter distances to the panel and higher values at larger distances. The blue to short-wavelength infrared range returned exactly reverse values (higher values at shorter distances and lower values at greater distances). Three wavelength dependent main influences were identified: The higher sensitivity of shorter wavelengths to diffuse radiation in combination with the pistol grip covering a large fraction of the sky hemisphere (relatively stronger influence in ultraviolet, violet and partly blue) as well as the *Size-of-Source Effect* and inter-reflections (relatively stronger influence in the visible to short-wavelength infrared ranges). It was concluded that the calculated correction model adds value to field spectroscopy measurements acquired at different distances to the panel due to the correction effect being larger than the associated *combined standard uncertainty* of the applied model. The results of this study indicate the importance of the topic of operator and protocol related uncertainties in field spectroscopy and the need for further analysis of different sources of uncertainty.

# 1 Introduction

## 1.1 Scientific Relevance

One of the greatest challenges facing humankind today is the changing climate. The anthropogenic influence on the climate by the emission of a large amount of greenhouse gases leads, among other things, to severe impacts on the Earth's system [50]. Due to climate change, various threats to the world's ecosystems and hence to humankind itself have evolved, such as the loss of biodiversity, changes in the occurrence of extreme events, the rise of global mean surface and ocean temperatures or the rise of the global mean sea level [50], [58]. The emergence of such threats forces humankind to develop adaptation and/or mitigation strategies, for which detailed knowledge of processes of the Earth's system is required.

Remote sensing systems are able to monitor and measure a wide range of parameters relevant to gain information on processes related to climate change. Knowledge on land-cover changes, biodiversity metrics, time-series analyses, estimates of coral reef extents or trace gas emissions, among many others, can be provided by the various remote sensing systems [58].

Spectroscopy, as defined by the *Society of Photo-Optical Instrumentation Engineers* [8] as well as E. J. Milton [46] is the study of matter using electromagnetic (EM) radiation. The interaction of electromagnetic radiation with a target object and thus either the transmitted, absorbed or reflected radiation after hitting the target object is of interest.

Imaging spectroscopy (hyperspectral remote sensing) in particular is a powerful tool that generates data usable in many application areas such as forestry, urban areas, green house gas detection and other fields [58]. To meet the needs of climate science, the *Global Climate Observing System* has defined so called *Essential Climate Variables*, which define relevant specifications for climate-related remotely sensed data products [25].

Extracting and communicating information stemming from electromagnetic radiation measured remotely from airborne or space-based platforms enables humankind to gain knowledge in entirely new dimensions. This facilitates better understanding, better prediction and ultimately provides a tool to mitigate or prevent threats due to climate change.

It is of utmost importance when acquiring imaging spectroscopy data, that the data is of high quality. A reliable data set is characterised by the traceability to the *International System of Units (SI)* and a defined uncertainty budget [62]. This is important because a derived product that is supposed to provide accurate and reliable information on a particular topic of interest is useless if the certainty of said product is unknown. The results will not be meaningful and, in the worst case, will lead to wrong interpretations and, moreover, to wrong decisions of policymakers.

To provide high quality data, airborne and space-based data sets need to be validated by another high quality data set, e.g., using field spectroscopy measurements.

## 1.2 Field Spectroscopy

Curtiss and Goetz [15] define field spectroscopy (or spectroradiometric in-situ measurements) as “*the quantitative measurements of radiance, irradiance, reflectance or transmission in the field*” whereby portable and battery powered spectroradiometers are used to acquire the data.

Field spectroscopy measurements are often used to provide data for the vicarious calibration and/or validation of airborne or space-based measurements, but also as a research tool in its own right [27] [47]. These in-situ spectroradiometric measurements are frequently referred to as “*Ground Truth*”, which has the intrinsic meaning that they are the accurate standard against which any other measurement should be compared. However, this is not the case for any obtained measurement, as there is no such thing as “*Ground Truth*”. At most, there is a best estimate of a variable obtained as an *SI*-traceable measurement with associated uncertainty [20].

Due to the important role of field spectroscopy measurements in providing information to be used as the most accurate estimate of the true value of a target parameter, these measurements must be as precise as possible. Therefore, the measurements need to be traceable to *SI*-standards and have an associated uncertainty budget. However, obtaining reliable in-situ measurements is not as easy as is often assumed. Or in the words of the *Commonwealth Scientific and Industrial Research Organisation’s technical handbook on the collection of field reflectance data* [44]: “*It is relatively easy to get good field spectra – and easier still to get bad spectra*”.

Many sources of uncertainty can emerge while conducting spectroradiometric measurements which are often unintuitive to operators as they are not aware of their existence. A holistic evaluation of the error sources, the development of approaches for their possible correction and the calculation of associated uncertainties of field spectroscopy measurements is therefore of utmost importance. A reliable validation data set is the basis to deliver feasible products generated from any other data set. Hence, the development of a complete uncertainty budget for field spectroscopy measurements would be an extremely valuable result.

## 1.3 Uncertainty

"Knowledge is an unending  
adventure at the edge of  
uncertainty." - Jacob Bronowski  
*Mathematician and Historian*

---

The utopian goal of measuring a physical quantity with an instrument is always to obtain the true value of the object of interest. Unfortunately, the true value of anything can never be known, as all measurements are just an estimate of that real value. In the best case, measurements come very close to the true value of the desired physical quantity [28]. The difference between the true value and the result of a measurement aiming to describe the real value is denoted as the measurement error [28]. But since the true value is not known, the measurement error cannot be known either. Therefore, the error can only be estimated from the results of our measurements. This is referred to as the uncertainty of the measurements (best estimate of the error). Uncertainty is hence by definition “doubt”, which, when applied to measurements, is doubt about the validity of the result of a measurement [28]. The uncertainty always needs to be assessed and stated with every measurement obtained, in order to provide an accurate quality statement about the value of the measured physical quantity.

A thorough calculation of uncertainties and their propagation is a process that can be done almost ad infinitum, which is why compromises have to be made. For the subsequent data and uncertainty analysis (Section 3), an attempt was made to find a good balance between accuracy, usefulness and time expenditure.

### 1.3.1 Work Flow of the Assessment of Uncertainty

This section will describe a general work flow on how to assess uncertainties following the general guide lines of the international *Guide to the Expression of Uncertainty in Measurements (GUM)* [28] and its supplements. The intention of this section is to provide a better understanding of the assessment of uncertainties of the obtained experimental measurements, which will be described subsequently.

As a general definition, the *GUM* assumes that any measurement whose uncertainty is to be determined can be modelled mathematically. This means that a function can be specified that describes the measured physical quantity. With the existence of a mathematical function, the *Gaussian* law of uncertainty propagation can be applied [28].

According to the *GUM*, there are two types into which uncertainties can be categorised: A) those that can be evaluated by statistical methods and B) those that need to be evaluated by other means [28]. Often, these two categories are also referred to as “random” (A) and “systematic” (B) uncertainties. However, the use of the latter two terms is not recommended by the *GUM*, as “systematic” uncertainty can be misleading and does not accurately describe the nature of type B uncertainties. Examples of type B uncertainties are: “*previous measurement data, experience with or general knowledge of the behaviour and properties of relevant materials and instruments, manufacturer’s specifications, data provided in calibration and other certificates or uncertainties assigned to reference data taken from handbooks*” [28].

Type A uncertainties are the uncertainties that will arise when conducting experimental (empirical) measurements. Prior to any type A uncertainty analysis, all type B uncertainties must therefore be considered accordingly.

Type A uncertainties are the ones accompanying the data that will be analysed in Section 5.2. It is assumed that the experimental data as well as the object of interest, denoted as the measurand  $Y$ , comply with the *Central Limit Theorem (CLT)*.

The *CLT* states that “*sums or other functions of a large number of independent or weakly-dependent random variables have a probability distribution close to the normal distribution*” [56]. Thus, with a large enough number of samples taken from a population, the distribution of all the arithmetic means of the samples is approximately *Gaussian*. Furthermore, this means that the arithmetic mean of the sampling distribution will be approximately equal to the arithmetic mean of the population distribution. In the more narrow context, the theorem states that the sum of several independent and random estimates will approach a *Gaussian* distribution, regardless of what kind of a distribution the single variables have. Due to this fact, also the *combined standard uncertainty* can be described by a normal distribution [56].

Hence, it is given that a continuous random variable  $X_n$  can be described by the *Gaussian* probability density function:

$$g(X_n) = \frac{1}{\sigma\sqrt{2\pi}} \exp\left[-\frac{1}{2}\left(\frac{X_n - \mu_{X_n}}{\sigma}\right)^2\right] \quad (1)$$

for  $-\infty < X_n < +\infty$  and with  $\sigma$  being the standard deviation and  $\mu$  the expectation of the distribution.

This assumption allows to apply the *Gaussian* law of uncertainty propagation, which will be described subsequently [28].

The calculations of an uncertainty budget start by first establishing the equation that defines the measurand  $Y$ , which is the actual result of the measurement performed.  $Y$  is thus the variable of interest to be determined by the study conducted, together with its associated uncertainty. Usually,  $Y$  is not directly measured but is a function of  $n$  variables ( $X_1, X_2, \dots, X_n$ ):

$$Y = f(X_1, X_2, \dots, X_n) \quad (2)$$

As stated in the *GUM* [28], the input quantities  $X_1, X_2, \dots, X_n$  are most likely dependent on other quantities themselves, which is why the function  $f(X_1, X_2, \dots, X_n)$  is often very complex. Sometimes assumptions have to be made and it can get more difficult to find potential sources of uncertainty along the process of data analysis. Hence, the many sources of uncertainties have to be assessed, such as: the incomplete definition of the measurand, non-representative sampling of the population, equipment, operator, environment, resolutions, measurement method or variations in the results [11] [28].

Since it is only possible to approximate the measurement result (in the sense that it is calculated along with its uncertainties), but the true value is never known, we denote Equation 2 as the output estimate  $y$  of the measurand  $Y$ .

Hence, this is denoted as:

$$y = f(x_1, x_2, \dots, x_n) \quad (3)$$

with the input estimates  $x_1, x_2, \dots, x_n$ .

Each of the input estimates therefore has its own uncertainty. For type A uncertainties of a normally distributed data set, the following equation describes the calculation of the *combined standard uncertainty*  $u_c(y)$  of the estimated output  $y$ , which represents the best estimate of the measurand  $Y$ :

$$u_c^2(y) = \sum_{i=1}^n \left( \frac{\partial f}{\partial x_i} \right)^2 u^2(x_i) + 2 \sum_{i=1}^{n-1} \sum_{j=i+1}^n \frac{\partial f}{\partial x_i} \frac{\partial f}{\partial x_j} \cdot u(x_i, x_j) \quad (4)$$

where  $f$  is the function from Equation 2 (and thus Equation 3),  $u(x_i)$  and  $u(x_j)$  being the associated uncertainties of the input estimates ( $x_1, x_2, \dots, x_n$ ) of the quantities ( $X_1, X_2, \dots, X_n$ ), the partial derivatives being the estimated sensitivity coefficients of the input estimates and the second term referring to the estimated covariance associated with  $x_i$  and  $x_j$ . The *combined standard uncertainty*  $u_c(y)$  is the positive square root of the *combined variance*  $u_c^2(y)$ .

To solve Equation 4 describing the *combined variance* (and hence the *combined standard uncertainty*) of the estimated output  $y$ , the different components (estimated uncertainties, estimated sensitivity coefficients and the estimated covariance) of the equation must first be calculated. Thus, the first step is to receive the uncertainty of the individual estimated inputs.

### Uncertainty of an Individual Estimated Input

The uncertainty  $u(x_i)$  of an individual estimated variable is derived by calculating the estimated standard deviation ( $\sigma_i$ ) of the targeted variable. If the result used for further data analysis is the arithmetic mean of a repeated acquisition of experimental measurements, the standard deviation needs to be divided by the square root of the number of acquisitions. This is due to the assumption that when deriving the arithmetic mean of a sample, the actual intention is to derive an estimate of the arithmetic mean of the whole population via the sample (this is legitimate due to the *CLT*, see above). The calculated arithmetic mean is hence supposed to be representative for the whole population and the aim is to indicate the uncertainty of this estimate of the arithmetic mean of the population. This also means that the uncertainty of a sample will decrease as the number of measurement acquisitions increases [6].

Hence, to receive the uncertainty  $u(x_i)$  of an individual estimated variable, it is first necessary to calculate the arithmetic mean ( $\bar{x}$ ):

$$\bar{x} = \frac{1}{n} \sum_{i=1}^n x_i \quad (5)$$

where  $x_i$  are the individual acquisitions and  $n$  is the number of acquisitions.

Furthermore, the estimated standard deviation  $\sigma_{x_i}$  (or  $s_{x_i}$ ) needs to be computed:

$$\sigma_{x_i} = s_{x_i} = \sqrt{\frac{\sum_{i=1}^n (x_i - \bar{x})^2}{n - 1}} \quad (6)$$

In the case that no arithmetic mean is used for further calculations,  $u(x_i)$  equals the standard deviation ( $\sigma_{x_i}$ ). If repeated measurements were obtained and thus the arithmetic mean is used, the uncertainty is defined as follows:

$$u(x_i) = \frac{\sigma_{x_i}}{\sqrt{n_{x_i}}} \quad (7)$$

Equation 6 or 7 then serves as input for the uncertainty  $u(x_i)$  per estimated input and can be propagated in the further course of the data analysis.

### Sensitivity Coefficients

The estimated sensitivity coefficient ( $c_{x_i}$ ) of an individual estimated input variable ( $x_i$ ) is derived by calculating the partial derivative of the function with respect to the estimated input variable [28]:

$$c_{x_i} = \frac{\partial f}{\partial x_i} \quad (8)$$

The estimated sensitivity coefficients describe how the output estimate  $y$  varies with changes in the values of the input estimates ( $x_1, x_2, \dots, x_n$ ) [28]. They thus describe the sensitivity of the output estimate  $y$  with respect to a change in an individual estimated input variable [68]. Estimated sensitivity coefficients can be derived in three different ways: mathematically, numerically or experimentally. In practice, it is often a combination of all three methods that are used on the way to the resulting uncertainty budget [68].

### Covariance

The second term of the equation of the *combined standard uncertainty* (Equation 4) represents the estimated covariance of the variables [28]:

$$2 \sum_{i=1}^{n-1} \sum_{j=i+1}^n \frac{\partial f}{\partial x_i} \frac{\partial f}{\partial x_j} \cdot u(x_i, x_j) \quad (9)$$

where the estimated sensitivity coefficients are multiplied by the estimated covariances of the input variables, as

$$cov(x_i, x_j) = u(x_i, x_j) \quad (10)$$

where  $u(x_i, x_j) = u(x_j, x_i)$ , which can also be denoted as

$$u(x_i, x_j) = u(x_j, x_i) = r(x_i, x_j)u(x_i)u(x_j) \quad (11)$$

where  $r(x_i, x_j) = r(x_j, x_i)$  is the estimated correlation coefficient, which characterises the degree of correlation between  $x_i$  and  $x_j$  and hence lies between  $-1 \leq r(x_i, x_j) \leq +1$  [28].

The estimated covariance states whether the input estimates are independent or correlated. If the input estimates are uncorrelated, the estimated covariance and estimated correlation coefficient are equal to zero.[28]

Deriving the estimated covariance of several input estimates can be a very complex matter. Several approaches exist that can be used to obtain estimated covariances:

A) The measurement equation will be rearranged in order that the several quantities are no longer correlated, B) the estimated covariances are computed using an error model, C) the correlation of the estimated input variables are derived experimentally or numerically or D) an estimation on the range of possible values for the correlation is performed [68].

For large projects such as the upcoming *Traceable Radiometry Underpinning Terrestrial- and Helio- Studies (TRUTHS)* satellite calibration mission, discussions about the uncertainty budget led to the realisation that estimated covariance matrices are too extensive in terms of complexity as well as computational effort and time resources. Hence, for this project, a simplified and faster approach will be implemented that will most likely overestimate the uncertainty budget (Kick-Off meeting *TRUTHS*) [48].

With all the terms defined, the *combined standard uncertainty* for the estimated output  $y$  can be calculated according to Equation 4. The *GUM* [28] states that the value  $u_c(y)$  can now be used as “*the parameter for expressing quantitatively the uncertainty of the result of a measurement*”.

## Expanded Uncertainty

Often, it is desired to expand the obtained *combined standard uncertainty*  $u_c(y)$ , to cover a wider range of the possible distribution of uncertainty values of the best estimate of the measurand. The calculated value is then called the *expanded uncertainty* ( $U$ ). How much of the distribution should be covered by the *expanded uncertainty*, or how high the level of confidence (also known as coverage probability) is, depends on the type of measurement, as well as the industry in which the data are used. However, it is usually between 95 % and 99 % [28].

To determine the *expanded uncertainty* ( $U$ ), a multiplication of the so-called coverage factor  $k$  with the *combined standard uncertainty*  $u_c(y)$  is performed:

$$U = ku_c(y) \tag{12}$$

This leads to a measurement result denoted as  $y = y \pm U$ , where  $U$  is an interval around the best estimated output  $y$  representing the best estimated uncertainty values for  $Y$  defined by the previously chosen level of confidence [28].

As mentioned, the coverage probability is often desired to be between 95 % and 99 % leading to a coverage factor between two and three. In the metrology industry, when the procedure of performing the measurements is well established and a sufficient number of measurements is obtained, a coverage factor of two leads to a level of confidence of about 95 % [28]. This is again due to the *CLT*: the more measurements obtained, the more the data tend to be *Gaussian* distributed. Hence,  $k = 2$  will account for 95 % confidence for a normal distribution and is conventionally used in the industry [63] [65]. However, to be very precise, it has to be acknowledged that the definition that  $k = 2$  equals a level of confidence of 95 % is not utterly correct, despite being well established as a value for the coverage factor  $k$ .  $k = 2$  rather accounts for 95.45 % of confidence. It would hence be  $k = 1.96$  that refers to 95 %.



There are also rare circumstances where a coverage factor  $k$  is other than two. This is the case, for example, when “(1) a value other than  $k = 2$  is required for a specific application dictated by an established and documented requirement; and (2) that value of  $k$  must provide an interval having a level of confidence close to a specified value” [63].

In such a case  $k$  can be calculated by computing the effective coverage factor  $k_p$ . This requires the effective degrees of freedom ( $v_{eff}$ ), the probability ( $p = 1 - \alpha$ , with  $\alpha$  being the significance level) and the *Student’s T distribution*. In this case, Equation 12 will be written as:

$$U_p = k_p u_c(y) \quad (13)$$

To obtain the effective coverage factor  $k_p$  that fits the equation of the obtained measurement, first the effective degrees of freedom have to be computed using the *Welch-Satterthwaite* equation:

$$v_{eff} = \frac{u_c^4(y)}{\sum_{i=1}^n \frac{u_i^4(y)}{v_i}} \quad (14)$$

where  $v_i$  is the degrees of freedom of the data set ( $v_i = n - 1$ ) and  $n$  is the number of samples used for the calculation of the standard deviation of one variable.

With  $v_{eff}$  obtained, the *Student’s T-distribution* table can be consulted to obtain the desired value of  $k_p$  [65]. If  $k_p$  is not an integer, a linear interpolation between the values of the *Student’s T-distribution* table is necessary (or the next lower value for  $k_p$  stated in the table can be used) [65]. Finally, the *expanded uncertainty*  $U_p$  can be computed.

## 1.4 Uncertainty in Field Spectroscopy: State of the Art and Motivation

The calculation of an estimate of the uncertainty of field spectroscopy measurements is a crucial part of the overall data analysis of a target product. In order to generate a valuable product that provides further insights into thematic content (such as climate change or similar topics), high data quality must be ensured.

Spectroradiometric in-situ measurements in particular must be of high data quality in order to provide reliable validation data. Therefore, the identification and, at best, elimination of error sources as well as a holistic calculation of the uncertainty of field spectroscopy measurements is necessary.

Usually manufacturers of field spectroradiometers provide a manual for the correct operation of their instrument. These manuals provide a solid basis on the acquisition of field spectroscopy measurements and in some cases also state potential sources of uncertainties. Unfortunately, however, they do not provide complete uncertainty budgets. The field spectroscopy guide of the *Spectra Vista Corporation (SVC)* [4], e.g., explicitly mentions that they assume potential errors to be estimated arising from the operator's handling of the instrument, which must be taken into account in order to obtain a valid and complete uncertainty budget [4]. Cautionary notes are given and for one source of uncertainty (the effect of the usage of a tilted panel) actual data analysis is added.

The same applies to the manuals of the *Analytical Spectral Devices (ASD) FieldSpec* instrument range [2] [3]. Influencing factors are mentioned and attention is drawn to the topic of the potential introduction of uncertainties. However, applicable values in the form of an uncertainty budget or correction factors are not provided.

Some scientific studies have been conducted on the subject of uncertainty in field spectroscopy measurements.

Goetz [19] conducted measurement and data analyses on various measurement influencing aspects. He investigated, e.g., scatter effects from surroundings, the clothing of the operator, operator proximity to the measurement setup or effects due to the change in solar irradiance over time [19]. All effects are also investigated as a function of wavelengths. Unfortunately, no actual correction factors or uncertainties are stated for the entire spectral range of the instruments. However, first rough statements about the impact of external factors are made. For example, the effect of blue clothing in the close proximity of the panel (within inches) has an effect “*as much as 12% of the measured reflectance*” [19].

Soffer [60] presented results on the perturbing factor of the operator proximity to the sensor and reference panel, once in the antisolar position and once perpendicular to the solar principal plane. Measurement errors as large as  $-5\%$  (at 350 nm) and  $7\%$  (in *near-infrared (NIR)/short-wavelength infrared (SWIR)* range) were identified at the most perturbing positions, showing the impact of such (unintentional) operator behaviour [60]. Soffer also stated the unfortunate fact that he only found one publication on this topic [60] (see [30]).

Various aspects of uncertainties associating field spectroscopy measurements are described by Walsh et al. (preprint submitted March 2020) [66]. They conducted experiments on the temporal instability of the instrument, the use of a support to stabilise the spectroradiometer, the manual movement of the white reference panel between measurements and the uncertainties introduced due to operators following a standard procedure for acquiring field spectroscopy measurements. Overall, they concluded that approximately  $5\%$  of the uncertainty in the measurements is due to the instrument and the methodological procedure applied, and that further research on these topics is necessary [66].

Mac Arthur and Robinson [43] stated that nowadays the topic of uncertainties in field spectroscopy is more widely recognised and developments on minimising uncertainties and improving in-situ sampling methods are encouraged. Nevertheless, various key challenges remain to be addressed [43].

The community's crucial comprehensive understanding of sources of uncertainty and the importance of quantifying them has not yet been achieved. The identification of all the different measurement-influencing factors, the calculation of correction models and measurement associated uncertainties would be a general aim that should be targeted. This would ensure a higher data quality of derived products in the further course of a data analysis chain.

This thesis provides a first attempt to approach the holistic calculation of an uncertainty budget for in-situ spectroradiometric measurements. Several experiments were conducted in order to isolate measurement influencing factors and calculate associated uncertainties. One exemplary experiment of the effect of different distances of the fibre optic tip (sensor aperture) to the surface of the white reference panel was analysed subsequently and a correction model as well as associated uncertainties were computed. This provides a first contribution to a complete uncertainty budget for field spectroscopy measurements and the results emphasise once more the importance of the topic. To our knowledge, such an experiment has not yet been carried out.

## 1.5 Terminology

For the sake of simplicity and due to ambiguity in the community, several terms are defined to prevent confusion:

- **Irradiance** ( $E$ ): Radiant incidence. “Power per unit area that is incident on a surface.”. For example the solar radiation [ $W/m^2$ ] [51].
- **Radiance** ( $L$ ): “Radiance is the elemental quantity of radiometry, power per unit area, and per unit projected solid angle” [ $W/m^2sr$ ] [51].
- **Spectral irradiance** ( $E_\lambda$ ): Irradiance ( $E$ ) per wavelength [ $W/m^2nm$ ] [51].
- **Spectral radiance** ( $L_\lambda$ ): Radiance ( $L$ ) per wavelength. “Watts per unit area per unit-projected solid angle per unit-wavelength interval; fundamental unit of radiometry” [ $W/m^2srnm$ ] [51].

In addition, it is important to define the viewing geometry of the instruments and hence the characteristics of the measured spectral radiance. As defined by Schaepman-Strub et al. [57] based on Nicodemus et al. [49], there are nine identified cases of incoming and reflected spectral radiance relations. Only four of these nine cases are actually measurable, and it is important to define exactly which case has been applied in field measurements in order to obtain consistent and comparable results across the community.

For all the subsequent experiments conducted outdoors, the term “spectral radiance” refers to a conical observation of a hemispherically incoming spectral radiance. If one would compute the reflectance factor of such a measurement, it would be defined as the *Hemispherical-Conical Reflectance Factor (HCRF)* [57]. This case applies when measurements are performed under ambient sky illumination where the solid angle must be integrated for the entire hemisphere (hence:  $\omega_i = 2\pi$ , with  $\omega_i$  being the solid angle of the incident beam of radiation) [57].

## 2 Experiments

### 2.1 Introduction to the Experiments

Field spectroscopy measurements can be obtained with a variety of different tools and methods, as well as different levels of operator experience. However, the measurement of spectral radiance is very sensitive and easily distorted. Differing acquisition conditions lead to various (unwanted and potentially unnoticed) influences that affect the measured data set.

Therefore, it is very important to know what will influence the measurement of the target object and which uncertainties these influences introduce.

In order to investigate different influences due to the setup, the environment or the operator's acquisition technique, several experiments were designed and conducted.

Unfortunately, it is beyond the scope of this Master's thesis to analyse all the data sets obtained. Hence, one experiment was chosen to demonstrate an exemplary analysis and show the importance of future work on this aspect. In this section, all the other conducted experiments are briefly introduced and a more detailed description of the experimental procedures can be found in Appendix C.

## 2.2 Performed Experiments

A total of nine experiments were carried out to obtain information on factors that may influence field spectroscopy measurements.

1. An investigation was made to see if there is a difference in measured spectral radiances with different distances of the fibre optic tip (sensor aperture) to the reference panel.
2. Measurements were carried out for a comparison of the measured spectral radiances on an inclined reference panel versus a levelled panel.
3. An experiment was conducted on the operator's influence in terms of the distance to the white reference panel.
4. The potential influence on the spectral measurements due to the position of the operator in relation to the sun was investigated.
5. Data were collected to compare the use of a rest for the data acquisition versus holding the pistol grip containing fibre optic cable by hand.
6. An experiment on the ideal number of target measurements to be obtained was carried out.
7. A data collection was carried out on the potential influence on the measurements by applying different acquisition patterns.
8. Data were gathered on potential differences in acquired spectral radiances due to the instrument not being properly warmed up.
9. Investigations were made on an ideal time frame of an acquisition.

Experiments that were not conducted but should be considered in future work are:

- The potential influence of scratches in the white reference panel in the projected *Field Of View (FOV)* of the instrument.
- The comparison of the influence of a dirty white reference panel versus a clean one on the acquired data values.
- A potential visible effect of whether or not the reference panel setup has been moved between white reference acquisitions.
- An experiment on the ideal number of reference measurements to be obtained.

Experiment one was chosen for the subsequent data analysis displayed in Section 3.

## 2.3 Used Devices and Setup

For the experiments, field spectroradiometers and white reference panels were used, which are presented below.

### 2.3.1 Field Spectroradiometers

Field spectroradiometers manufactured by the company *Malvern Panalytical Ltd* (a *Spectris* company) were used. Instruments of different product ranges were utilised: an *ASD FieldSpec 3*, an *ASD FieldSpec 4* and an *ASD FieldSpec 4 Hi-Res*.

The most important specifications of the devices related to this study are listed in Table 1:

Table 1: Selected specifications of the field spectroradiometers used [2] [3].

|                            | ASD FieldSpec 3   | ASD FieldSpec 4   | ASD FieldSpec 4 Hi-Res  |
|----------------------------|---|---|---|
| <b>Spectral range</b>      | 350 - 2500 nm   | 350 - 2500 nm   | 350 - 2500 nm   |
| <b>Spectral resolution</b> | 3 nm at 700 nm,<br>10 nm at 1400/2100 nm  | 3 nm at 700 nm,<br>10 nm at 1400/2100 nm  | 3 nm at 700 nm,<br>8 nm at 1400/2100 nm   |
| <b>Spectral sampling</b>   | 1.4 nm for 350 - 1000 nm,<br>2 nm for 1000 - 2500 nm  | 1.4 nm for 350 - 1000 nm,<br>1.1 nm for 1000 - 2500 nm  | 1.4 nm for 350 - 1000 nm,<br>1.1 nm for 1000 - 2500 nm  |
| <b>Scanning time</b>       | 100 ms  | 100 ms  | 100 ms  |
| <b>Number of Channels</b>  | 2151  | 2151  | 2151  |
| <b>Detectors</b>           | VNIR: 512 element silicon array,<br>SWIR1 & SWIR 2:<br>Graded Index InGaAs Photodiode,<br>Two Stage TE Cooled | VNIR: 512 element silicon array,<br>SWIR1 & SWIR 2:<br>Graded Index InGaAs Photodiode,<br>Two Stage TE Cooled | VNIR: 512 element silicon array,<br>SWIR1 & SWIR 2:<br>Graded Index InGaAs Photodiode,<br>Two Stage TE Cooled |
| <b>Input</b>               | 1.5 m fibre optic (25° FOV)   | 1.5 m fibre optic (25° FOV)   | 1.5 m fibre optic (25° FOV)   |
| <b>Weight</b>              | 5.6 kg  | 5.44 kg   | 5.44 kg   |
| <b>Calibrations</b>        | NIST traceable  | NIST traceable  | NIST traceable  |

Each of the field spectroradiometers operates over the spectral range from 350 - 2500 nm with three implemented photodetectors that measure the incident radiant energy. The incoming photons are converted into electrons and saved as *Digital Numbers (DN)*. Subsequently, the *DNs* are converted into spectral radiances by applying a calibration. For the *visible and near-infrared (VNIR)* spectral range (350 - 1000 nm), the detector is a *Charge-Coupled Device (CCD)*, which is a 512 element silicon photo-diode array. For the SWIR range, namely SWIR1 (1000 - 1830 nm) and SWIR2 (1830 - 2500 nm), a thermoelectrically cooled *Indium Gallium Arsenide (InGaAs)* photo-diode is incorporated for both [2]. Fibre optics are used to transmit the at-sensor spectral radiance directly to the detectors [22].

### Instrument Warm-up

Unfortunately, the three detectors do not warm up at the same rate when the device is switched on [41]. Yet it is crucial for the acquisition of spectroradiometric measurements that the detectors reach equilibrium and are thus stable, as the spectral sensitivity of the spectroradiometers changes with temperature. The different warm-up rates lead to drifts in the spectrum (spectral discontinuities) where the joints of the detectors are especially prone, resulting in a distorted spectrum [2]. Hemmer and Westphal [23] obtained laboratory measurements with a predecessor of the *ASD FieldSpec 3*, the *FieldSpec FR*, regarding the changing spectral sensitivity with temperature. They concluded that the low spectral end of the SWIR2 detector drifts up to 20% and the high end of the VNIR detector up to 7.5% (see Fig. 1). Also with newer instruments, the drifts are still present [26].

Additionally, the ambient temperature has been identified to also have an increasing effect on the detector joint jumps (which can thus not be eliminated by sufficient warming up) [26]. Hence, in order to correct the drifts, a jump correction has to be applied to the distorted overlap regions. The manufacturer implemented a parabolic correction function that corrects for the thermal response of the instruments [10]. Hueni and Bialek [26] further improved the parabolic correction for calibration and validation purposes.

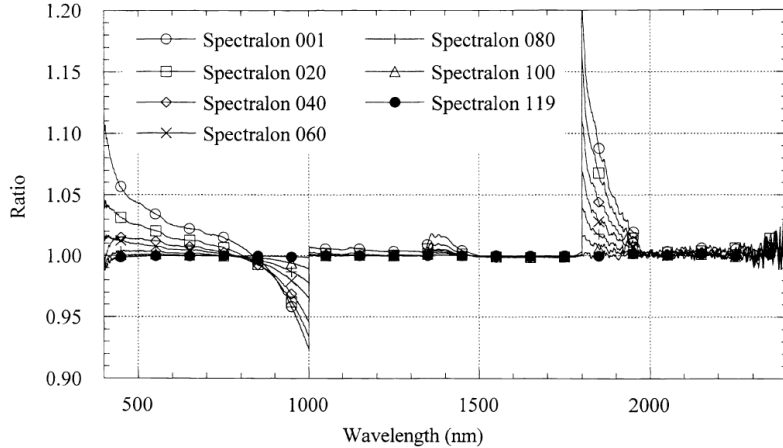


Figure 1: Ratio of the spectral radiances at different times during the warm-up period to the spectral radiance at the start of the experiment conducted by Hemmer and Westphal [23]. (Figure from Hemmer and Westphal [23].)

It is still strongly recommended by the manufacturer to properly warm up the field spectroradiometer for at least 30 min to preferably one hour before any data acquisition, even if the jumps can be corrected [2]. In compliance with this, it allows the three detectors to stabilise (to some degree) [2] [41].

## Dark Current

Every photosensitive device is accompanied by a so-called *Dark Current (DC)*, an electric current inherent to the detectors. It is generated “*due to the thermal excitation of electrons into the conduction band and collection in the CCD wells*” [67]. The *DC* is therefore a by-product that always occurs, regardless of whether the detectors are exposed to light or not. These *DC* values are added to the acquired spectral radiance measurements and therefore distort the latter. They are strongly temperature-dependent for the entire electromagnetic range covered by the field spectroradiometers, and are also dependent on the integration time in the VNIR range. This implies that with a varying ambient temperature, also the *DC* varies. In such cases, it is important to obtain the *DC* more frequently. However, in any case the measurements have to be corrected for this intrinsic instrument noise by a subtraction of the *DC* to obtain a reliable data set [3] [67].

## Fibre Optics

A number of optical fibres are connected to each of the three detectors, which in combination as a bundle define the sensor aperture at the tip of the fibre optic cable. However, the fibre optics belonging to the different detectors are not spatially uniformly positioned in the bundle, but are randomly arranged during the manufacture of the device [42]. Due



to this fact, each of the field spectroradiometers produced by *Malvern Panalytical* has a unique so-called *Directional Response Function (DRF)*. The *DRF* characterises the system’s spatial and spectral responsivity within the projected *FOV* as well as its sampling resolution [42]. This results in each instrument measuring slightly different values for the same projected *FOV*. In the case that one of the optical fibres of the entire fibre bundle is broken, it hence will affect the measured spectral radiance of the detector range to which the broken fibre has been assigned.

For some of the field spectroradiometers used, this unfortunately was the case as stated in Table 2. This source of error has to be kept in mind when performing the data analysis.

Table 2: Overview of the field spectroradiometers used and their number of functioning fibres.

| Instrument             | Instrument number | VNIR fibres | SWIR1 fibres | SWIR2 fibres |
|------------------------|-------------------|-------------|--------------|--------------|
| ASD FieldSpec 3        | 16007             | 19/19       | 17/19        | 19/19        |
| ASD FieldSpec 4        | 18130             | 18/19       | 19/19        | 19/19        |
| ASD FieldSpec 4 Hi-Res | 18739             | 19/19       | 19/19        | 19/19        |

### 2.3.2 White Reference Panel

The white reference panel is a crucial and indispensable item when it comes to in-situ spectroradiometric measurements. Its purpose is to provide as accurate a representation as possible of the incident solar radiation (*Panel Substitution Methodology*) [60]. A target measurement can be standardised by the division of the measured target spectral radiance by the measured spectral radiance of the reference panel [55]. The result of this division will hence provide the reflectance characteristics of the target matter.

In order to receive the above-mentioned reflectance values (*HCRFs*) of an object of interest, the reference panel must have characteristic properties.

A reference panel should ideally provide a perfectly diffuse surface. Hence, it should be reflecting lossless and act *Lambertian* (“*distributing energy from any incident illumination into all viewing directions equally*” [33]) [47].

An often used material is *Labsphere’s Spectralon* which is also recommended to be used with *ASD FieldSpec* instruments [2]. *Spectralon* reflectance material is made of polytetrafluoroethylene and sintered halon. Its reflectance is >99% for the spectral range from 400 - 1500 nm and >95% for 250 - 2500 nm as stated by the manufacturer [35]. Thus, unfortunately, no reference panel is 100% diffuse and perfectly uniformly reflecting across the spectral range considered, which has to be taken into account for field spectroscopy measurements [17] [35] [47]. A varying viewing geometry of the instrument thus also has an influence on the measured spectral radiance.

A clean and preferably calibrated reference panel is of great importance for the acquisition of field spectroscopy measurements in terms of quantifying the uncertainty of the obtained data. If the white reference panel is compromised in one way or another (dirt, scratches), this will introduce uncertainty into the measurements (especially if radiance measurements are to be analysed).

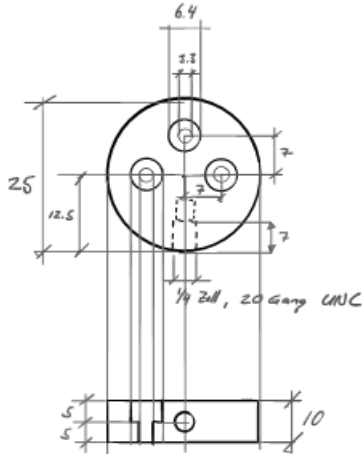
Also, each calibrated reference panel is accompanied by a calibration certificate that specifies a correction factor. This correction factor has to be applied to measurements involving the panel in order to make them traceable to standards of the *National Institute of Standards and Technology (NIST)* [35].

## 2.4 Default Setup

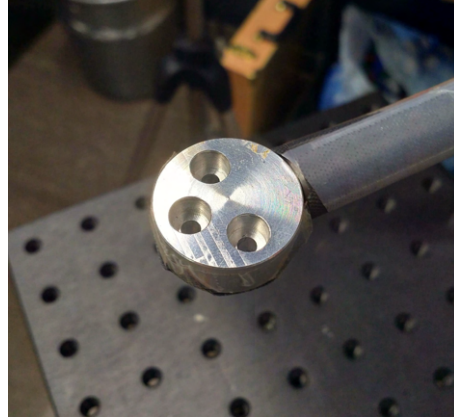
The default setup (see Fig. 3 and Table 3) is defined as the installation used for all the reference measurements conducted while an experiment was in progress (unless otherwise specified). It consisted of a tripod that had a black fixing plate with the dimensions 20.4 x 20.4 cm (= 8 x 8 in) screwed onto it. The fixing plate was levelled with the horizon, i.e. it was perpendicular to the force of gravity and provided a surface to position the reference panel. The height from the ground to the surface of the white reference panel was 100 cm  $\pm$  0.1 cm (uncertainty defined by the resolution of the ruler used).

On the fixing plate, the white reference panel was aligned using two screws on one edge of the plate. This ensured that the same position was maintained for all measurements. On the opposite edge, the furthest from the panel, a shiny, straight metal rod was screwed into the fixing plate. Attached to the rod was a connection piece capable of holding another pole perpendicular (hence horizontal) to the first vertical rod. A fibre holder (see Fig. 2) was attached to the end of the horizontal rod and hovered above the centre of the reference panel.

A fibre holder is a piece of aluminium that has indentations that can hold up to three fibre optic tips at the same time. These indentations were designed to project a similar *FOV* facing nadir (a viewing angle of 0° from the normal of the panel) onto the white reference panel. According to [16], the nadir view is defined as a measurement standard geometry by the *International Commission on Illumination*.



(a) Sketch of the fibre holder design.



(b) The fibre holder screwed to the horizontal rod.

Figure 2: The design of the fibre holder used for the conducted experiments.

The rods as well as the fibre holder were coated with a black tarpaulin material to prevent unwanted reflected radiation from the metal, which could have distorted the measurements. The fibre optic tip of the reference instrument was inserted into the front recess of the fibre holder. The distance from the fibre optic tip to the surface of the panel was set to 12 cm  $\pm$  0.1 cm as default. This setting projects a nominal *FOV* onto the panel with a radius of 2.66 cm. The fibre optic tip was aligned using a bubble level pointing towards nadir and the centre of the panel. Since the fibre tip was fixed in the fibre holder, the fibre optic cable did not move while the measurements were acquired. Hence, a “wobble effect” of a moving cable (and therefore moving fibres) did not have to be taken into account [34].



Figure 3: The reference setup installed to collect spectral data.

The used field spectroradiometer was always (unless otherwise specified) properly warmed up for at least one hour before the first measurement. The power supply for the instruments as well as for the laptops was provided by a power socket. This avoided running out of power, as the batteries normally used in the field would not have lasted for a full day of measurements. The cleanest available reference panel with the fewest scratches was selected to serve as the panel for all reference measurements, assuming that it would therefore provide the most accurate values.

The panel was a square *Spectralon* panel with a side length of 12.7 cm manufactured by *Labsphere* [35]. Unfortunately, the chosen panel, although the smoothest one available, was also contaminated with scratches. Luckily, none of them were in the projected *FOV* of the sensor when it was mounted at a height of 12 cm above the panel. The white reference panel was cleaned two days prior to the first measurement applying the standard cleaning procedure recommended by the manufacturer. That is, the panel was sanded with a fine-grained sandpaper under running water on a flat surface [38].

In order to ensure a levelled panel, a bubble level glued to the side of the reference panel was used as a first step. Furthermore, this method was controlled with two different free *Android* applications named “*Climometer*” [54] and “*Bubble Level*” [18]. Both applications were calibrated following the developer’s instructions. According to the latter, all levelling efforts were within  $1^\circ$  of deviation.

The appliance with the fibre holder was aligned perpendicular to the solar principal plane at all times. With a changing solar azimuth angle (and also solar elevation angle), the appliance had to be rotated to always maintain the position perpendicular to the solar principal plane. This was done to avoid any potential influence of the appliance reflecting additional radiation coming from the pole or casting shadows when oriented otherwise.

If the experimental measurements took longer than approximately 15 min, the spectroradiometer was optimised again to adjust for changes in the solar irradiance before any unwanted saturation occurred. This procedure is also recommended by the manufacturer [2].

The general settings for the spectroradiometric measurements were as follows: The average of the *DC* spectra was set to 100 and the internal average for radiance spectra to 25, according to the usual field spectroscopy procedure of the *Remote Sensing Laboratories (RSL)* of the *University of Zurich*. The time interval between the measurements was set to zero seconds and the integration time was defined by optimising the instrument to best match the current solar irradiance conditions.

The person operating the spectroradiometer always started the measuring procedure from a distance of at least two to three metres away from the setup.

Table 3: Summary of all specifications of the default setup.

| <b>Specification of the default setup</b>            | <b>Value</b> |
|--|--------------|
| Height of panel above ground                         | 100 cm       |
| Distance of the fibre optic tip to the panel surface | 12 cm        |
| Warm-up time   | min. 1 h     |
| Dark Current   | 100 spectra  |
| Internal spectra average                             | 25 spectra   |
| Time between measurements                            | 0 s          |

### 3 Introduction to the Exemplary Experiment: Distance From the Fibre Optic Tip to the White Reference Panel

Any acquisition of field spectroscopy data usually consists of both target measurements and reference measurements [42]. To obtain reference measurements using a white reference panel, the sensor tip must be positioned above the reference panel at a certain distance to the latter's surface. This distance between the tip of the fibre optic cable and the surface of the white reference panel is hardly ever mentioned in studies that use field spectroscopy measurements as a data collection method (e.g., [5], [14], [21], [31], [53] or [60]). The impression is thus not given that the distance was deliberately chosen.

Available guides from manufacturers and other sources on how to conduct measurements with a field spectroradiometer also do not mention a recommended absolute operating height above the panel (e.g., [1], [2], [3], [19] or [41]). The *Spectra Vista Corporation* provides the exception and gives a recommendation of 30 cm distance to a 25 x 25 cm panel in their *Field Spectroscopy Guide for the SVC i-series Spectroradiometers* [4]. Their reasoning is that at this distance, the *SVC* spectroradiometer only shades about 3% of the skylight (around <0.2% of the total illumination at 700 nm) [4]. However, this can only be applied to this particular series of instruments. Since instrument compositions vary greatly among different manufacturers, such recommendations would be necessary for all devices on the market. In the case of the *ASD FieldSpec* series, for example, the fibre optics are implemented as a cable with a small tip at the end, whereas the above mentioned *SVC* device measures with a lens built directly into the instrument (no fibre optic cable extension). In the *ASD FieldSpec 3* user manual [2], it is mentioned that a pistol grip used will block some of the diffuse radiation, which is why objects in general and preferably also the user should be positioned as far away as possible. However, no absolute distance to the reference panel is recommended. On the one hand, the reason for this overall lack of recommendations could be that the distance of the fibre optic tip to the panel has no influence on the measurements and it is thus not of importance to pay attention to the height at which the fibre optic tip is held above the panel. On the other hand, few to no findings of this setup parameter in the literature raise the suspicion that it has not been extensively tested for the possible introduction of uncertainties due to different applications of this parameter. Varying heights of the pistol grip setup with the fibre optic tip fed-in deliver different projected *FOVs*. The higher the pistol grip is held or mounted to the appliance, the larger is the projected area on the panel and vice versa. Different geometries hence influence the path length of the spectral radiance. The information from *SVC* [4] indicates that the proportion of the sky hemisphere covered by the fibre optic tip is smaller the further away the tip is from the panel. This leads to the hypothesis that the further the fibre optic tip is from the white reference panel, the more spectral radiance reaches the sensor. Of course, the tip can only be so far away from the panel as the projected *FOV* still covers the area of the panel and does not go beyond its edges. Otherwise, the sensor registers not only the signal of the reference panel, but also the signal of matter around the panel, which would lead to distortions. Vice versa, a very proximate installation of the fibre optic tip fed into the pistol grip to the panel covers a large fraction of the sky hemisphere, resulting in a lower spectral radiance at the sensor aperture. Deductively, one would assume that the ideal distance for measurements of the white reference panel is infinitely far away, so that the sensor does not cover any fraction of the sky hemisphere and hence has no influence on the measurement at all. Of course, in reality this is not an applicable solution, hence it is hypothesised that it is best to measure at a distance between the two extremes of very close to the panel and very far away.

## 4 Research Questions and Hypotheses

The following research questions and hypotheses were studied:

### Research Questions:

- Is there a difference in measured spectral radiances at different distances of the fibre optic tip (sensor aperture) to the surface of the white reference panel, given that the projected *FOV* of the sensor is still on the panel?
- If there are differences, how large are they compared to the predefined default height of 12 cm (relatively)?
- If there are differences, would the application of a correction model, which corrects measurements acquired at different heights to the default height, add value, or would the associated uncertainty of the correction model still be greater?

### Hypotheses:

- $H_0$ : Several measurements performed using the same setup, but with the fibre optic tip at different heights above the panel, will lead to the same spectral radiance intensities, given that the projected *FOV* of the sensor is still on the panel.  
 $H_1$ : Several measurements performed using the same setup, but with the fibre optic tip at different heights above the panel, will lead to different spectral radiance intensities, given that the projected *FOV* of the sensor is still on the panel.
- $H_0$ : At greater distances from the fibre optic tip to the panel, the measured spectral radiance shows the same values compared to a default height of 12 cm as at smaller distances to the panel, given that the projected *FOV* of the sensor is still on the panel.  
 $H_1$ : At greater distances from the fibre optic tip to the panel, the measured spectral radiance shows higher values compared to a default height of 12 cm as at smaller distances to the panel, given that the projected *FOV* of the sensor is still on the panel.
- $H_0$ : At smaller distances from the fibre optic tip to the panel, the measured spectral radiance shows the same values compared to a default height of 12 cm as at greater distances to the panel, given that the projected *FOV* of the sensor is still on the panel.  
 $H_1$ : At smaller distances from the fibre optic tip to the panel, the measured spectral radiance shows smaller values compared to a default height of 12 cm as at greater distances to the panel, given that the projected *FOV* of the sensor is still on the panel.
- $H_0$ : The uncertainty of a correction model that corrects different distances to the panel to a default distance of 12 cm is smaller than the noise of the instrument.  
 $H_1$ : The uncertainty of a correction model that corrects different distances to the panel to a default distance of 12 cm is greater than the noise of the instrument.

To test these hypotheses, an experimental setup was designed and measurements were conducted for different selected heights above the reference panel (see Table 4).

In addition to the heights given in Table 4, two measurements were made at the heights of 2 and 5 cm above the panel, with the pistol grip tilted. Hence, a different *FOV* is projected onto the panel surface when using an inclined pistol grip compared to a fibre optic tip pointing nadir. These measurements were collected to investigate potential differences in measured spectral radiances between an inclined and a nadir pointing fibre optic tip.

The bare fibre bundle of an instrument of the *ASD FieldSpec* range has a *FOV* of about 25° [2]. The radius of the projected *FOV* of the fibre optic bundle is calculated as follows [52]:

$$r = \tan\left(\frac{FOV}{2}\right) \cdot h \quad (15)$$

With *FOV* being the *Field Of View* angle of the instrument, *h* being the distance from the fibre optic tip to the panel and *r* being the radius of the projected *FOV*.

Table 4: The specifications of the experimental setup.

| Distance to the panel (h) [cm] | Projected <i>FOV</i> radius (r) [cm] | Projected <i>FOV</i> diameter [cm] |
|--------------------------------|--------------------------------------|------------------------------------|
| 30                             | 6.65                                 | 13.3                               |
| 28.643 (28)                    | 6.35 (6.2)                           | 12.7 (panel side length) (12.41)   |
| 25                             | 5.54                                 | 11.08                              |
| 20                             | 4.43                                 | 8.87                               |
| 15                             | 3.33                                 | 6.65                               |
| 12 (default height)            | 2.66                                 | 5.32                               |
| 10                             | 2.22                                 | 4.43                               |
| 5                              | 1.11                                 | 2.22                               |
| 2                              | 0.44                                 | 0.88                               |

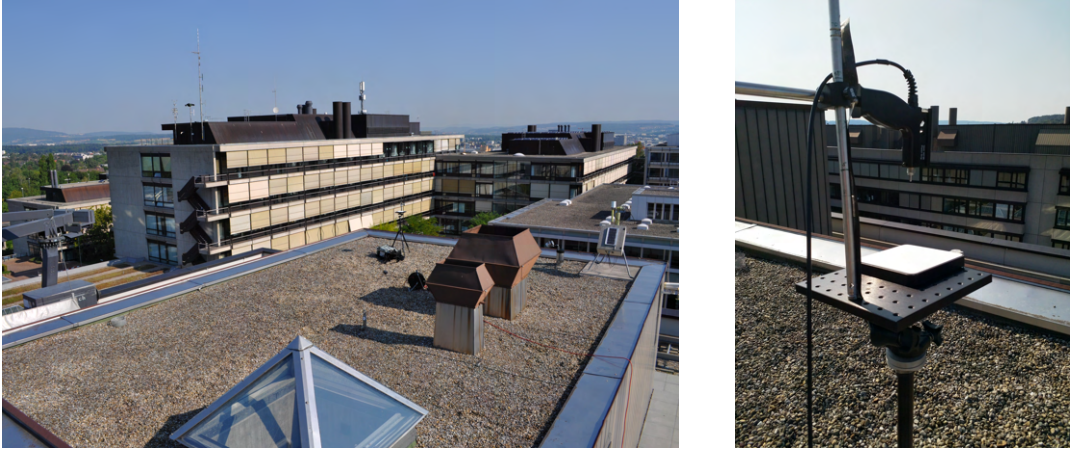
The experiment conducted aims to answer the prior posed hypotheses and research questions. As a product, a correction model was generated, which once applied, enabled the comparison of different field spectroscopy measurements with respect to the height of the fibre optic tip to the panel. Accompanying this, the associated uncertainties of the model were quantified.

## 5 Method

This part of the thesis consists of three sections. The first section presents the experimental setup and the data collection procedure. This is followed by the data analysis resulting in the correction model and the last section provides the uncertainty analysis accompanying the data analysis. The latter two are separated for ease of reading.

### 5.1 Experimental Setup and Procedure

The roof of the building Y25 of the University of Zurich's Irchel Campus (see Fig. 4) was used as the location for the experiment (N 47.396759, E 8.549472). Measurements were collected on the 9<sup>th</sup> of September 2020 on a clear day with a maximum temperature of 25.2°C (Zurich Fluntern weather station, N 47.37794, E 8.56575 [45]). The maximum solar elevation angle (solar culmination) for this day and location was 47.66° and occurred at 13:22:58 *Central European Summer Time (CEST) (Universal Time Coordinated +2)* with a sun azimuth angle of 179.64°. The daylight duration for this day was 12 h 45 min 29 s [24].



(a) The roof of building Y25 of the University of Zurich's Irchel Campus, which served as the experimental location. The reference setup was already installed.

(b) The experimental setup.

Figure 4: The location and setup.

The weather conditions on the measurement day were favourable with blue skies and no clouds. The visibility decreased slightly on the horizon.

For the experimental setup (see Fig. 4), the default setup (single-beam configuration) was installed with minor adjustments. Instead of a fibre holder, a pistol grip with an integrated bubble level at the top of it was screwed to the end of the horizontal rod in order to have the same circumstances as for an in-situ measurement. A scale with the different heights from Table 4 was written on the vertical rod that was screwed to the far edge of the installation. The heights were marked with a potential deviation of  $\pm 0.1$  cm (resolution of the ruler). The only deviation from the values in Table 4 was 28.643 cm, which could not be measured exactly with the ruler used and hence had to be rounded to 28 cm. This also ensured that the measurements did not go beyond the edge of the panel. The hand-drawn scale was used to position the tip of the fibre optics at the defined heights. To get the correct distances, the size of the pistol grip also had to be taken into account. The horizontal pole was coated with black tarpaulin material and for the vertical pole a rectangular piece of



black tarpaulin was adhered to the one side of the rod facing the panel. This allowed the different height levels to be read and still prevented the measurements from interference by unwanted reflected radiation from the shiny rod. The rest of the setup corresponded to the default setup (clean, levelled *Spectralon* reference panel, the appliance installed at 1 m above the ground). The reference setup was positioned in approximately three metres distance to the experimental setup and was built up according to the default setup (see Section 2.4). Both appliances were positioned perpendicular to the solar principal plane and were corrected in their alignment during the experiment. It was always ensured that the two *Spectralon* panels and the pistol grip respectively fibre holder were always levelled perpendicular to the force of gravity and the pistol grip and fibre holder, hence pointing nadir. The *ASD FieldSpec 3 # 16007* was used for the experimental measurements and the *ASD FieldSpec 4 # 18130* for the reference measurements. The spectroradiometers were properly warmed up for at least one hour previous to the data collection. The instrument settings were set to an internal average of 25 spectra for the spectra acquisition and 100 spectra for the *DC* measurements (according to the default setup).

In a first step, both field spectroradiometers and the two reference panels were cross-calibrated. The two fibre optic tips of the spectroradiometers were inserted into the fibre holder of the reference setup and 30 spectral radiance measurements were collected simultaneously. Further, the white reference panel of the reference setup was switched with the panel of the experimental setup and another 30 readings of this panel were acquired simultaneously. The experimental measurements were started by the acquisition of spectral data at a height of 30 cm from the fibre optic tip to the panel surface. While performing the experimental measurements, the reflected solar irradiance was continuously measured by the reference setup (at the default distance of 12 cm). For each of the different distances to the panel, which are shown in Table 4, 30 measurements were conducted. At a height of 30 cm, the *FOV* projects an area onto the panel that is larger than the panel area. For 28.643 cm, the diameter of the area would be exactly the length of one panel side (if the pistol grip is pointed at nadir and exactly at the centre of the panel). With a height of 12 cm above the panel (defined as the default height), the diameter of the footprint is about 5.3 cm. The first measurement (at a height of 30 cm) was obtained at 14:13 CEST and the last measurement at 14:51 CEST (at 2 cm). After the data collection, a second cross-calibration (end time: 15:04 CEST) of the spectroradiometers was performed for both *Spectralon* panels in the same way as the first cross-calibration (start time 14:04 CEST). The spectroradiometers were operated remotely from a distance of at least 2 m.

## 5.2 Data Analysis

The experimentally measured data sets were influenced by several different factors. In order to obtain results where the parameter of the distance to the panel was isolated (hence the only parameter affecting the measured values), it had to be corrected for all other factors. Due to the same setup of the reference and the experimental installation, some influencing parameters could already be eliminated. However, there was still the need for correction for the following factors: (1) the different instruments used in the reference and experimental setups, (2) the two different white reference panels, (3) the influence of the pistol grip, which was only used in the experimental setup, and (4) the change in solar irradiance over time. To guide through the process of data analysis, a data flow diagram was designed to provide an overview of the different analysis steps (Fig. 5). The acquired data consisted of the nine plus two tilted sets of measurements (as mentioned in Section 4) obtained at different heights above the panel, which are shown in Table 4. As mentioned before, the tilted measurements were obtained to analyse whether there is a significant difference in the measurement result compared to a fibre optic tip pointing nadir. Unfortunately, due to time constraints, this matter was not investigated further, but should be considered in the future. For the subsequent analysis, the two measurements had hence to be removed from the data set. It was assumed that the potential influence of a tilted fibre optic cable would distort the analysis due to the addition of another influencing variable (the tilt).

Additionally, the measurement at the greatest distance to the panel of 30 cm also had to be removed from the data set. Having conducted measurements at this distance resulted in a projected *FOV* that overlapped the panel area, which led to a measurement that included other materials than just the *Spectralon* panel. Of course, it would also have been an interesting study to investigate the influence of such an overlapping projected *FOV*. However, it was not a feasible data set to achieve the goal of this experiment. In order to obtain a correction model as a result of this study, a set of values influenced by an additional matter could not be used, but would rather have distorted the result. Hence, a total of eight suitable data sets were identified for the subsequent analysis.

### 5.2.1 Cross-Calibration of the Instruments and Panels

Since two different instruments as well as *Spectralon* panels were used for the data acquisition, the mentioned cross-calibration of the experimental measurements and the reference measurements was necessary [7]. The aim was to convert the measurements acquired with the experimental spectroradiometer and the experimental white reference panel and make them comparable with the measurements obtained with the reference spectroradiometer and the reference white panel.

For this purpose, the mentioned cross-calibration measurements were carried out before (pre) and after (post) the experimental measurements (see Section 5). Hence, two cross-calibration data sets were available for the correction. Due to the cross-calibration, there was no need to apply the calibration correction factors of the two panels mentioned in Section 2.3.2 in order to make them *NIST*-traceable.

However, before applying the cross-calibration and further thematic processing, a correction for the jump at the overlapping areas of the detectors (as mentioned in Section 2.3.1) had to be applied. The *RSL* in-house tool *RFL Calculator* was used for this jump correction, which is a *MATLAB*-based tool [64] that performed a parabolic interpolation at the detector joints. Once the correction was applied, further processing could be continued.

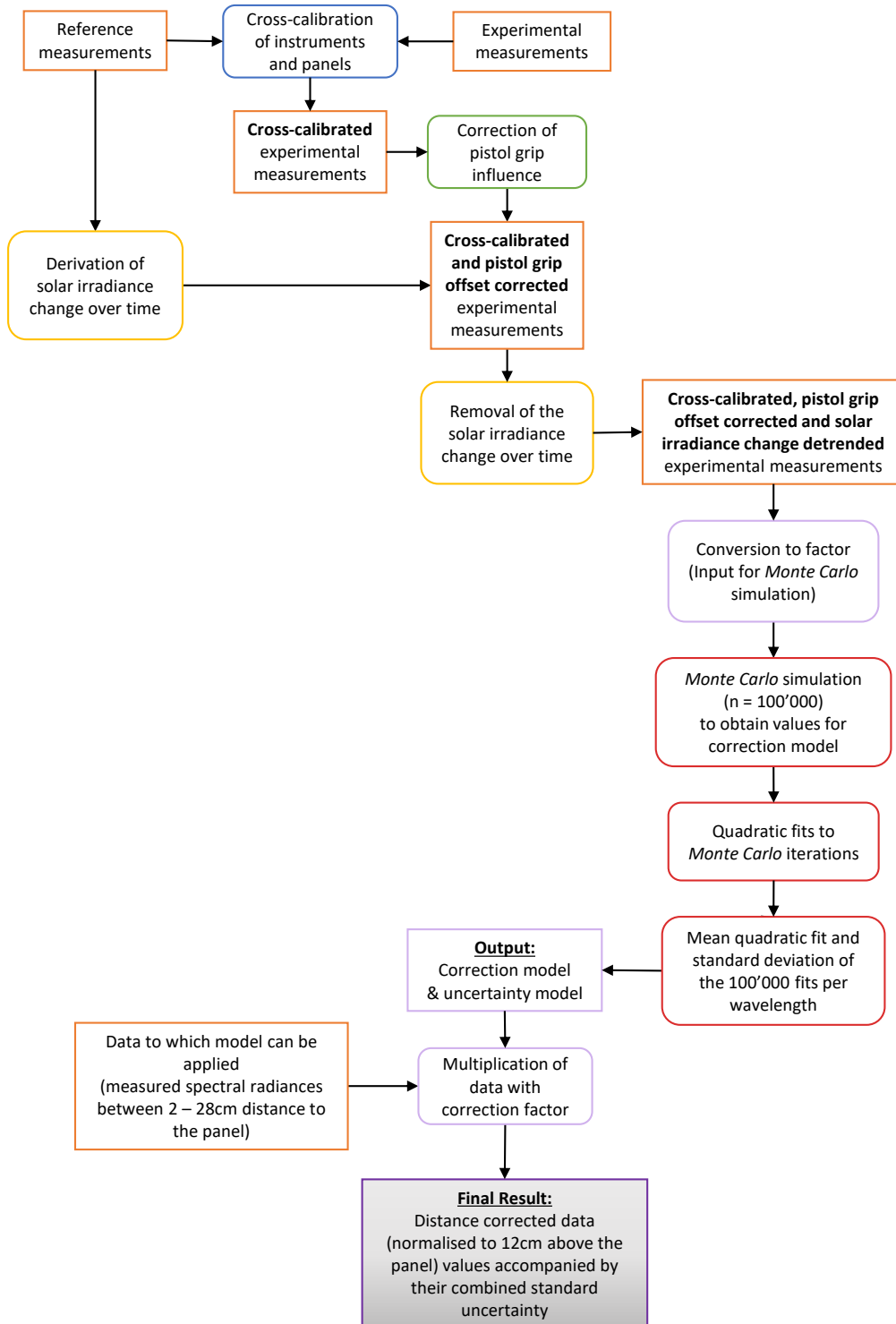


Figure 5: The data flow diagram, illustrating the main steps of the derivation of the correction model.

In an ideal case, one would assume that both the instruments and the reference panels would not differ from each other and the cross-calibration factor would be equal to one. Unfortunately, this was not the case in practice. Due to the usage of the white reference panels over the years, they have been worn to varying degrees. The instruments also differ slightly in their characteristics. As mentioned in Section 2.3.1, in addition to the individual instrument noise, the different spatial positions of the optical fibres of each instrument also had an influence on the measurement, especially because some of the fibres were broken. The two cross-calibration factors derived from the cross-calibration measurements (see Fig. 6) were hence each computed as follows:

$$xcal\_factor = \frac{RefASDRefP}{ExpASDExpP} \quad (16)$$

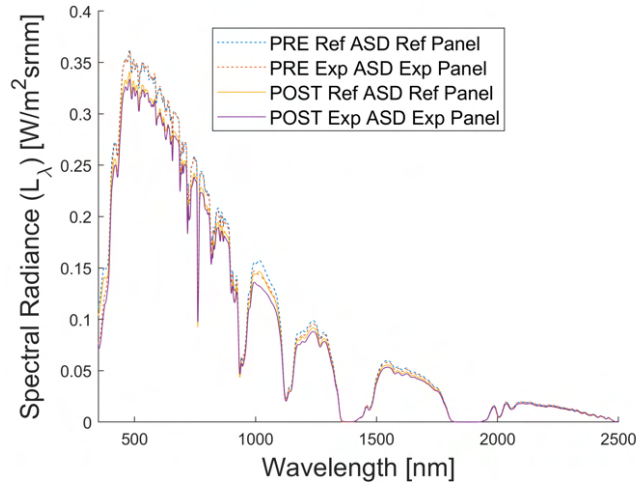


Figure 6: The mean measured spectra used for the cross-calibration of the instruments and panels.

Furthermore, the cross-calibration factors ( $xcal\_factor$ , once from before and once from after the experimental measurements) allowed a linear interpolation of cross-calibration factors to all the acquisition time stamps of the experimental measurements (see Fig. 7 and 8). Thus, it was not necessary to use the mean value of the pre or the post cross-calibration factor, but factors that corresponded to the actual time stamps of the experimental data collection. The interpolation was implemented by applying a *Monte Carlo* simulation, once using the mean pre cross-calibration factors per wavelength and once the mean post cross-calibration factors per wavelength as inputs ( $xcal\_factor$ ), as well as their so far propagated uncertainty per wavelength ( $u(xcal\_factor)$ ) (see Equation 17) [29]. The detailed calculation of the uncertainty will be presented in Section 5.3.1. 100'000 *Monte Carlo* iterations of the pre and post cross-calibration factors were generated, to which 100'000 linear interpolations were applied to obtain the cross-calibration factors at the different acquisition time stamps of the experimental measurements. The mean linear interpolation per acquisition time stamp and per wavelength was used as the final cross-calibration factor for the experiments ( $xcal\_factor\_MC$ ). This approach allowed to obtain the best estimated cross-calibration factor for the experimental measurements. Also, it allowed to receive an uncertainty value by obtaining the standard deviation of the 100'000 linear interpolations per distance to the panel and wavelength (see Section 5.3.1).

$$xcal\_factor\_MC = \frac{u(xcal\_factor) \cdot randn(100000)}{+xcal\_factor} \quad (17)$$

Hence, a simple calibration of the data sets was achieved by multiplying the interpolated mean factor by the corresponding spectral radiance of the data sets at the different distances. As a result, the measurements were simulated as if they had been obtained using the reference instrument and the reference panel.

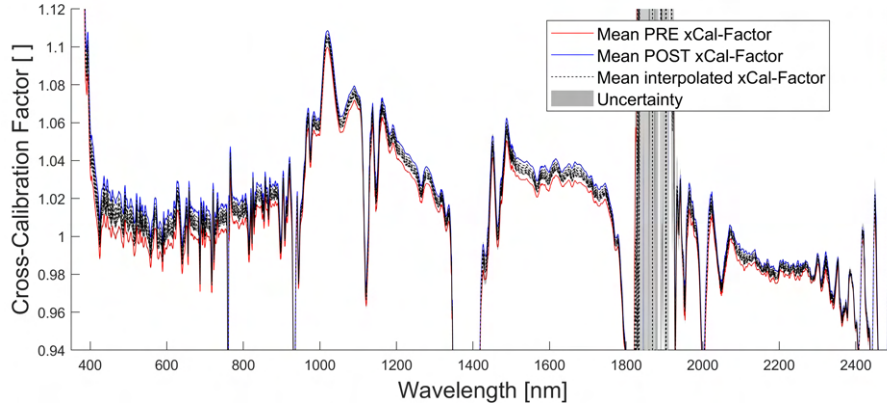


Figure 7: Mean pre and post cross-calibration factors and mean time-interpolated cross-calibration factors per distance measurement as well as their interpolated uncertainty for the entire wavelength range of the instruments (350 - 2500 nm).

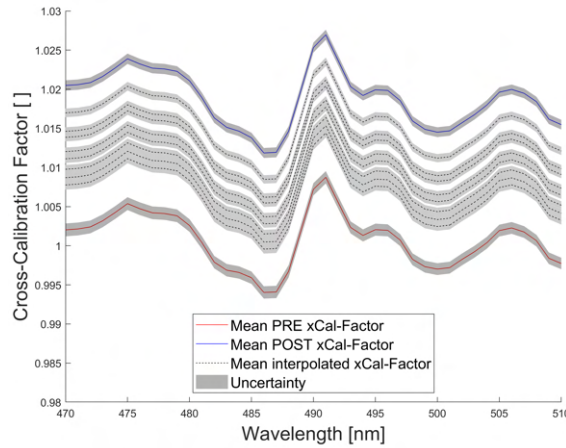
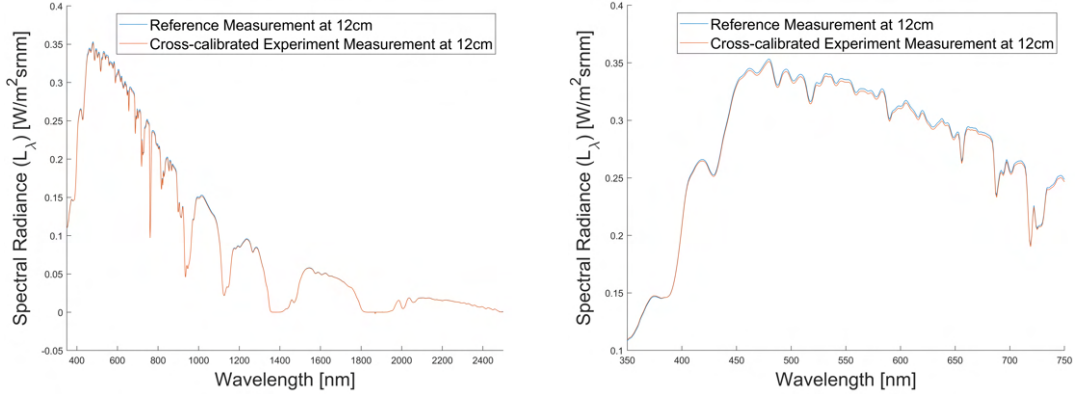


Figure 8: Zoom (470 - 510 nm) on the mean pre and post cross-calibration factors and mean time-interpolated cross-calibration factors per distance measurement as well as their interpolated uncertainty.

### 5.2.2 Correction of the Pistol Grip Offset

At this point in the data analysis, it was hence assumed that the appliance used to hold the fibre optic tip was the fibre holder for the experimental setup. However, this was not the case. Rather, the fibre optic tip was fed into a pistol grip and mounted to the rod (see Fig. 4). Therefore, the data had to be corrected for the influence of the pistol grip

on the measurement. The difference caused by the different cable support (fibre holder versus pistol grip) is well visible in the data set (see Fig. 9), resulting in the necessity of a correction.



(a) Entire wavelength range of the instruments.

(b) Zoom on the visible range (~350 - 750 nm).

Figure 9: The reference measurement at a distance of 12 cm to the panel and the cross-calibrated experimental measurement at the same distance revealing the influence of the pistol grip.

Therefore, the difference between the experimental measurement obtained at the distance of 12 cm, which corresponded to the chosen default height, and the reference measurement acquired in the same time span was calculated. This offset was further added to (or subtracted from, depending on the wavelength) the cross-calibrated experimental measurements. Since both the reference measurements and the experimental measurements each consisted of several spectra, the arithmetic mean of both of the data sets per wavelength was used to perform this calculation of the difference.

### 5.2.3 Correction for the Change in Solar Irradiance Over Time

Furthermore, it was necessary to correct for the change in solar irradiance for the duration of the experiment, since the solar irradiance increases until local noon and decreases thereafter. The two spectroradiometers did not collect the spectral data exactly at the same time due to differences in the instruments. For instance, the spectroradiometer #16007 (used for the experiments) had a higher frequency in collecting the spectra with the same settings as the reference spectroradiometer #18130. Hence, fewer data values were provided by the reference instrument. Unfortunately, it also occurred that the reference spectroradiometer sometimes experienced a time delay when saving the spectra. This led to additional cases where due to a lack of matching time stamps, fewer measurements were available for the reference instrument (e.g., see Fig. 10, Subfigure 1, where only two reference measurements matched the experimental measurements at a distance of 10 cm). Nonetheless, the reference data set provided a fair representation of the change in solar irradiance over time (see Fig. 10, Subfigure 1). Thus, the following procedure was applied to the entire spectral range of the spectroradiometer: In order to eliminate the influence of varying solar irradiance, a function had to be found that best describes the change in solar irradiance over time. From literature it is known that solar irradiance shows slight fluctuations within a high temporal resolution (minutes to hours) [32]. Therefore, a function was fitted to the fluctuations to use for the trend removal. This meant that

the mean value per distance cluster (30 readings) was used to obtain a fluctuation trend over time (see Fig. 10, Subfigure 1). Per reference measurement cluster, 2 - 32 reference measurements were available, which were acquired in the same time span. Therefore, the arithmetic mean per distance cluster was computed. The eight derived arithmetic mean values were further used to calculate the difference of solar irradiances at all distances to the panel to the solar irradiance of the default distance of 12 cm, in order to obtain the varying intensities of solar irradiance due to the different acquisition times. This meant that the mean reference measurement at a distance to the panel of 12 cm (normalisation basis) was subtracted from each mean reference measurement of all the different distances (see Equation 18).

$$\Delta L_{solar\_detrnd\_all\_to\_12cm\_ref} = L_{solar\_detrnd\_all} - L_{solar\_detrnd\_12cm} \quad (18)$$

In a further step, this delta was subtracted from all the experimental measurements to remove the trend of the solar irradiance changing over time (see Equation 19 and Subfig. 2 and 4 in Fig. 10). At this point, no arithmetic mean of the experimental measurements was derived, hence the delta (which is one arithmetic mean value per distance to the panel and wavelength) was subtracted from each of the 30 experimental values per corresponding distance cluster (see Fig. 10, Subfigure 4).

$$L_{solar\_detrnded\_exps} = L_{exp\_xcalibrated\_PG\_offset\_corr} - \Delta L_{solar\_detrnd\_all\_to\_12cm\_ref} \quad (19)$$

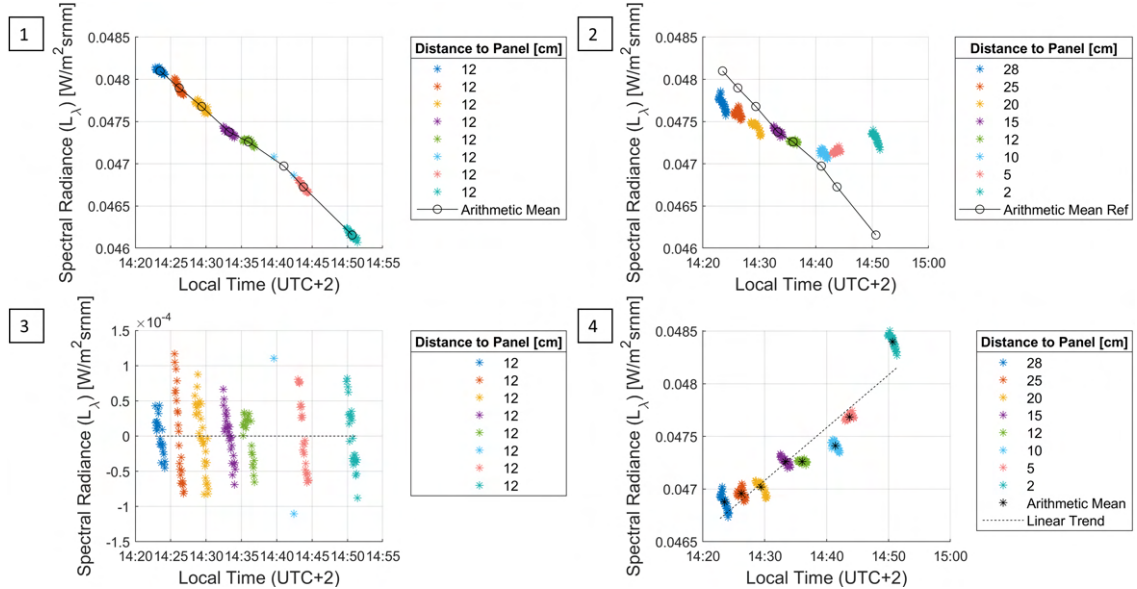


Figure 10: Removal of the solar irradiance change over time from the cross-calibrated and pistol grip offset corrected experiments at the exemplary wavelength 1650 nm. 1: Reference measurements, 2: Experimental measurements, 3: Solar irradiance change detrended reference measurements, 4: Solar irradiance change detrended experimental measurements.

The eight distances were still found in a cluster of 30 measurements, each representing one height above the panel. In Subfigure 4 of Fig. 10 it is visible that the values within one cluster varied quite intensively in their spectral radiance values over a very short period of time. However, it would have been expected that these 30 measurements rather coincided into one single point, or in this case a horizontal line (due to the time axis), than being distributed among a point cloud. The intensities of spectral radiances in a cluster should have not varied that much after removing the time trend, as solar fluctuations tend to occur within minutes rather than seconds. Because the resulting measurements did not behave as expected, some investigations were conducted, which are presented in the subsequent section, to find out whether the instrument was responsible for some of these variations.

#### 5.2.4 *Excursus: Broken Fibres and Bending of the Fibre Optic Cable*

As indicated in Table 2, both instruments used contained at least one broken fibre. One assumption was that there was variation in the spectral radiance due to these broken fibres. Thus, if the fibre optic cables would be bent, it should become observable in the spectral radiance intensity if these broken fibres accounted for some variation in comparison to a fibre optic bundle that did not contain broken fibres.

A second matter to consider was whether there were variations in the intensity of the measured spectral radiance due to movement of the cable in general. Hence, also instruments that did not have broken fibres would have been affected by the bending of the fibre optic cable. These assumptions were also based on the findings of Kuester et al. [34].

In order to obtain a data set to test the potential influence of broken and moved fibres, laboratory measurements were performed. The three *ASD FieldSpecs* #16007, #18130 and #18739 were warmed up for at least two hours (#16007 and #18130 are the instruments that were used for the main experiment). Table 2 shows that the instrument #16007 had two broken fibres belonging to the SWIR1 range and #18130 had one broken VNIR fibre. In the case of instrument #18739, all fibres were intact. The fibre holder was attached to one end of a rod assembly, the other end of which was screwed into a worktable. The fibre optic tips of the three spectroradiometers were fed into the fibre holder, which was positioned in front of an integrating sphere (a *HELIOS Uniform Source System*, *Labsphere Inc.* [36] [37]). The integrating sphere xenon lamp (*HELIOS XEL - Xenon External Lamp* [36]) was used as a stable artificial light source. Initially, 100 measurements were collected per instrument, with the cables in a static position. After obtaining these data sets, another 100 measurements were acquired, this time with the three fibre optic cables dynamically bent by hand at different angles throughout the measurement procedure. The two data sets were then compared by calculating the standard deviation per measurement series and instrument.

Fig. 11 shows that there was indeed a variation in intensity when the fibre optic cable was bent for all the three spectroradiometers tested. However, it was not clear from the figure whether broken fibres were actually responsible for some of the variation. In fact, the spectroradiometer which had no broken fibres showed a larger standard deviation than the field spectroradiometer with two broken fibres when the cables were twisted. Hence, it could not be said if the variation in intensity came from the broken fibres or from bending the fibre optic cable.

In any case, it was necessary to consider this variation in intensity and to include it in the form of uncertainty. This uncertainty was hence a mixture of the instrument noise, the jump correction as well as the bending of the fibre optic cable and potentially broken



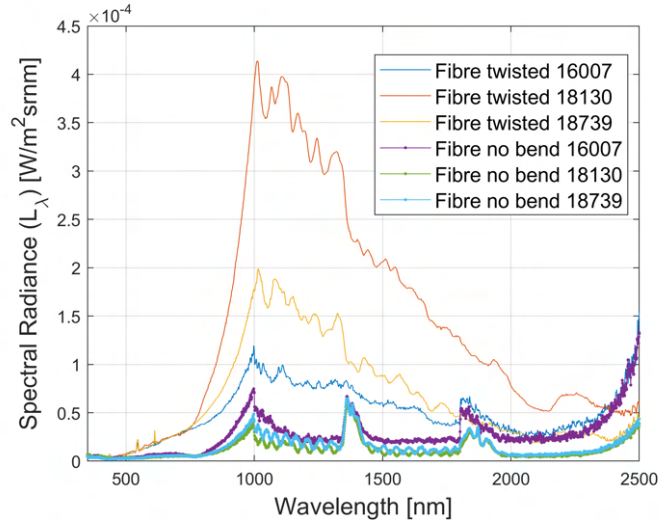


Figure 11: Standard deviations of the test measurements obtained with the three instruments. Once the fibre optic cables were twisted by hand and once in a static state.

fibre optics. Whenever the cable is moved, this uncertainty has to be taken into account. Since these measurements were conducted under laboratory conditions, the influence of the atmosphere and the solar irradiance was missing. A comparison of the obtained laboratory uncertainties with the uncertainty received from the actual experiments performed outdoors concluded that the latter uncertainty was even greater.

Hence, the uncertainty of the actual experiments was used for the further calculation of the correction model. Nonetheless, this topic of a bent fibre optic cable needs to be further investigated and, once isolated, added to the uncertainty budget.

Unfortunately, however, even within the framework of the above investigations, the problem of not having point-shaped clusters of values obtained at the same height remained unsolved. It was assumed that the source of such scattered values was more likely a problem caused by the instrument or the conditions of this particular data acquisition. To confirm this theory, it would therefore be necessary to repeat the experiment. However, since the latter was not possible within the scope of this thesis, the analysis was continued with the available data. For a comprehensive analysis, however, a future repetition of the measurements is strongly recommended.

### 5.2.5 Calculation of the Correction Model

Returning to the cross-calibrated, pistol grip offset corrected and solar irradiance change detrended experimental measurements, these had to be converted into factors that could be multiplied by a measurement obtained at a distance between 2 and 28 cm. The result of the multiplication of the data by these factors were spectral radiances normalised to the standard distance of 12 cm above the panel. To obtain the factors, the cross-calibrated, pistol grip offset corrected and solar irradiance change detrended experimental measurements at the default distance were divided by all the other experimental measurements in the same state at the other heights.

Hence, the experimental data was converted to factors which were corrected for the instrument and the panel, as well as for the influence of the pistol grip and the changing solar irradiance over time. They were further used as input values for a *Monte Carlo* simulation to generate the correction model.

The arithmetic mean of the factors per distance cluster as well as the uncertainty propagated so far (see Section 5.3 for the detailed calculation) were calculated and used as input for the *Monte Carlo* simulation according to Equation 20.

$$MC_{outputs} = u(CM_{inputs}) \cdot randn(100000) + \overline{CM_{inputs}} \quad (20)$$

100'000 random simulations were generated for each of the eight distances to the panel. The first hundred are visualised in Fig. 12.

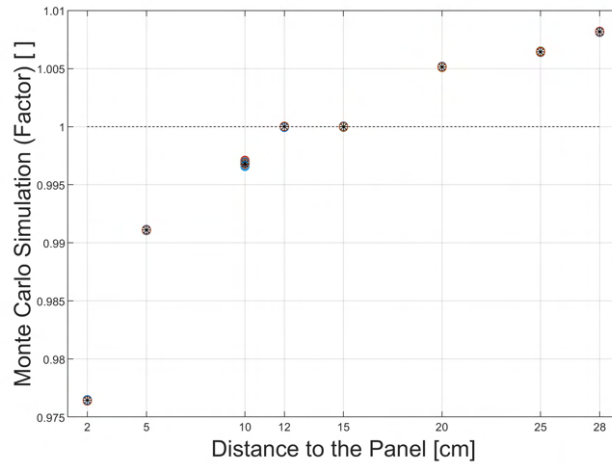


Figure 12: Visualisation of the 100 first *Monte Carlo* iterations to generate the correction model at the exemplary wavelength 1650 nm (SWIR).

Through each of the 100'000 iterations, a quadratic function (second degree polynomial) was fitted to derive a model that could correct for all distances between 2 and 28 cm (see Fig. 13). The coefficients of the mean quadratic fit per wavelength were derived as well as the standard deviation computed from the 100'000 fits per distance and wavelength. The coefficients could be used to compute the functions that provided the final correction model. The standard deviation evaluated for the initial input distances (2, 5, 10, 12, 15, 20, 25 and 28 cm) provided the associated propagated uncertainties at these distances. The mean *Monte Carlo* simulation values per distance and wavelength were computed to assess the goodness of fit of the correction model. The difference (residuals) of the correction model and the mean *Monte Carlo* simulation values was also calculated for evaluation purposes (see Section 6.3). The *root mean square error (RMSE)* was assessed for the entire spectral range (350 - 2500 nm) for all the different distances to the panel.

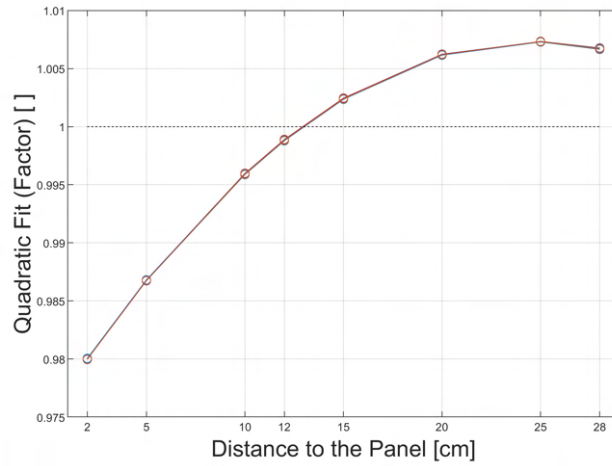


Figure 13: An example of the quadratic fits applied to the *Monte Carlo* simulations: The first 100 iterations for the wavelength 1650 nm (SWIR).

As the final applicable output, the mean coefficients per wavelength producing the correction model can be evaluated at any distance  $x$  between 2 and 28 cm. The output of the correction model will then be multiplied by the measurement obtained at distance  $x$ . The resulting value is the correction of the initial measurement to the default height of 12 cm distance to the panel per wavelength.

To include the uncertainty of the correction model, the *combined standard uncertainty* as well as the *expanded uncertainty* were computed. The detailed derivation of the uncertainty values is discussed in the subsequent Section 5.3.

### 5.3 Propagation of Uncertainty

The calculation of the propagated uncertainty of this data set followed the procedure described in Section 1.3.1 of this thesis and thus the best practice approach recommended by the *GUM* [28] and its supplements [29]. Hence, the *Gaussian* law of propagation was applied for the calculation of the propagation of uncertainties [28].

A tree diagram was created as a reference and visual aid for the uncertainty analysis performed in the upcoming section (Fig. 14). It outlines all the important steps of the analysis and indicates where uncertainties occur and how they propagate. The subsequent description of the uncertainty derivation will hence refer to the tree diagram.

The following uncertainty analysis describes type A uncertainties where the data acquisition was carried out under repeatability conditions (30 measurements per data set) [28]. In general, it was assumed that the used data sets comply with the *CLT*. As with any analysis, there were unknown uncertainties of different measures that could not be assessed within the scope of this work and were therefore not included in the uncertainty budget. Examples of unknown uncertainties in this analysis as well as with in-situ spectroradiometric measurements in general are the instrument noise, the non-linearity or the temporal (in)stability of an instrument, as well as unknown environmental errors such as the effects of humidity, temperature or stray light [40] [68]. Further experiments and modelling would be required to determine estimates of the currently unknown errors. One additional uncertainty that was known to exist, but was not computed within the scope of this thesis, was the uncertainty arising from the jump correction of all spectra. In a future study, this is certainly a part of the analysis where uncertainties need to be estimated.

For simplicity, all unknown uncertainties were assumed to be zero and were denoted as  $u(0)$  in the uncertainty tree diagram (Fig. 14). Therefore, the final uncertainty budget is an underestimate of the actual budget. As mentioned in Section 1.3.1, the derivation of covariance matrices (the second term of Equation 4) is a rather complicated, time-, computational- and data-intensive step. In order to stay within the scope of this work, the calculation of the covariance was omitted. As a result, the *combined standard uncertainty* computed in this thesis is underestimating the actual uncertainty of the calculated correction model and must be treated with caution. This must be given particular consideration when applying the model.

All the different influencing estimated input quantities of the correction model calculation were either spectral radiances [ $W/m^2srnm$ ] or were without units (e.g., factors). The propagation of uncertainty followed a linear summation of the uncertainties of the input quantities, weighted by their corresponding sensitivity coefficients and propagated following the *Gaussian* law of propagation [28].

In the case of this experiment, the measurand  $Y$  were the three coefficients per wavelength that define the correction model. They were computed by performing several processing steps (see Section 5.2), which generated and propagated uncertainties.

As a simple overview, the main processing steps could be referred to as input parameters of an overall function that provided the coefficients of the correction model as output. Thus, the following elements were part of this function: The cross-calibration of the two setups (*xcal*), the influence of the pistol grip (*PG*), the detrending of the solar irradiance change over time (*detrend*) and the fitting of a quadratic function to generate a correction model (*quadrFit*).

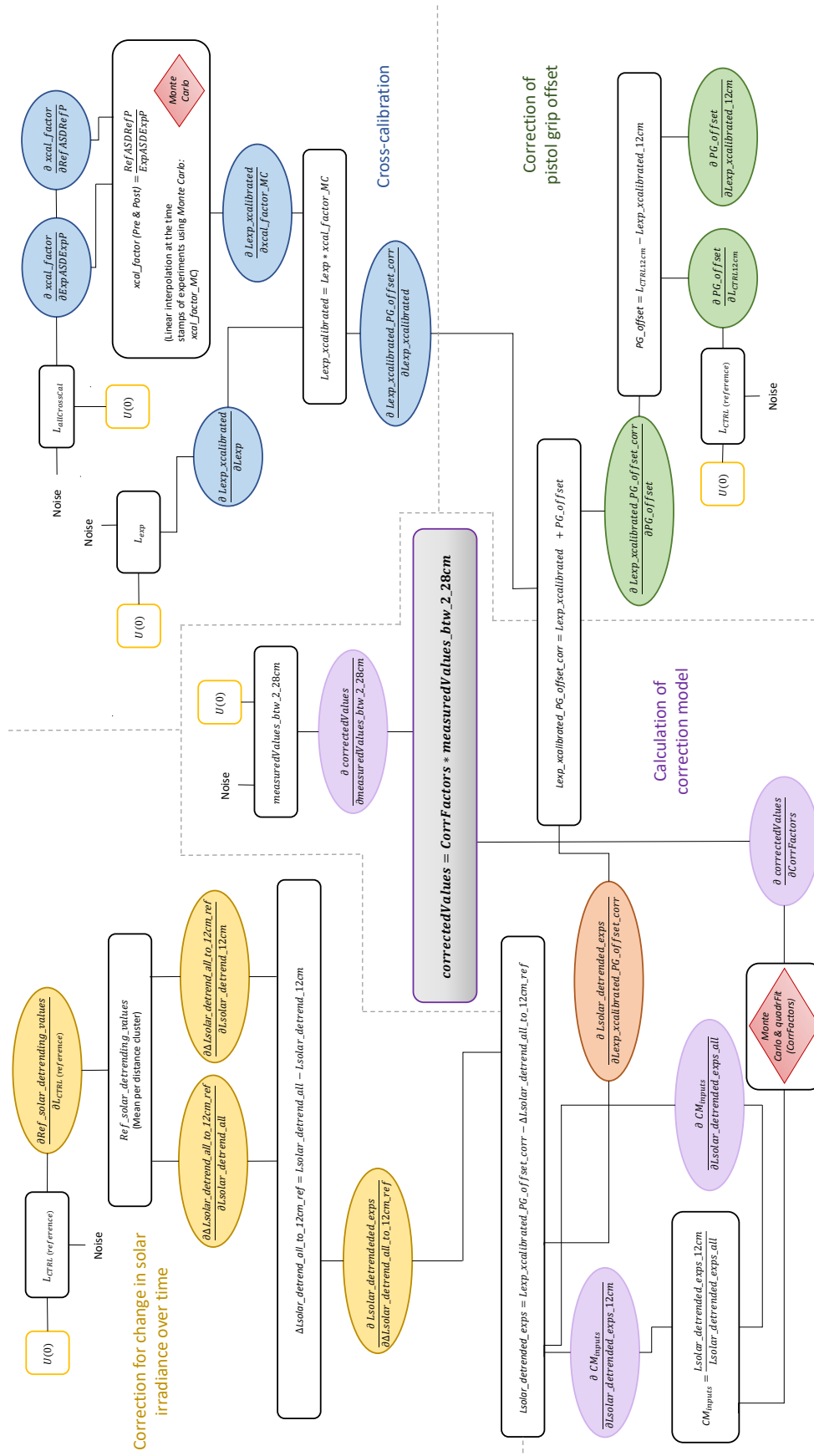


Figure 14: The tree diagram presenting the uncertainty propagation of the data analysis.

Mathematically, this could be expressed as follows:

$$Y = f(X_1, X_2, \dots, X_N) = f(xcal, PG, detrend, quadrFit) \quad (21)$$

Hence, the best estimated output of  $Y$ , which is  $y$ , was written as:

$$y = f(x_1, x_2, \dots, x_N) = f(xcal, PG, detrend, quadrFit) \quad (22)$$

The *combined standard uncertainty*  $u_c(y)$ , which must be taken into account when applying the correction model, was therefore characterised by the same elements as stated in Equation 22. The general equation denoting the *combined standard uncertainty* can be taken from Section 1.3.1 (Equation 4).

### 5.3.1 Uncertainty Estimation of the Cross-Calibration

First, uncertainty values were calculated with the step of computing the arithmetic mean of the pre and post cross-calibration factors. The arithmetic mean of the different input measurements for the cross-calibration (30 measurements each) was derived to calculate the factors of the two cross-calibrations (before and after the experiment). All steps concerning the uncertainty propagation due to the cross-calibration can be extracted from the part indicated in blue of the tree diagram (Fig. 14).

The equation for deriving the pre as well as the post cross-calibration factor was the same as Equation 16 and is hence referred to as follows:

$$xcal\_factor = \frac{RefASDRefP}{ExpASDExpP}$$

where  $(RefASDRefP$  and  $ExpASDExpP) \in L_{allCrossCal}$  were the input measurements for the cross-calibration.

The equation to derive the uncertainty of the pre and post cross-calibration factors was written as:

$$\begin{aligned} u(xcal\_factor)^2(Pre\&Post) &= u(RefASDRefP)^2 \cdot \frac{\partial xcal\_factor}{\partial RefASDRefP}^2 \\ &+ u(ExpASDExpP)^2 \cdot \frac{\partial xcal\_factor}{\partial ExpASDExpP}^2 \end{aligned} \quad (23)$$

with the uncertainty of each of the individual cross-calibration measurements calculated according to Equation 7:

$$u(x_i) = \frac{\sigma_{x_i}}{\sqrt{n_{x_i}}}$$

where  $x_i$  was an input measurement for the cross-calibration,  $\sigma_{x_i}$  the standard deviation of  $x_i$  and  $n_{x_i}$  the sample size of  $x_i$  ( $i= 1 - 30$ ). The division by the square root of the sample size was due to the use of the arithmetic mean of repeated cross-calibration measurements (see Section 1.3.1).

The two sensitivity coefficients of the estimated input variables were given as follows:

$$\frac{\partial xcal\_factor}{\partial RefASDRefP} = \frac{1}{ExpASDExpP} \quad (24)$$

$$\frac{\partial xcal\_factor}{\partial ExpASDExpP} = -\frac{RefASDRefP}{ExpASDExpP^2} \quad (25)$$

The resulting uncertainty ( $u(xcal\_factor)(Pre\&Post)$ ) was calculated once for all the data sets obtained before the experimental measurements (pre) and a second time for all the data sets obtained after the experimental measurements (post).

As explained in Section 5.2.1, it was linearly interpolated between the pre and post cross-calibration factors to account for the different time stamps of the experiments using the arithmetic mean of 100'000 *Monte Carlo* simulations. Hence, the uncertainty of the pre and post cross-calibration factors ( $u(xcal\_factor)(Pre\&Post)$ ) was used as input for this *Monte Carlo* simulation. The standard deviation of the 100'000 linear interpolation iterations could be used per distance measurement and wavelength as the propagated uncertainty  $u(xcal\_factor\_MC)$  of this computation step.

In a second step, the influence of a bent fibre optic cable was evaluated. When examining the influence of a bent fibre optic cable, it was found that it does have an influence on the measurements, but could not be isolated within the scope of this work (see Section 5.2.4). Since uncertainties emerging from the experimental measurements themselves were greater than those resulting from the bending of the fibre cable in the laboratory, the influence of a bent fibre cable was neglected.

Hence, the standard deviation of the mean experimental measurements ( $u(Lexp)$ ) was derived by applying Equation 7.

The two uncertainties, that of the calculation of the cross-calibration factor ( $xcal\_factor\_MC$ ) and that of the experimental measurements ( $Lexp$ ) were propagated by multiplication according to the following equation:

$$Lexp\_xcalibrated = Lexp \cdot xcal\_factor\_MC \quad (26)$$

The propagated uncertainty estimate of  $Lexp\_xcalibrated$  could hence be denoted as:

$$\begin{aligned} u(Lexp\_xcalibrated)^2 &= u(Lexp)^2 \cdot \frac{\partial Lexp\_xcalibrated^2}{\partial Lexp} \\ &+ u(xcal\_factor\_MC)^2 \cdot \frac{\partial Lexp\_xcalibrated^2}{\partial xcal\_factor\_MC} \quad (27) \end{aligned}$$

with the sensitivity coefficients defined as:

$$\frac{\partial L_{exp\_xcalibrated}}{\partial L_{exp}} = xcal\_factor\_MC \quad (28)$$

$$\frac{\partial L_{exp\_xcalibrated}}{\partial xcal\_factor\_MC} = L_{exp} \quad (29)$$

### 5.3.2 Uncertainty Estimation of the Pistol Grip Offset Correction

More uncertainties occurred when correcting the pistol grip offset (green part of the tree diagram, Fig. 14). To compute the offset, the difference between the reference measurement obtained at the same time as the experimental measurement at the distance of 12 cm and the experimental measurement at the distance of 12 cm was calculated.

The equation for this step was:

$$PG\_offset = L_{CTRL12cm} - L_{exp\_xcalibrated\_12cm} \quad (30)$$

It was therefore necessary to propagate the two uncertainties resulting from the calculation of the cross-calibrated experimental measurement at a height above the panel of 12 cm, as well as from the derivation of the arithmetic mean of the reference measurement acquired at the same time as the experimental data set.

The propagated uncertainty was thus calculated as:

$$\begin{aligned} u(PG\_offset)^2 &= u(L_{CTRL12cm})^2 \cdot \frac{\partial PG\_offset^2}{\partial L_{CTRL12cm}} \\ &+ u(L_{exp\_xcalibrated\_12cm})^2 \\ &\cdot \frac{\partial PG\_offset^2}{\partial L_{exp\_xcalibrated\_12cm}} \end{aligned} \quad (31)$$

With  $u(L_{exp\_xcalibrated\_12cm})$  taken from the precedent uncertainty calculation of the cross-calibration and divided by the square root of its sample size, as well as  $u(L_{CTRL12cm})$  calculated according to Equation 7 (standard deviation of measurement and divided by the square root of its sample size).

The sensitivity coefficients were:

$$\frac{\partial PG\_offset}{\partial L_{CTRL12cm}} = 1 \quad (32)$$

$$\frac{\partial PG\_offset}{\partial L_{exp\_xcalibrated\_12cm}} = -1 \quad (33)$$



The pistol grip offset was further added (or subtracted, depending on the wavelength) to the cross-calibrated experimental measurements to apply the correction. Hence, this resulted in the following equation:

$$Lexp\_xcalibrated\_PG\_offset\_corr = Lexp\_xcalibrated + PG\_offset \quad (34)$$

With the associated uncertainties calculated as follows:

$$\begin{aligned} u(Lexp\_xcalibrated\_PG\_offset\_corr)^2 &= u(Lexp\_xcalibrated)^2 \\ &\quad + \frac{\partial Lexp\_xcalibrated\_PG\_offset\_corr^2}{\partial Lexp\_xcalibrated} \\ &\quad + u(PG\_offset)^2 \\ &\quad + \frac{\partial Lexp\_xcalibrated\_PG\_offset\_corr^2}{\partial PG\_offset} \end{aligned} \quad (35)$$

Due to the simple addition in the equation, the sensitivity coefficients were both equal to 1.

The resulting propagated uncertainty was thus the uncertainty associated with the cross-calibrated and pistol grip offset corrected experimental measurements  $u(Lexp\_xcalibrated\_PG\_offset\_corr)$ .

### 5.3.3 Uncertainty Estimation of the Correction for the Solar Irradiance Change Over Time

From the reference measurements, additional uncertainties arose due to the neutralisation of the change in solar irradiance over time (yellow part of the uncertainty tree diagram, Fig. 14).

To calculate the solar irradiance trend from the reference measurements, the arithmetic mean per measurement cluster of the eight different distances to the panel was derived (*Ref\_solar\_detrending\_values*). Hence, the uncertainty of the mean per cluster was computed by applying Equation 7.

As mentioned in Section 5.2.3, the next step in the data analysis was to obtain the difference in reflected solar irradiance with respect to the default height at 12 cm above the panel. Therefore, the mean reflected solar irradiance measured at the default distance (12 cm) was subtracted from the mean reflected solar irradiances of all other distances as stated in Equation 18.

The related uncertainty equation was denoted as:

$$\begin{aligned}
u(\Delta L_{solar\_detrend\_all\_to\_12cm\_ref})^2 &= u(L_{solar\_detrend\_all})^2 \\
&\cdot \frac{\partial \Delta L_{solar\_detrend\_all\_to\_12cm\_ref}}{\partial L_{solar\_detrend\_all}} \\
&+ u(L_{solar\_detrend\_12cm})^2 \\
&\cdot \frac{\partial \Delta L_{solar\_detrend\_all\_to\_12cm\_ref}}{\partial L_{solar\_detrend\_12cm}}
\end{aligned} \tag{36}$$

The used sensitivity coefficients were equal to:

$$\frac{\partial \Delta L_{solar\_detrend\_all\_to\_12cm\_ref}}{\partial L_{solar\_detrend\_all}} = 1 \tag{37}$$

$$\frac{\partial \Delta L_{solar\_detrend\_all\_to\_12cm\_ref}}{\partial L_{solar\_detrend\_12cm}} = -1 \tag{38}$$

Once the difference was obtained, the next step was to subtract it from the cross-calibrated and pistol grip offset corrected experimental measurements. The procedure led to the actual elimination of the estimated solar irradiance change over time that affected the experimental measurements. This step was the convergence of all three uncertainty calculations performed so far and the corresponding calculation can be taken from Equation 19.

The associated uncertainties are denoted as:

$$\begin{aligned}
u(L_{solar\_detrended\_exps})^2 &= u(L_{exp\_xcalibrated\_PG\_offset\_corr})^2 \\
&\cdot \frac{\partial L_{solar\_detrended\_exps}}{\partial L_{exp\_xcalibrated\_PG\_offset\_corr}}^2 \\
&+ u(\Delta L_{solar\_detrend\_all\_to\_12cm\_ref})^2 \\
&\cdot \frac{\partial L_{solar\_detrended\_exps}}{\partial \Delta L_{solar\_detrend\_all\_to\_12cm\_ref}}^2
\end{aligned} \tag{39}$$

with the sensitivity coefficients:

$$\frac{\partial L_{solar\_detrended\_exps}}{\partial L_{exp\_xcalibrated\_PG\_offset\_corr}} = 1 \tag{40}$$

$$\frac{\partial L_{solar\_detrended\_exps}}{\partial \Delta L_{solar\_detrend\_all\_to\_12cm\_ref}} = -1 \tag{41}$$

The resulting propagated uncertainty accompanied the cross-calibrated, pistol grip offset corrected and solar irradiance change detrended experimental measurements.

### 5.3.4 Uncertainty Estimation of the Correction Model

In a last step, the uncertainty of the correction model had to be calculated (purple part of the uncertainty tree diagram, Fig. 14). To obtain a correction factor that could be applied to distances to the panel between 2 and 28 cm, the results of Equation 19 at the distance of 12 cm to the panel had to be divided by all the other measurements of said equation:

$$CM_{inputs} = \frac{L_{solar\_detrended\_exps\_12cm}}{L_{solar\_detrended\_exps\_all}} \quad (42)$$

Therefore, the uncertainties were propagated once more to the uncertainty budget of the preliminary correction model:

$$\begin{aligned} u(CM_{inputs})^2 &= u(L_{solar\_detrended\_exps\_12cm})^2 \cdot \frac{\frac{\partial CM_{inputs}}{\partial L_{solar\_detrended\_exps\_12cm}}}{\frac{\partial CM_{inputs}}{\partial L_{solar\_detrended\_exps\_all}}}^2 \\ &\quad + u(L_{solar\_detrended\_exps\_all})^2 \cdot \frac{\frac{\partial CM_{inputs}}{\partial L_{solar\_detrended\_exps\_all}}}{\frac{\partial CM_{inputs}}{\partial L_{solar\_detrended\_exps\_all}}}^2 \end{aligned} \quad (43)$$

With the sensitivity coefficients denoted as:

$$\frac{\partial CM_{inputs}}{\partial L_{solar\_detrended\_exps\_12cm}} = \frac{1}{L_{solar\_detrended\_exps\_all}} \quad (44)$$

$$\frac{\partial CM_{inputs}}{\partial L_{solar\_detrended\_exps\_all}} = -\frac{L_{solar\_detrended\_exps\_12cm}}{L_{solar\_detrended\_exps\_all}^2} \quad (45)$$

The data, now in the state of a factor, were used as the input to a *Monte Carlo* simulation to get the best estimated values per distance and wavelength for a correction model. Hence, the uncertainty propagated so far also served as input for this same *Monte Carlo* simulation.

$$MC_{outputs} = u(CM_{inputs}) \cdot randn(100000) + \overline{CM_{inputs}} \quad (46)$$

The standard deviation of the 100'000 quadratic functions fitted to the *Monte Carlo* simulations was derived per distance to the panel and wavelength and served as the *combined standard uncertainty* for the eight initial distances to the panel of the correction model. However, since the standard deviations were only available for the initial eight distances, quadratic functions were fitted to these standard deviations to estimate the uncertainties for all heights between 2 - 28 cm.

To evaluate the goodness of fit of the model, the residuals and *RMSE* of the input uncertainty values and the quadratic fits were calculated.

To obtain the *expanded uncertainty* of the correction model, the results of the quadratic fit for the *combined standard uncertainties* were multiplied with a coverage factor  $k = 2$ , as it is the usual standard in metrology [28] [65].

Finally, with the last calculation of the *expanded uncertainty*, the uncertainty budget of the correction model was completely calculated.

The coefficients of the *combined standard uncertainty* (and thus of the *expanded uncertainty* by applying the preferred coverage factor) are available as matrices that can be applied to acquired measurements obtained within a distance of 2 to 28 cm to the white reference panel.

### 5.3.5 Uncertainty Estimation of the Applied Correction Model

Since the purpose of a correction model is to apply it to actual measurements, the further propagation of the uncertainty had to be considered when applying the model to newly acquired data. The equation for applying the correction factor is defined as:

$$correctedValues = CorrFactors \cdot measuredValues\_btw\_2\_28cm \quad (47)$$

Hence, the uncertainty of the data set to be corrected had to be taken into account (by applying Equation 7) and propagated along with the uncertainty of the correction model:

$$\begin{aligned} u(correctedValues)^2 &= u(CorrFactors)^2 \cdot \frac{\partial correctedValues^2}{\partial CorrFactors} \\ &\quad + u(measuredValues\_btw\_2\_28cm)^2 \\ &\quad \cdot \frac{\partial correctedValues^2}{\partial measuredValues\_btw\_2\_28cm} \end{aligned} \quad (48)$$

The sensitivity coefficients were given as:

$$\frac{\partial correctedValues}{\partial CorrFactors} = measuredValues\_btw\_2\_28cm \quad (49)$$

$$\frac{\partial correctedValues}{\partial measuredValues\_btw\_2\_28cm} = CorrFactors \quad (50)$$

The final measurements, corrected to a distance to the panel of 12 cm, were therefore accompanied by the *combined standard uncertainty* “ $u(correctedValues)$ ”.

To derive an *expanded uncertainty*, the *combined standard uncertainty* was again multiplied by the preferred coverage factor  $k$  (standard in metrology:  $k = 2$  [28] [65]).

## 6 Results

The first part of this section presents the correction model as the output of the data analysis (Section 5.2): The correction model for distances to the panel from 2 to 28 cm and over the entire wavelength range is shown as well as visualisations of correction model functions for exemplary wavelengths. Moreover, the modelled *combined standard uncertainty* and *expanded uncertainty* are quantified and presented. The last part of this section is dedicated to an estimation of the goodness of fit of the calculated models.

### 6.1 Correction Model

The result of the data analysis (see Section 5.2) was a correction model that corrected any distance from the tip of the fibre optic cable to the white reference panel from 2 to 28 cm to the default distance of 12 cm (Fig. 15). This correction model could be applied to the entire spectral range of a field spectroradiometer of the *ASD FieldSpec* range (350 - 2500 nm). For a measurement at a certain height between 2 and 28 cm, the corresponding correction factors were multiplied by the measured spectral radiances. Hence, the result of this multiplication normalised the initial spectral radiance values to a distance of 12 cm. Furthermore, the *combined standard uncertainty* (and hence also the *expanded uncertainty*) of the correction model was available for the corrected data set. Wavelength regions where atmospheric absorption features dominate were excluded from the model (see the gaps in Fig. 15). The absorption of the radiation is mainly by water vapour in the wavelength ranges around 930 - 960 nm, 1100 - 1160 nm, 1320 - 1490 nm, 1760 - 1980 nm, 2000 - 2020 nm and 2400 - 2500 nm [59]. However, the position of the atmospheric features was only an approximation based on [59]. The correction model in its entirety, covering the whole spectral range of an *ASD FieldSpec* 3 or 4 for the distances between 2 - 28 cm, is visualised in Fig. 15.

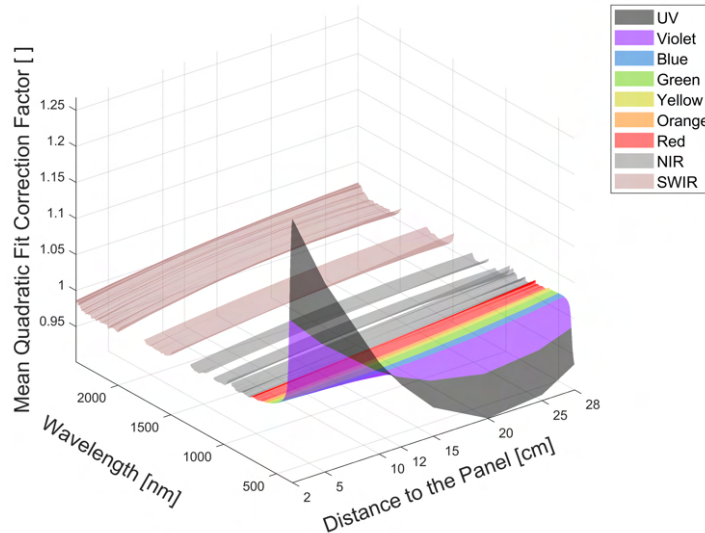


Figure 15: The final correction model per wavelength and distance to the panel (mean fitted quadratic function) with absorption features removed.

Each correction model function was accompanied by its *combined standard uncertainty* and its *expanded uncertainty* at a level of confidence of 95.45% ( $k = 2$ ). Both uncertainty estimates could be visualised as envelopes and were calculated according to the work flow described in Section 5.3. In the two Figures 16 and 17 twelve examples of correction

model functions at exemplary wavelengths are shown along with their *combined standard uncertainty* and their *expanded uncertainty* (applied coverage factor  $k$  of 2). The examples each represent a selected wavelength to show the variation across the entire spectral range of a field spectroradiometer.

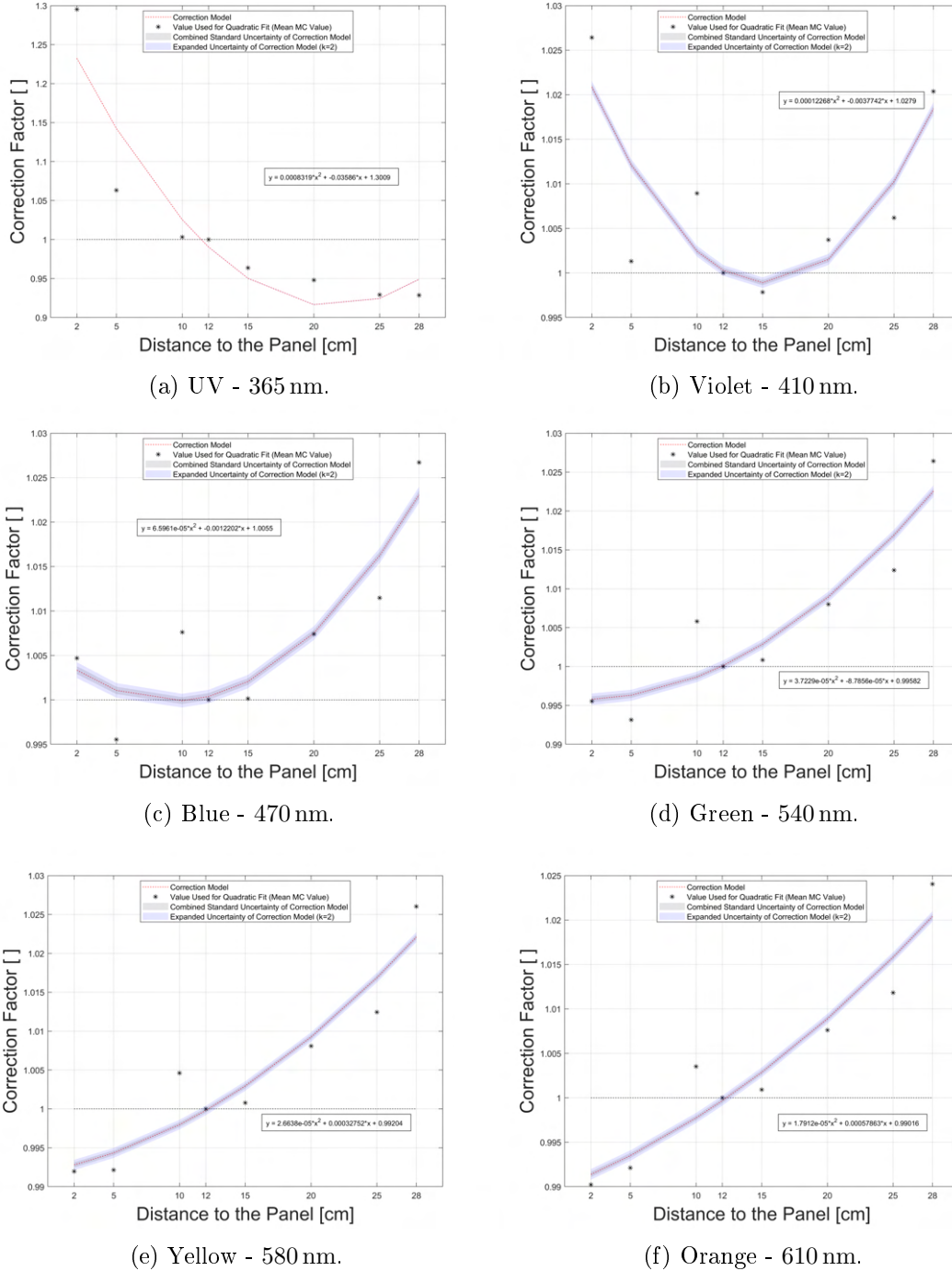
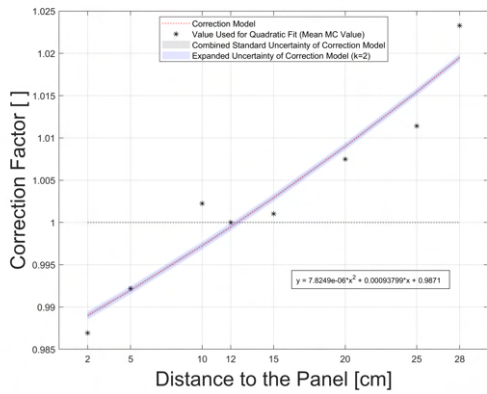
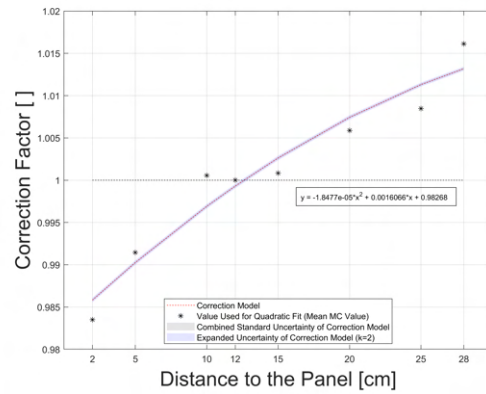


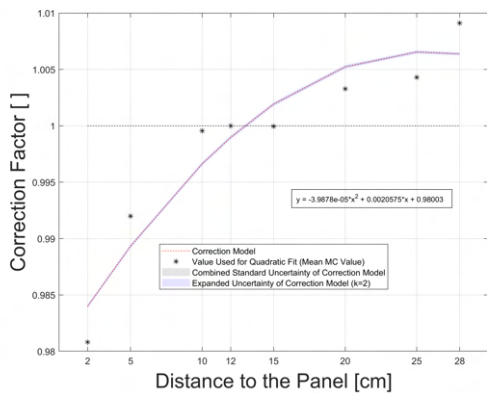
Figure 16: Exemplary correction model functions with their corresponding uncertainties to be applied to distances to the panel from 2 to 28 cm (UV - Orange).



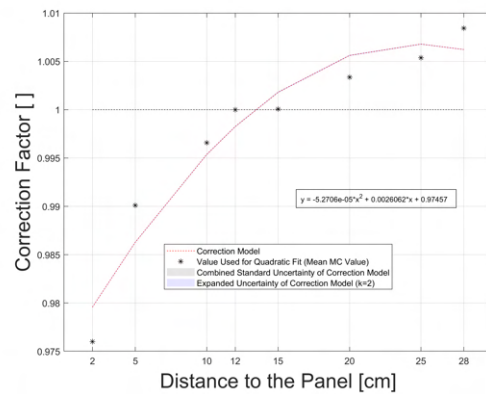
(a) Red - 670 nm.



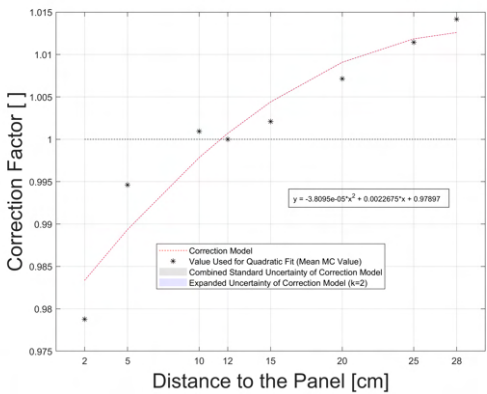
(b) NIR - 843 nm.



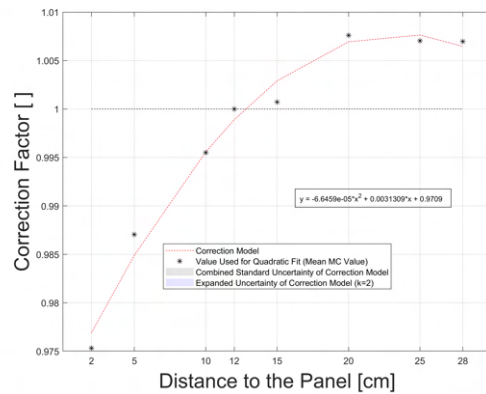
(c) NIR - 1000 nm.



(d) SWIR1 - 1600 nm.



(e) SWIR1 - 1750 nm.



(f) SWIR2 - 2200 nm.

Figure 17: Exemplary correction model functions with their corresponding uncertainties to be applied to distances to the panel from 2 to 28 cm (Red - SWIR).

Figure 15 illustrates that the correction model showed a fair amount of variation across the spectrum. Especially the *ultraviolet* (*UV*) (~350 - 380 nm) and also the violet part (~380 - 450 nm) of the EM-spectrum showed a different trend than the remaining wavelength range. The two mentioned parts showed a decline of the correction factors from a smaller to a larger distance to the panel, whereas the range from approximately blue to SWIR (~450 - 2500 nm) showed an increase towards larger distances.

The Figures 16 and 17 give a more detailed insight into the different regions of the electromagnetic spectrum and their correction factor characteristics. All correction models, divided by region, are also attached in the Appendix A to provide further information. They are represented once with their *combined standard uncertainty* (Fig. 26) and once with their *expanded uncertainty* (Fig. 27).

In general, a correction factor of one was expected to be applied at a distance of 12 cm, since this distance represented the chosen default distance. This meant that all other distances had to be corrected to 12 cm and hence a measurement collected at 12 cm needed no correction. Of course, this only applied if no effect other than a different distance to the panel influenced the measurement. Nevertheless, there will always be a very small correction factor also for the default height. This is due to the fact that the correction function is a fitted model (hence not perfect).

Figure 16a shows the correction function for the wavelength of 365 nm, representing an exemplary wavelength of the UV region. The correction factors showed a clear decrease in their values with increasing distance to the panel. At distances smaller than the default height (2 - 12 cm), the factors were therefore larger than one and at distances to the panel of 12 - 28 cm, the factors were smaller. From Appendix A (Fig. 26 and 27) it can be taken that the correction factors for 2 cm ranged between 1.133 and 1.271. This resulted in an average correction (arithmetic mean of the entire UV range) of approximately 22.04% of the initially measured spectral radiance, which had to be added to the data set obtained at 2 cm to simulate a measurement at 12 cm (see Table 5). For a distance of 28 cm the values varied from 0.9376 to 0.9824 and it was about 4.67% of the spectral radiance by which it needed to be reduced to simulate a height of 12 cm.

Table 5: Correction to the default distance in +/- percent of the measured spectral radiance.

| <i>Wavelength range / Distance to panel [cm]</i> | <b>2</b> | <b>5</b> | <b>10</b> | <b>12</b> | <b>15</b> | <b>20</b> | <b>25</b> | <b>28</b> |
|--|----------|----------|-----------|-----------|-----------|-----------|-----------|-----------|
| <b>UV</b>  | 22,04    | 13,51    | 2,46      | -0,86     | -4,65     | -7,81     | -7,03     | -4,67     |
| <b>Violet</b>                                    | 2,94     | 1,74     | 0,34      | -0,01     | -0,30     | -0,19     | 0,67      | 1,55      |
| <b>Blue</b>                                      | 0,25     | 0,06     | -0,02     | 0,04      | 0,22      | 0,76      | 1,63      | 2,29      |
| <b>Green</b>                                     | -0,37    | -0,34    | -0,13     | 0,01      | 0,28      | 0,88      | 1,68      | 2,25      |
| <b>Yellow</b>                                    | -0,70    | -0,55    | -0,19     | -0,01     | 0,30      | 0,93      | 1,69      | 2,21      |
| <b>Orange</b>                                    | -0,83    | -0,63    | -0,21     | -0,02     | 0,30      | 0,91      | 1,62      | 2,10      |
| <b>Red</b>                                       | -1,08    | -0,78    | -0,25     | -0,03     | 0,31      | 0,90      | 1,53      | 1,92      |
| <b>NIR</b>                                       | -1,54    | -1,02    | -0,29     | -0,04     | 0,29      | 0,70      | 0,96      | 1,03      |
| <b>SWIR</b>                                      | -2,18    | -1,41    | -0,38     | -0,05     | 0,36      | 0,80      | 0,95      | 0,90      |

A prominent feature was the flattening of the correction function as it approached the distance of 28 cm, where it even showed a slight upward trend towards the furthest distance. The correction function representing an example wavelength of the violet part of the electromagnetic spectrum (410 nm) is shown in Figure 16b. These correction functions did not show as clear a trend as the other wavelength ranges with respect to the different heights above the panel. The functions were rather fanned out U-shaped functions (see Appendix A, Fig. 26 and 27). From the same plot, it can be taken that the wavelengths behaved quite differently depending on whether they were closer to the UV part or the blue part of the spectrum. Compared to all other wavelength ranges, the violet part showed di-



verse correction function shapes and also varied in the magnitude of the correction factors within the different distances to the panel (between 1.006 and 1.133 for 2 cm and 0.9807 and 1.023 for 28 cm). For some wavelengths, the correction function never dropped below a value of one, implying that the measured values needed to be increased no matter at what distance to the panel they were measured. The mean percentages of the correction applied to this wavelength range can be found in Table 5. The difference in magnitude of the percent values between the UV range and the violet range was quite large. At a distance of 2 cm, for the violet part the measurement data had to be increased by a mean of 2.94 %, whereas the mean correction was 22.04 % for the UV range. The mean percentage of 1.55 % for a distance of 28 cm needed to be added again to the measurement in the violet wavelength range in contrary to the mean percentage at this distance of the UV range (-4.67 %). However, the mean percentages of the violet wavelength range have to be treated with caution due to the diverse behaviour of the functions.

In Figure 16c, the blue region (~450 - 500 nm) is represented by the wavelength 470 nm. In this range, the first complete change of trend was visible, where the correction factors were higher with larger distances of the fibre optic tip to the panel. At smaller distances to the panel, they slowly decreased to the value of one with each wavelength approaching the green range, while the correction factors continued to increase towards larger distances. As with some of the wavelengths of the violet range, the majority of correction functions of the blue range appeared to not have correction factors smaller than one at any distance to the panel (see Fig. 26 or 27 in Appendix A). Only a few global minima fell slightly below a value of one, mostly between a distance of 5 to 12 cm from the panel. This is also visible in Table 5, where it can be seen that the distance to the panel of 10 cm was the only mean correction in percent that reduced the measurements in their values. The correction factors ranged from 0.9994 to 1.006 (corresponding to a mean correction in percent of 0.25 %) for a distance of 2 cm and from 1.0226 to 1.0234 (2.29 %) for 28 cm.

Very similar correction model functions could be found for all wavelength ranges from green to red (~500 - 750 nm, represented by 540, 580, 610 and 670 nm in Figures 16 and 17). In general, distances smaller than the default distance correlated with correction factors below one and distances to the panel larger than 12 cm corresponded to correction factors larger than one. The correction functions had concave shapes, while the shapes tended to get less concave from green to red. Therefore, the functions for the red part of the spectrum were nearly linear fits. The correction factors varied for green from 0.9937 (2 cm) to 1.023 (28 cm), for yellow from 0.9921 (2 cm) to 1.023 (28 cm), for orange from 0.9913 (2 cm) to 1.023 (28 cm) and for red from 0.9869 (2 cm) to 1.024 (28 cm). Figures 26 and 27 in Appendix A show that the variation in correction factors per distance to the panel among all wavelengths of these individual ranges of the EM-spectrum was low and therefore the functions were of similar values. Table 5 shows that for all distances to the panel in the range of 2 to 20 cm, the deviations to be corrected were below 1 % (plus or minus), with the only exception of the 2 cm distance in the red wavelength range. For distances to the panel of 25 and 28 cm, the percentages were between 1.53 and 2.25 %.

The NIR range (~750 - 1400 nm) was represented by two exemplary wavelengths: 843 nm and 1000 nm (Fig. 17b and 17c). Both correction functions had a convex shape that got more extreme the longer the wavelengths. The correction factors for this range varied from 0.9803 to 0.9931 for a distance to the panel of 2 cm and from 1.005 to 1.024 for 28 cm (see Fig. 26 and 27 in Appendix A). This corresponded to mean percentage deviations for the NIR range of -1.54 % for a distance of 2 cm to the panel and 1.03 % for 28 cm (Table 5). The increasingly convex shape of the functions resulted in a flattening of the function at greater distances to the panel for NIR wavelengths closer to the SWIR region. It was

still the case that the functions increased in value from a smaller to a larger distance to the panel.

Figures 17d, 17e and 17f show three functions of the SWIR range (~1400 - 2500 nm). The correction factors ranged from 0.971 to 0.9889 for 2 cm and from 1.005 to 1.025 for 28 cm. The flattening towards the larger distances to the panel was also present within this region of the EM-spectrum. In general, the functions of the SWIR range behaved similarly to those of the NIR region. The mean corrections in percent reduced the measured spectral radiances by approximately 2.18 % at 2 cm above the panel and increased them by 0.90 % at a distance of 28 cm to the panel.

Overall, the percentage deviations were greatest in the UV range in relation to the entire spectral range, whereas the percentage deviations for the rest of the spectrum were in similar ranges.

## 6.2 Model of the Combined Standard Uncertainty

The modelled *combined standard uncertainty* accompanying the correction model is visualised as factors in Fig. 18. It indicates the upper and lower margins of the *combined standard uncertainty* factors per wavelength and distance to the panel. It should be remembered that the uncertainty shown is an underestimate of the actual uncertainty, as no estimated covariance was calculated and unknown uncertainties were not included.

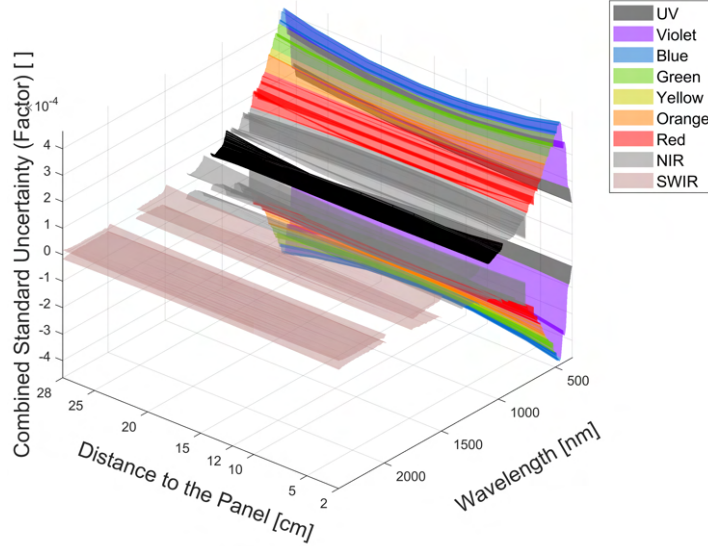


Figure 18: Factors of the *combined standard uncertainty* of the correction model per wavelength (fitted quadratic functions) with absorption features removed (the black part consists of many overlapping NIR wavelengths due to the 3D structure).

As with the correction model, there was also variation within the associated uncertainties. It is noticeable that the uncertainties seemed to be largest in the blue wavelength range and became smaller towards both ends of the spectrum.

Uncertainties (*combined standard uncertainties* as well as *expanded uncertainties*) of the same exemplary wavelengths over the nine selected ranges (UV, violet, blue, green, yellow, orange, red, NIR and SWIR) are also displayed in the Figures 16 and 17. However, for some of the exemplary wavelengths the uncertainties were so small that they could hardly be distinguished from the correction function (UV, NIR and SWIR range). Table 6 shows the mean *combined standard uncertainty* per wavelength range in percent of the measured spectral radiances for all the distances. The percentages were added as an envelope ( $\pm$ ) to the corresponding values of the correction model. The *combined standard uncertainties* described in the following refer to the uncertainty of the correction model. This means that if the correction model is applied to measured data, the uncertainty must be propagated once more according to the *Gaussian* law of propagation (see e.g., Fig. 24 or 25).

The mean *combined standard uncertainty* of the UV range reached values of 0.015 % (for 2, 5, 10 and 12 cm) to 0.021 % (28 cm). The mean uncertainty increased slightly for the violet part of the spectrum, ranging from a minimum of 0.028 % (10, 12 and 15 cm) to a maximum of 0.034 % (28 cm). The peak of the mean uncertainty values was reached in the blue spectral range. Mean uncertainty values of 0.037 % to 0.045 % were calculated for 15 cm (minimum) respectively 28 cm (maximum). For the remaining spectral ranges, the mean uncertainty for all the different distances to the panel decreased towards longer wavelengths. For the range from green to red, mean percentage values for a distance of 2 cm to the panel varied between 0.023 % (red) and 0.038 % (green).

Table 6: Mean *combined standard uncertainty* per wavelength range and distance to the panel in percent [%].

| <i>Wavelength range / Distance to panel [cm]</i> | <b>2</b> | <b>5</b> | <b>10</b> | <b>12</b> | <b>15</b> | <b>20</b> | <b>25</b> | <b>28</b> |
|--|----------|----------|-----------|-----------|-----------|-----------|-----------|-----------|
| <b>UV</b>  | 0,015    | 0,015    | 0,015     | 0,015     | 0,016     | 0,017     | 0,020     | 0,021     |
| <b>Violet</b>                                    | 0,032    | 0,030    | 0,028     | 0,028     | 0,028     | 0,029     | 0,032     | 0,034     |
| <b>Blue</b>                                      | 0,044    | 0,041    | 0,038     | 0,038     | 0,037     | 0,039     | 0,042     | 0,045     |
| <b>Green</b>                                     | 0,038    | 0,036    | 0,034     | 0,034     | 0,033     | 0,034     | 0,036     | 0,038     |
| <b>Yellow</b>                                    | 0,034    | 0,032    | 0,031     | 0,031     | 0,031     | 0,031     | 0,032     | 0,033     |
| <b>Orange</b>                                    | 0,030    | 0,029    | 0,028     | 0,028     | 0,028     | 0,028     | 0,028     | 0,029     |
| <b>Red</b>                                       | 0,023    | 0,022    | 0,022     | 0,022     | 0,022     | 0,022     | 0,022     | 0,022     |
| <b>NIR</b>                                       | 0,009    | 0,009    | 0,009     | 0,009     | 0,009     | 0,009     | 0,008     | 0,008     |
| <b>SWIR</b>                                      | 0,002    | 0,002    | 0,002     | 0,002     | 0,002     | 0,002     | 0,002     | 0,001     |

The values for a distance of 28 cm to the panel for the same ranges were between 0.022 % (red) and 0.038 % (green). The NIR range showed even lower mean percentages of uncertainties, where values from 0.008 % (25 and 28 cm) to 0.009 % (2 - 20 cm) were found.

The lowest mean uncertainties overall were associated with the SWIR region. The mean percentages ranged from 0.001 % for a distance of 28 cm and 0.002 % of uncertainty for all other distances to the panel. The largest mean uncertainties were found for the most extreme distances (2 and 28 cm). They were always largest for 2 cm, except for the UV, violet and blue ranges, where higher mean uncertainties occurred at a distance to the panel of 28 cm (the green wavelength range had equal values at 2 and 28 cm). The lowest mean *combined standard uncertainties* hence appeared to be associated with mid-range distances to the panel.

The consideration of the absolute *combined standard uncertainties* (in spectral radiance ( $L_\lambda$ ) [ $W/m^2srnm$ ]) was relevant to assess the magnitude of the individual uncertainties resulting from the different processing steps. It also visualised the different sources of uncertainty along the data analysis process.

Uncertainties were generated by the different input data and by the further propagation through the various processing steps. In Figure 19 the absolute uncertainties for the exemplary distance to the panel of 12 cm of the entire data analysis procedure were hence visualised. The first subplot shows the entire spectrum and all uncertainties arising from the data processing. The second and third subplot each indicate the same subset extracted from the entire spectral range to provide two enlargements to a given range for better visualisation of the different uncertainties.

In general, the uncertainties increased with every further propagation, which is well visible in Fig. 19.

The final *combined standard uncertainty* of the correction model was visualised in yellow-green ( $u_{CMinput}$ ) and provided the highest absolute values. All the initial (not yet propagated) uncertainties yielded the lowest values (except for the one uncertainty of a cross-calibration input (orange dashed line) and the interference of the  $u_{PGoffset}$  (in purple)).

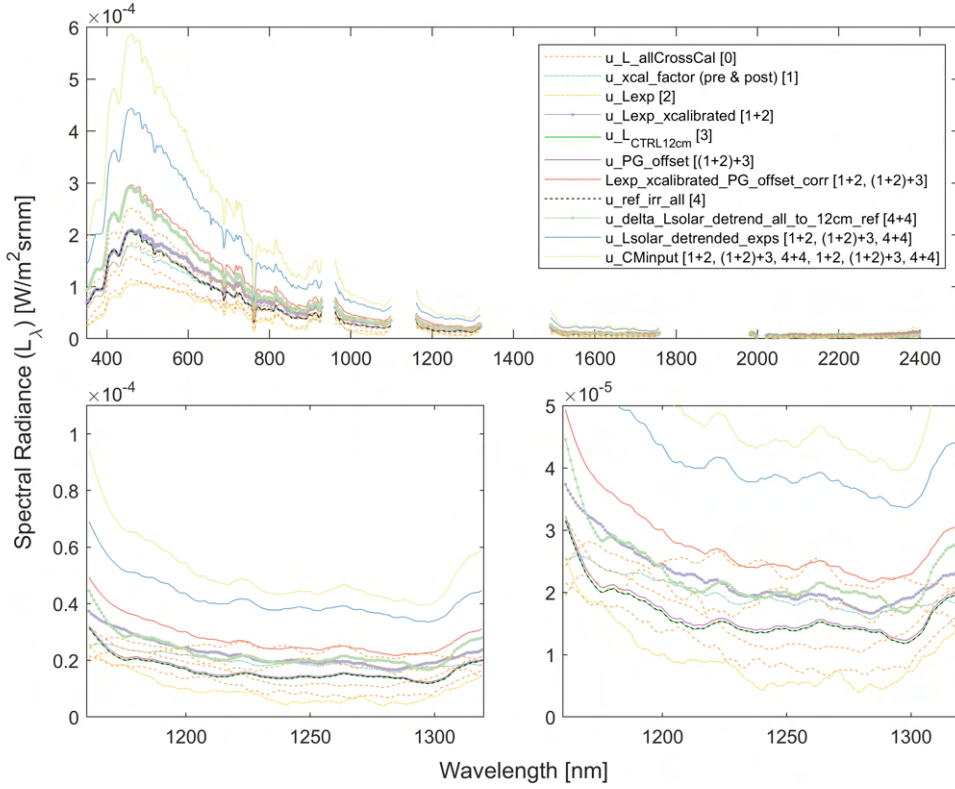


Figure 19: All statistical uncertainties of the data sets and their propagation along the data processing for a distance to the panel of 12 cm.

The non-propagated and thus purely statistical (random) uncertainties had four origins: The first resulted from the computation of the cross-calibration factor, where the individual uncertainties were calculated for each of the four cross-calibration measurements used. These uncertainties were visualised as orange dashed lines and are referred to in combination as  $u\_L\_allCrossCal$  [0]. The second uncertainty resulted from all experimental measurements ( $u\_Lexp$  [2]), the third from the reference measurement obtained at the default distance to the panel of 12 cm ( $u\_LCTRL12cm$  [3]) and the fourth resulted from the reference measurements of all distances to the panel ( $u\_ref\_irr\_all$  [4]). Thus, the latter two had very similar uncertainties.

The uncertainties of the individual cross-calibration measurements [0] were propagated into the uncertainty of the cross-calibration factor [1]. For simplicity, this propagation was not denoted as the combination of several [0] (hence, [0+0+0+0] as all the other propagated uncertainties are (see Fig. 19), but redefined as  $u\_xcal\_factor(pre&post)$  [1]. It is visible that the individual uncertainties of the cross-calibration measurements ( $u\_L\_allCrossCal$  [0]) were greater at some wavelengths than the propagated uncertainty of the cross-calibration factor ( $u\_xcal\_factor(pre&post)$  [1]). This was due to the application of the linear interpolation at the acquisition times of the experimental measurements and the for this purpose used *Monte Carlo* simulation.

The uncertainties [1] and [2] were further propagated by the multiplication of the experiments by the cross-calibration factor ( $u\_Lexp\_xcalibrated$  [1+2]).

From the calculation of the pistol grip offset, the uncertainty of the pistol grip offset ( $u\_PG\_offset$  [(1+2)+3]) and thus also the uncertainty due to the correction of the

offset ( $u_{Exp\_xcalibrated\_PG\_offset\_corr}$  [1+2, (1+2)+3]) resulted.

The necessary detrending due to the solar irradiance change over time further introduced the fourth statistical uncertainty [4], which resulted in the uncertainty of the calculated delta due to the temporal solar irradiance change ( $u_{delta\_Lsolar\_detrend\_all\_to\_12\_cm\_ref}$  [4+4]). Further, it propagated to the uncertainty of the cross-calibrated, pistol grip offset corrected and solar irradiance change detrended experimental measurements ( $u_{Lsolar\_detrended\_exps}$  [1+2, (1+2)+3, 4+4]).

The last propagation of uncertainties happened with the calculation of the correction factors as input for the *Monte Carlo* simulations ( $u_{CMinput}$  [1+2, (1+2)+3, 4+4, 1+2, (1+2)+3, 4+4]).

Comparing the magnitudes of the statistical uncertainties (uncertainties [0], [2], [3] and [4]), it can be said that the values all appeared to be in a similar range.

The uncertainty of the pistol grip offset ( $u_{PG\_offset}$ , propagated from uncertainties [1], [2] and [3]) was smaller than some of the uncertainties used to calculate the latter (e.g.,  $u_{Exp\_xcalibrated}$ ), as it was possible to reduce the uncertainty of the pistol grip offset by using the arithmetic mean for further calculations. Hence, the uncertainty was divided by the square root of the sample size.

Propagated uncertainties arising from the calculations of the cross-calibration of the experimental measurements and the pistol grip offset correction contributed only little to the overall budget.

Jumps to larger uncertainties occurred with the correction for the solar irradiance change over time (from [1+2, (1+2)+3] to [1+2, (1+2)+3, 4+4]) and with the transition from the cross-calibrated, pistol grip offset corrected and solar irradiance change detrended experiments to the correction factors used as inputs to the *Monte Carlo* simulations (from  $u_{Lsolar\_detrended\_exps}$  to  $u_{CMinput}$ ). However, these jumps were not significantly larger.

Overall, the uncertainties of the correction model remained very low compared to the initially measured spectral radiances.

### 6.3 Goodness of Fit Evaluation of the Models

An evaluation of the goodness of fit of both the correction model as well as the model of the associated *combined standard uncertainty* was performed. For this purpose, the difference (residuals) of the quadratic functions that composed the correction model and the corresponding mean *Monte Carlo* simulation values per wavelength and distance were calculated and visualised (Fig. 20). The same was done for the propagated eight uncertainty values per wavelength and all their fitted quadratic functions (Fig. 22).

As a further measure to assess the goodness of fit of the models, the *RMSE* was computed per wavelength for each of the two models (Fig. 21 and 23).

The residual plot of the correction model (Fig. 20b) showed the overall largest differences between the fitted quadratic functions and the data values in the UV and violet range (approximately from 350 - 400 nm).

An evaluation of the residuals of the eight distances to the panel of the nine defined wavelength ranges showed that for the UV and violet region, the residual values were largest at a distance to the panel of 5 cm (in relation to the other distances to the panel) (also see Fig. 29 in Appendix A). From the blue to the SWIR range, the largest residuals no longer occurred at 5 cm, but rather at a height above the panel of 10 cm.

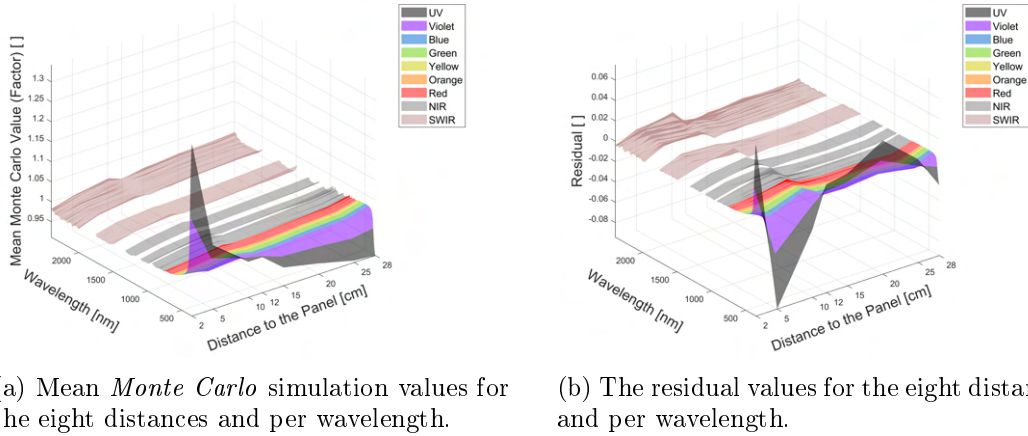


Figure 20: 3D visualisation of the mean *Monte Carlo* simulations and the corresponding residuals.

The *RMSE* of the correction model calculated per wavelength (Fig. 21) confirmed the observation from the residual plot (Fig. 20b). The *RMSE* values were largest for the range of about 350 - 400 nm. No particularly noticeable values were found for the remaining range, whereby wavelengths, at which atmospheric absorption features occur, were excluded.

The residual plot of the fitted uncertainty model functions and the actual uncertainty values (see Fig. 22) showed that the largest differences occurred in the visible range of the spectrum. The UV, NIR and SWIR regions showed smaller residuals in comparison. Fig. 32 in the Appendix A shows the residuals per wavelength range. A rather similar pattern could be observed for the entire wavelength range from UV to SWIR range with regard to the residual sizes per distance to the panel.

The largest residuals were observed at heights above the panel of 5, 25 and 28 cm, accompanied by another noticeable plateau-like peak in residuals at 12 and 15 cm for the entire spectral range. Overall, however, residual values were very small compared to the magnitudes of the factors.

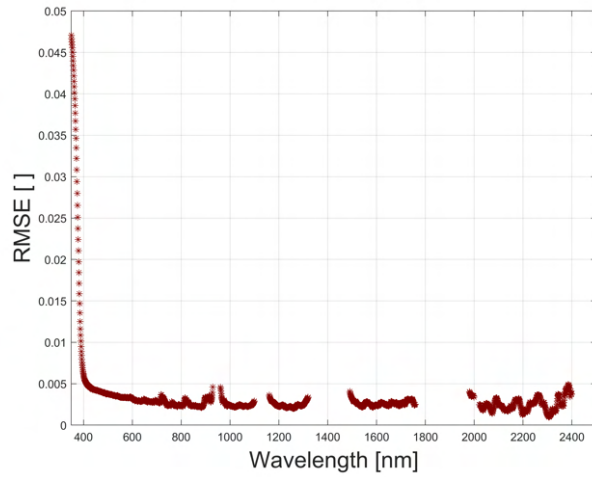
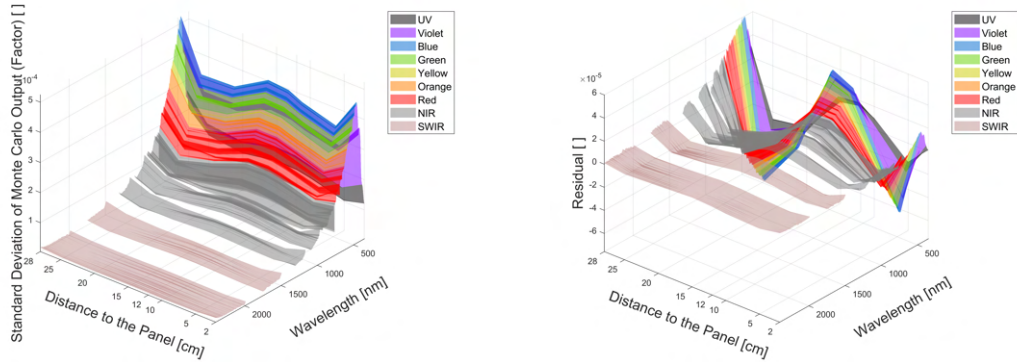


Figure 21: The  $RMSE$  of the eight distances to the panel per wavelength of the correction model.



(a) The actual values of the propagated uncertainty data for the eight distances and per wavelength.

(b) The residual values for the eight distances and per wavelength).

Figure 22: 3D visualisations of the propagated uncertainty values and the residuals.

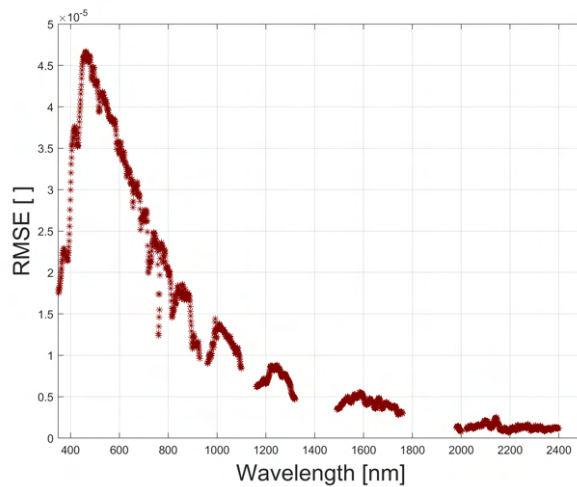


Figure 23: The  $RMSE$  of the eight distances to the panel per wavelength of the uncertainty model.



The *RMSE* of the uncertainty model per wavelength (Fig. 23) agreed with the residual plot and showed larger values for the visible range of the spectrum. Smaller *RMSE* values were found for wavelengths of the UV range and the NIR range and decreased towards the end of the spectral range of the field spectroradiometer.

## 6.4 Applied Correction Model

To demonstrate the performance of the correction model with actual data values obtained at different heights above the panel, the pre-processed (cross-calibrated, pistol grip offset corrected and solar irradiance change detrended) experimental measurements were used as input data for the application of the correction model. The mean measurement per distance and wavelength of this data set was multiplied by the corresponding correction factor. As referred to in Section 5.3.5, the uncertainty needed to be propagated once more to obtain the final *combined standard uncertainty* as well as the *expanded uncertainty* of the applied correction model.

The same exemplary wavelengths as in Fig. 16 and 17 were chosen to demonstrate the resulting distance to the panel corrected measurements (see Fig. 24 and 25). However, as these were only exemplary wavelengths, the following statements apply precisely to these described wavelengths and not to the entire range, unless otherwise mentioned.

An expected result of the correction applied to the pre-processed data was that the corrected values all had equal spectral radiances. This effect could indeed be observed in all subplots of Figures 24 and 25, especially in comparison to the uncorrected pre-processed data (blue line). The measurements at the distance of 12 cm were very similar for both data sets (pre-processed and corrected), as this height above the panel represented the chosen normalisation basis.

For the UV wavelength example, the correction appeared to have a greater effect at smaller distances to the panel than at larger distances. The uncertainty values of the applied correction model were extremely small and the *combined standard uncertainty* was hardly distinguishable from the *expanded uncertainty*.

The exemplary wavelength of the violet range showed larger corrections at the two "edge" distances to the panel (2 and 28 cm) in comparison to the other heights above the panel. All the mid-range distances to the panel (10 - 20 cm) of the pre-processed exemplary data values still lay within the envelope of the *combined standard uncertainty* or the *expanded uncertainty* of the correction model.

Exemplary wavelengths of the blue to red ranges (470, 540, 580, 610 and 670 nm) behaved rather similar. The main differences occurred at the distance of 2 cm to the panel, where the value of the pre-processed data as input data increased relatively seen the longer the wavelengths. For these ranges, the pre-processed values for distances of 10 - 15 cm all lay within the uncertainty of the correction model, with some exceptions: For the blue exemplary wavelength, the pre-processed data value of a distance to the panel of 5 cm was also within the uncertainty envelope and for the red range the heights above the panel of 10 and 15 cm were only just outside the uncertainty range. The drop in spectral radiance at the distance of 10 cm was also particularly visible in these ranges of the electromagnetic spectrum of the pre-processed data set. This was hence also reflected in the corrected data set. In addition, the correction appeared to have a bigger influence at larger distances to the panel. The remaining exemplary wavelengths of the NIR and SWIR regions (843, 1000, 1600, 1750 and 2200 nm) also behaved similarly. The influence of the correction for the different distances to the panel had more influence towards the "edge" distances. It was also noticeable that especially in these ranges, the uncertainty envelope was smaller at smaller distances to the panel (2 and 5 cm) and the uncertainty of the applied model was generally lower.

The drop at 10 cm was almost not observable within these exemplary wavelengths. The uncertainty values of the applied correction model remained rather low compared to the uncertainty of only the correction model.

Overall, both the *combined standard uncertainty* and the *expanded uncertainty* of the ap-

plied correction model were larger than the initial random noise of the instrument per distance from the panel. This was visualised in Figures 24 and 25, but is not visible by eye because the uncertainty of the instrument noise was so small.

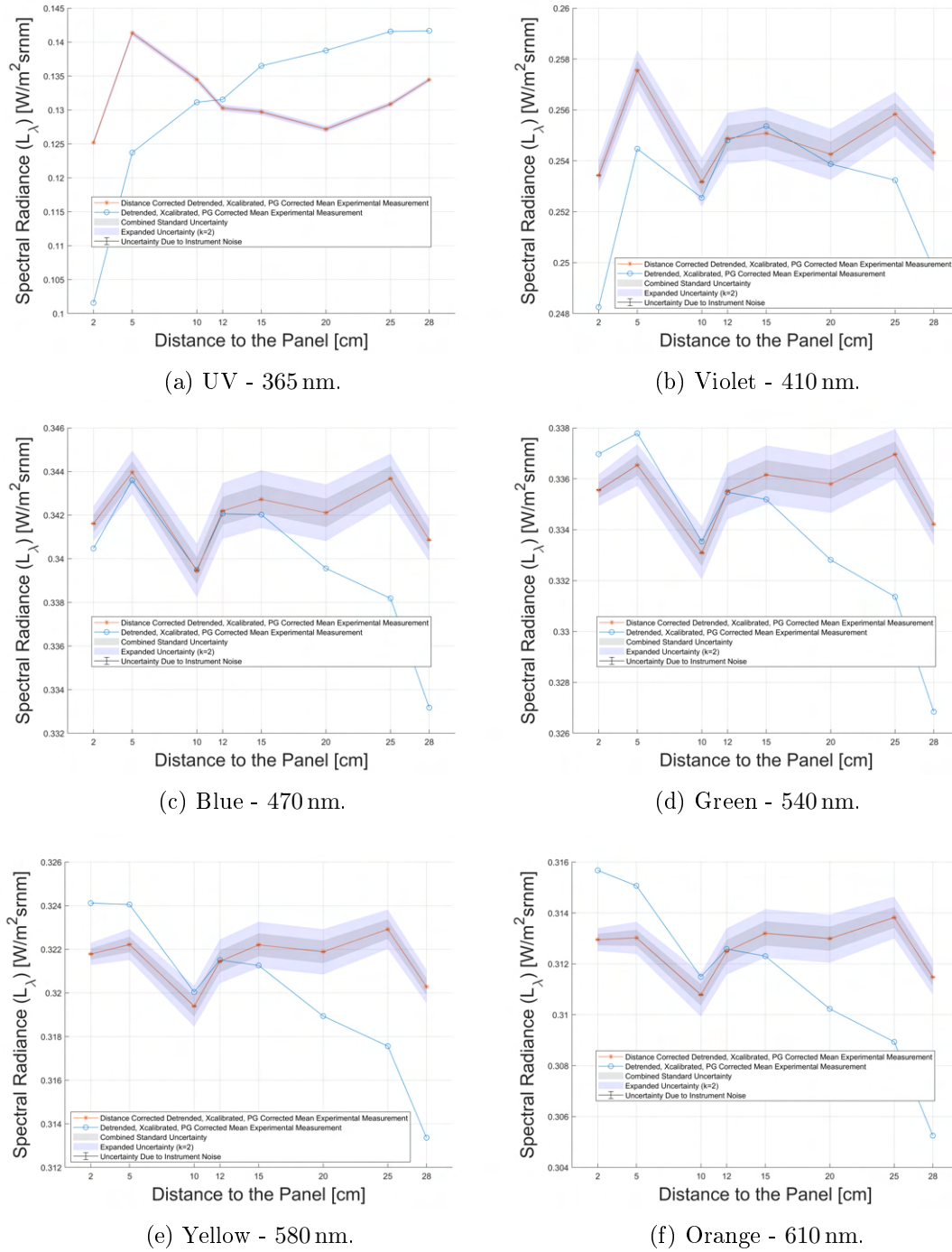
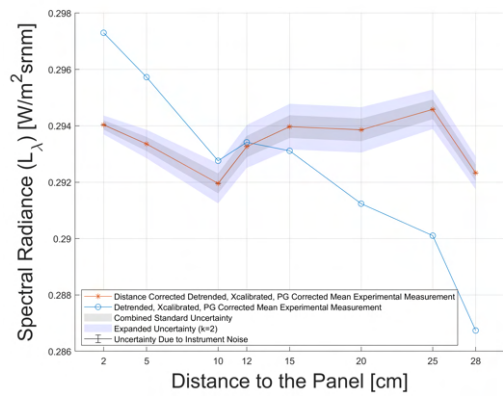
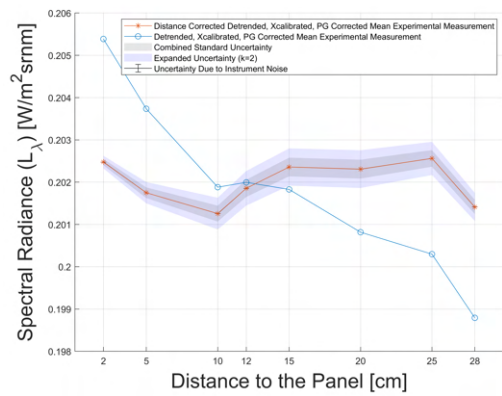


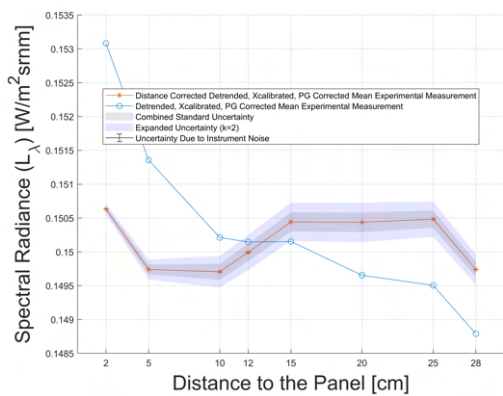
Figure 24: Exemplary applied correction model functions for distances to the panel from 2 to 28 cm and their associated uncertainties (UV - orange).



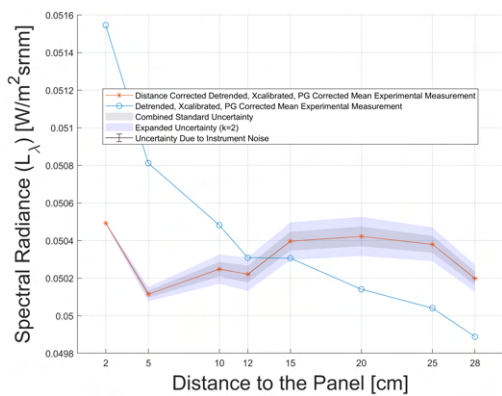
(a) Red - 670 nm.



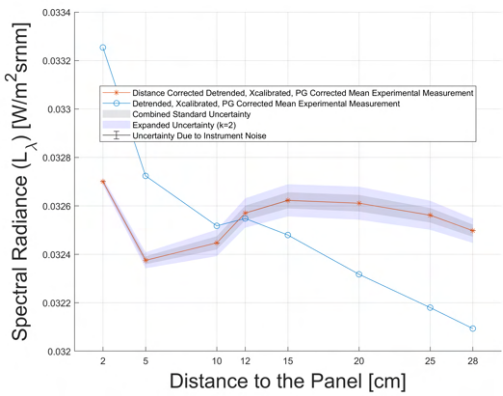
(b) NIR - 843 nm.



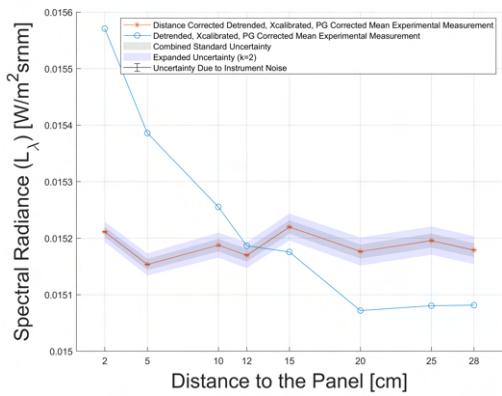
(c) NIR - 1000 nm.



(d) SWIR1 - 1600 nm.



(e) SWIR1 - 1750 nm.



(f) SWIR2 - 2200 nm.

Figure 25: Exemplary applied correction model functions for distances to the panel from 2 to 28 cm and their associated uncertainties (Red - SWIR).

## 7 Discussion

The results of the data analysis clearly show that there is a difference in the intensity of the measured spectral radiances at different distances from the fibre optic tip to the reference panel. Removing all known influencing factors and in particular the trend of the solar irradiance change over time, a pattern became visible that showed the sole influence of the different heights.

The UV and violet parts of the electromagnetic spectrum were certainly very interesting ranges of the correction model compared to the other spectral regions. The reverse shape of the correction model functions could be explained by the interaction of the solar radiation with the atmosphere and the experimental setup.

Solar radiation can be split into direct and diffuse radiation, whereas diffuse radiation is defined as radiation that is scattered by atmospheric molecules such as aerosols or dust and has no defined direction [13]. In shorter wavelength ranges, such as UV, violet and also in the blue range of the spectrum, diffuse scattering of radiation is dominated by *Rayleigh scattering*. This type of scattering occurs under most atmospheric conditions when solar radiation interacts with the Earth's atmosphere and hence its molecules [39]. It is inversely proportional to the fourth power of the wavelength and thus *Rayleigh scattering* is stronger at shorter wavelengths and less strong at longer ones [39]. Therefore, the increased diffuse radiation plays a major role at shorter wavelengths and accounts for a large proportion of the measured radiation.

As mentioned in previous sections, a pistol grip was used for the experimental setup, which served as a holder for the fibre optic cable. By correcting the difference between the pistol grip of the experimental setup and the fibre holder of the reference setup at the distance of 12 cm above the panel, the measurements at this height were thus no longer influenced by the pistol grip (but still by the presence of the fibre holder). Thus, for all distances to the panel other than the standard distance, the pistol grip still influenced the measurements by covering different fractions of the sky hemisphere (due to the different distances of the pistol grip to the reference panel surface). At a smaller distance to the panel, more of the sky hemisphere was covered by the pistol grip and, vice versa, at a greater distance, a smaller proportion. The greater influence of diffuse radiation on the measurements in shorter wavelength regions explains the inverse trend of the correction model functions in the UV and violet spectral range. At shorter distances, the measured spectral radiance values had to be increased to simulate a measurement at the default distance to the panel of 12 cm. At such small distances, less of diffuse radiation was measured at the sensor aperture due to the pistol grip covering a larger fraction of the sky hemisphere. At greater distances, however, the spectral radiances had to be decreased to match the values at the default height above the panel. In relation to the default height, too much spectral radiance reached the fibre optic tip because the pistol grip covered a smaller fraction of the sky hemisphere (see Fig. 16a and Appendix A). The pistol grip in combination with the diffuse solar radiation therefore had a large impact on shorter wavelengths (UV, violet and partly blue).

A similar effect could be observed in the study by Soffer [60] in which he investigated the influence of the operator's proximity to the reference panel. An operator standing closer to the panel resulted in reduced spectral radiance detected at the sensor aperture for the UV - VIS range of the EM-spectrum and vice versa in increased spectral radiance at longer wavelengths [60]. These findings can be compared to the influence of a pistol grip, as in both cases objects interfered with the path of the radiation to the panel and

further to the sensor. Furthermore, in both experiments, there was a need to increase rather than decrease measured spectral radiances due to interference from nearby objects in the wavelength ranges from UV to blue. Although the experimental conditions were not the same (different angular geometry of the interfering objects and other setup and environmental factors), the influence of a nearby object on the measurement could not be denied.

The UV range, as well as partly the violet range, showed another noticeable feature at greater distances of the fibre optic tip to the panel. From a distance of approximately 20 cm to the panel, a flattening of the functions towards greater distances occurred (see Fig. 26 in the Appendix A). At some wavelengths, the functions even had a tendency to increase again towards a value of one. However, this was most likely caused by the quadratic fit applied to the mean *Monte Carlo* values. As Fig. 28 in the Appendix A shows, the actual values did not increase again at larger distances to the panel for the majority of the functions, but remained constant.

This indicates that the influence of the pistol grip did not become progressively smaller at a greater distance from the panel, but remained the same from that height above the panel of approximately 25 - 28 cm (in comparison to the default height). Further, this means that the ideal distance of the fibre optic tip to the reference panel was at the distance of which the correction factors no longer decreased. The ideal normalisation basis for the UV and partly also the violet wavelength range would therefore be around 25 - 28 cm above the panel.

A normalisation basis at a distance of 28 cm would result in a maximum correction factor for a distance to the panel of 2 cm of about 1.2671, hence 26.71 % on average.

Compared to the required corrections in other wavelengths, the percentages in the UV range were especially high (see Table 5). The main difference between the short UV wavelengths and partly also the violet range and the remaining spectral ranges was the influence of diffuse radiation in combination with the pistol grip. According to [2], the diffuse radiation at shorter wavelengths contributes as much as 20 - 25 % of the total illumination reaching the panel surface in comparison to 5 - 10 % of the contribution of diffuse radiation at longer wavelengths. Hence, this effect indicated to be (at least partly) responsible for the large difference in the correction factors over the different wavelength ranges.

The correction functions of the violet range were more spread out. Fig. 26 in the Appendix A shows that the violet range was the transition zone where the change in trend occurred. Thus, the influence of diffuse radiation seemed to decrease the closer the wavelengths came to the blue spectral range. Some functions in this range had an U-shape, as shown by the exemplary wavelength in Fig. 16b. Hence, the mean percentages of corrections of the violet range presented in Table 5 need to be treated with care due to the variation of functions in this wavelength range.

For both smaller and larger distances to the panel than 12 cm, the spectral radiances at such U-shaped wavelengths barely dropped below one and had thus to be increased to get to a simulated measurement at the default distance. The reason for the necessary increase in spectral radiances at smaller heights than the default height above the panel was still the remaining effect of the larger influence of diffuse radiation at shorter wavelengths. On the other hand, at distances greater than 12 cm, the so-called *Size-of-Source Effect (SSE)* played a role.

The *SSE* describes the phenomenon that with smaller sizes of sources a reduced measured signal is received at the sensor aperture (and vice versa), while the source still fills the

projected *FOV* of the sensor [12] [61]. Yoon et al. [69] describe two factors contributing to the *SSE*: Firstly, scattering from the objective lens of the instrument and secondly, scattering that occurs within the spectroradiometer due to internal components. Due to these imperfections some radiation from outside the *FOV* is detected at the sensor aperture leading to imprecise measured values [9]. Yoon et al. [69] mention that the *SSE* should always be assessed if changes are made to the optical path from the source to the instrument [69]. The described effect also applies to the findings of this study: In the experiment, the actual size of the source did not change (the reference panel used always remained the same). However, due to the different distances of the fibre optic tip to the panel, it appeared as if one would have changed the size of source for every measurement obtained at a different distance. Measurements collected closer to the panel resulted in a smaller projected *FOV* and hence it appeared as if there was a larger size of source. Vice versa, for measurements that were further away from the panel and thus had larger projected *FOVs*, the size of source appeared smaller.

Hence, for a minority of wavelengths of the violet range closer to the blue range (e.g., Fig. 16b), the *SSE* was already visible at greater distances to the panel. This effect seemed to first dominate with increasing proximity to the blue range, followed by greater distances to the panel than the default height. Greater distances to the panel thus led to a smaller size of source and too little spectral radiance reached the sensor. Thus, the measured spectral radiance needed to be increased to reach the same values as if obtained at the default distance. At smaller distances to the panel, it seemed as if the influence of diffuse radiation in the violet range of the EM-spectrum still dominated over the *SSE*.

The same flattening as for the UV range occurred for some of the functions of the violet region that were closer to the UV range, where the same explanation can be applied.

The correction functions of the blue range completed the change in trend: The correction factors increased from smaller to larger distances to the panel. A remaining influence of diffuse radiation was still visible at the small distances to the panel (2 - 10 cm), where spectral radiances still had to be increased (due to the pistol grip influence) in order to get values similar to a measurement at 12 cm (see Fig. 26). However, the influence of the pistol grip decreased faster as the distances got closer to the default height above the panel, also in comparison to correction functions of the violet range. Wavelengths of the blue spectral range that were closer to the green spectral range tended to be less influenced by diffuse radiation at smaller distances to the panel. At such wavelengths, the influence of the *SSE* slowly prevailed and the longer the wavelengths got, the more likely the effect was visible. Greater distances to the panel than the default height needed hence to be increased in the blue range due to the *SSE*.

The green, yellow, orange, red and the first part of the NIR range appeared to have rather similar correction functions. All of these ranges were dominated by the *SSE*, which is clearly visible as distances to the panel smaller than the default height needed to be decreased in their values (due to a larger size of source and hence too much spectral radiance at the sensor aperture). Vice versa, heights above the panel greater than 12 cm needed to be increased in spectral radiance values (smaller size of source due to a larger projected *FOV*). In the green spectral range, the correction functions still spread slightly at distances of 2 - 5 cm (see Fig. 26 in the Appendix A), while this effect decreased more and more in the yellow and further ranges (change from concave shape to nearly linear). From the yellow to the SWIR range, the *SSE* dominated and the effect of diffuse radiation was eliminated.

A phenomenon that was most noticeable in these spectral ranges, but was also already visible in the blue range and even slightly in the violet as well as in the NIR range, was the small jump in values from 25 cm to 28 cm (see Appendix A, Fig. 28). An explanation for such a jump could be an edge effect, as the projected *FOV* at the distance of 28 cm came quite close to the edges of the panel. Since any matter from which spectral radiance could reach the sensor aperture was less bright than the white reference panel, this could have led to an increased correction factor at this distance. Most likely, this is also a combination of a potential edge effect and the *SSE* and therefore requires further investigation.

An additional factor leading to too much spectral radiance reaching the fibre optic tip at small distances to the panel could be inter-reflections between the sensor aperture and the reference panel surface. At small heights of the fibre optic tip above the panel, the probability of multiple reflections between the fibre optic tip and the surface of the panel is higher than at greater distances to the panel due to a shorter path length. This effect could have increased the spectral radiance at small heights above the panel, which led to a reduction of the received spectral radiance values when the correction model was applied. Most likely it was a combination of inter-reflections and the *SSE* that led to correction values smaller than one for distances smaller than the default distance in the visible wavelength range.

The same two effects of the inter-reflections and the *SSE* dominated the correction model for the NIR and SWIR range. Already slightly visible in the red range, but increasingly visible from the NIR to the SWIR region, was the change in the shape of the functions from rather linear (red) to convex (see Fig. 26 in the Appendix A). Functions of NIR wavelengths close to the SWIR range were more convex than correction functions of shorter NIR wavelengths. Hence, the longer the wavelengths, the more a flattening of the correction functions was observed. As with the very short wavelengths of the UV and partly the violet range, the flattening of the functions in the SWIR and some of the NIR wavelengths occurred again at greater distances to the panel of 20 - 28 cm. However, the literature does not mention that the *SSE* stagnates at a certain small size of source (in this case a large distance respectively a greater projected *FOV*). Since this only occurred at NIR wavelengths close to the SWIR range and SWIR wavelengths themselves, a wavelength dependence of the *SSE* was suspected. It seemed that for a certain small size of source (greater distances to the panel) the *SSE* did not further contribute to less spectral radiance being received at the sensor aperture. In this case, the effect started to stagnate at a height above the panel of 20 cm. As mentioned previously, this only occurred for the longer wavelength ranges of the spectroradiometer's electromagnetic spectrum (partly NIR and SWIR). Furthermore, this phenomenon of a flattening function could only be observed for the case where sizes of sources decreased continuously. For the opposite case (at smaller distances to the panel), no flattening was observed at NIR or SWIR wavelengths. One reason for this could be that the *SSE* at smaller distances to the panel is dominated by the effect of inter-reflections and therefore no flattening of the functions occurred.

Overall, the correction factors that needed to be applied to correct for the different distances of the fibre optic tip to the panel were rather small. The majority of the deviations varied up to a mean maximum of 2.94% for all the different distances and over the entire wavelength range except for the UV range. The UV range was strongly influenced by diffuse radiation, therefore the correction factors were larger compared to the rest of the spectroradiometer's EM-spectrum. All in all, the percentages seem to be reasonable considering the influences of diffuse radiation, the inter-reflections and the *SSE*.



A correction model is only as good as its fit to the data. Relatively speaking, the model fitted worst in the UV and violet range, as shown in the residual plot as well as in the *RMSE* (Fig. 20 and 21). According to the residual plots per wavelength range (see Appendix A, Fig. 29), the residuals for the UV and violet range were highest at a distance to the panel of 5 cm. The reason why the fit was poorer at this distance could be the greater influence of diffuse radiation at the even smaller distance to the panel of 2 cm. Therefore, a quadratic function did not best fit the correction factor at a distance of 5 cm.

Furthermore, the quadratic fit gave the impression that the correction factors increased at greater distances to the panel (from 20 cm) for the UV and partly the violet range (see Fig. 26 in the Appendix A). However, when comparing the quadratic fits with the mean *Monte Carlo* correction factors at these same distances, it was clear that the input values for the quadratic fit did not increase towards one, but rather stagnated for the majority of the functions. Hence, the fit did not optimally represent the actual values at these distances to the panel.

For all other wavelength ranges, the highest residual was found at a distance of 10 cm. In Fig. 28 of the Appendix A as well as in the Figures 16 and 17, it is shown that for different wavelengths, different effects occurred at a distance of 10 cm to the panel. For the shorter blue wavelength range, it appeared that the mean *Monte Carlo* correction factor at a height of 10 cm above the panel was an outlier compared to the other values. However, for wavelengths from approximately the green to the NIR range, it appeared that the mean *Monte Carlo* correction factors formed a plateau at distances to the panel of 10 - 15 cm. Hence, it could be debated (and needs to be tested in further studies) that an S-shaped function could represent the mean *Monte Carlo* correction factors better than a quadratic function. On the other hand, the experiment should be repeated to exclude the possibility that the measurement at the distance to the panel of 10 cm was an outlier. The reason for this potential plateau effect could be the similar sizes of projected *FOVs* for distances to the panel of 10 - 15 cm and their relation to the size of the reference panel. The size of the reference panel at these three distances may not affect the same three distances as differently compared to smaller or larger distances to the panel. Hence, all the previously mentioned influences should be inherently more similar for these three heights above the panel.

Overall, the quadratic fits seem to have performed adequately and provided a reasonable correction model.

The modelled *combined standard uncertainties* of the correction model were pleasingly small compared to the initially measured spectral radiances. The uncertainties were largest in the blue wavelength range and smallest in the SWIR range. From Fig. 19 it can be taken that the uncertainty in the blue spectral range was already highest for the purely statistical uncertainties compared to the other ranges of the electromagnetic spectrum of the spectroradiometer. Hence, a propagation of uncertainties inevitably led to further increased uncertainty values in this range. The reasons for the higher uncertainty in the blue spectral range could most likely be the higher sensitivity to stray light, the relatively lowest *Signal-to-Noise-Ratio* and the greatest sensitivity to wavelength errors (personal communication with Emma Woolliams, *National Physical Laboratory*).

In general, the *combined standard uncertainties* were higher at smaller and greater distances to the panel than at the medium distances (see Fig. 30 in Appendix A). This was given due to the fit of the quadratic functions to the uncertainties of the eight initial values.

The quadratic functions fitted to the *combined standard uncertainty* of the eight initial distances to the panel provided an overall reasonable application in terms of shape. However, due to the nature of the fit, the uncertainty was underestimated for some distances to the panel, but also overestimated for some others (see Fig. 22). For heights above the panel of 2 and 28 cm, the *combined standard uncertainty* was underestimated, as well as for distances of 12 and 15 cm, which should be remembered (see Fig. 22 and Fig. 32). These effects were largest in the visible range of the electromagnetic spectrum, as shown in Fig. 23. Hence, the fit only provided an approximation of the uncertainty.

On the one hand, the generally low uncertainty values had to do with the low random (statistical) uncertainties of the input data sets (see Fig. 19). On the other hand, as already mentioned, it must be considered that all calculated uncertainties were underestimated due to omitting the calculation of the estimated covariance as well as due to a possible variety of unknown uncertainties.

All in all, the correction model applied to the pre-processed data performed as expected: Spectral radiance values were all corrected to a similar value and the associated uncertainties of the correction model were small to moderate and did not diminish the added value of the correction for most distances to the panel.

The smaller overall uncertainties for the exemplary wavelengths, especially in the UV but also in the SWIR range, were noticeable but logical considering the uncertainties of the correction model (see Fig. 18).

The most important fact that can be taken from the exemplary Figures 24 and 25 was that the application of the correction model to the majority of the distances to the panel actually added value. The uncertainty of the corrected values was not that large for most heights above the panel that it included the uncorrected values. For medium distances (10 - 15 cm) the added value of the correction model could be debated (but this is also due to the choice of the normalisation basis at 12 cm above the panel), but for very small and very great distances to the panel the added value was evident in the context of the used normalisation basis. This applied to the entire spectral range of the field spectroradiometer.

Again, the almost consistent drop in absolute spectral radiance for the visible range of the electromagnetic spectrum is noteworthy (see Fig. 24 and 25). As mentioned previously, this was either due to an outlier in the measurement series or due to the poor fit of the quadratic function. However, the former can be verified by repeating the experiment and the latter by fitting the proposed S-shaped function to the data values.

Also noteworthy is the sudden smaller uncertainty at the distance to the panel of 2 cm (sometimes also at 5 cm), especially at longer wavelengths. This effect originated from the propagated uncertainty in the application of the model and could be attributed to the uncertainty of the pre-processed data, since the uncertainty of the correction model (see e.g., Fig. 16 or 17) did not indicate a smaller uncertainty at the height of 2 cm above the panel.

## 8 Conclusion

This study aimed at contributing to the topic of operator- and setup-related uncertainties in field spectroscopy. In-situ spectroradiometric measurements are influenced by several methodological aspects introduced by the operator and the handling of the material. The distance of the fibre optic tip (sensor aperture) to the white reference panel is one of those aspects that affect the measured spectral radiance.

The following research questions and hypotheses were posed at the beginning of this thesis and are now answered:

- *Is there a difference in measured spectral radiances at different distances of the fibre optic tip (sensor aperture) to the surface of the white reference panel, given that the projected FOV of the sensor is still on the panel?*

Yes, there are differences in spectral radiance values between measurements conducted at a height of 2 cm above the panel or at any other height up to 28 cm. A correction model was calculated to correct for these differences. The definition of a normalisation basis to which every measured data set is corrected enables the comparison of ground measurements acquired at different distances to the panel and puts them into context. This ability to make data comparable is important for the further use of field spectroscopy measurements in calibration or validation processes of other, e.g., airborne or satellite-based measurements.

Thus, the hypotheses can be accepted or rejected:

$H_0$ : *Several measurements performed using the same setup, but with the fibre optic tip at different heights above the panel, will lead to the same spectral radiance intensities, given that the projected FOV of the sensor is still on the panel.*

$H_1$ : *Several measurements performed using the same setup, but with the fibre optic tip at different heights above the panel, will lead to different spectral radiance intensities, given that the projected FOV of the sensor is still on the panel.*

$H_0$  is rejected and  $H_1$  accepted.

- *If there are differences, how large are they compared to the predefined default height of 12 cm (relatively)?*

The extent of the differences due to the different heights above the panel and hence the applied correction is wavelength dependent. The UV range (and partly also the violet range) required a significantly larger correction than the other spectral ranges of the field spectroradiometer. The diffuse radiation (in combination with the pistol grip) had a relatively greater influence in the short wavelengths compared to the influences (*SSE*, inter-reflections and potentially edge effects) that dominated the visible to SWIR range. Therefore, the impact of the distance of the fibre optic tip to the panel is of greater importance in shorter wavelength ranges. In the visible to SWIR range there were still differences and corrections had to be applied, but these were significantly smaller.

Thus, the hypotheses can be accepted or rejected:

$H_0$ : *At greater distances from the fibre optic tip to the panel, the measured spectral radiance shows the same values compared to a default height of 12 cm as at smaller distances to the panel, given that the projected FOV of the sensor is still on the panel.*

$H_1$ : *At greater distances from the fibre optic tip to the panel, the measured spectral radiance shows higher values compared to a default height of 12 cm as at smaller distances to the panel, given that the projected FOV of the sensor is still on the panel.*

$H_0$  is rejected and  $H_1$  is accepted for the UV and partly the violet range of the EM-spectrum.

$H_0$ : *At smaller distances from the fibre optic tip to the panel, the measured spectral radiance shows the same values compared to a default height of 12 cm as at greater distances to the panel, given that the projected FOV of the sensor is still on the panel.*

$H_1$ : *At smaller distances from the fibre optic tip to the panel, the measured spectral radiance shows smaller values compared to a default height of 12 cm as at greater distances to the panel, given that the projected FOV of the sensor is still on the panel.*

$H_0$  is rejected and  $H_1$  is accepted for the UV and partly the violet range of the EM-spectrum.

The posed hypotheses apply to the UV and partly the violet range of the EM-spectrum, but not to the remaining spectral ranges due to the previously mentioned different influences in these wavelength regions.

- *If there are differences, would the application of a correction model, which corrects measurements acquired at different heights to the default height, add value, or would the associated uncertainty of the correction model still be greater?*

In most of the cases, a correction model added value to the acquired data sets. Both the *combined standard uncertainty* and the *expanded uncertainty* of the correction model applied to the selected measurements were reasonably small and the majority of the uncorrected values did not fall within the uncertainty range of the corrected data. The *combined standard uncertainty* of the applied correction was still greater than the pure statistical noise of the instrument, which was expected. Overall, the application of the model improved the measured values.

Thus, the hypotheses can be accepted or rejected:

$H_0$ : *The uncertainty of a correction model that corrects different distances to the panel to a default distance of 12 cm is smaller than the noise of the instrument.*

$H_1$ : *The uncertainty of a correction model that corrects different distances to the panel to a default distance of 12 cm is greater than the noise of the instrument.*

$H_0$  is rejected and  $H_1$  accepted.

The following section contains a summary of the most important findings that can be concluded from this work:

A clear wavelength dependence was apparent for measurements acquired at different heights above the panel. Shorter wavelength ranges were more influenced by diffuse radiation, while longer wavelength ranges were dominated by the *SSE*, and at shorter distances to the panel also by inter-reflections. Edge effects potentially influenced measurements of the visible to NIR spectral ranges at a distance of 28 cm, due to a projected *FOV* that came very close to the panel edges.

For wavelengths of the UV, partly the violet range as well as the longer NIR wavelengths and the entire SWIR range, it seemed that the ideal normalisation basis was not perfectly chosen. At greater distances to the panel, the influence of diffuse radiation in combination with the pistol grip for UV and violet and the influence of the *SSE* for the NIR and SWIR range seemed to have been attenuated. Hence, for these wavelength ranges, it appears that a normalisation basis at greater distances to the panel (25 - 28 cm) would more closely represent the true value of the measured spectral radiance.

The correction model factors and also the *combined standard uncertainties* of the correction model were rather small. The highest uncertainty values were found in the blue range of the electromagnetic spectrum and the lowest uncertainties were found in the SWIR range.

The fitted functions defining both the correction model and the uncertainty model seemed to give a reasonable result. However, it should be investigated if an S-shaped function could further improve the results for some of the wavelengths in the correction model.

Overall, this study delivered a first approach to quantifying one of several seemingly small aspects of field spectroscopy measurements and revealed their potential as sources of uncertainty. The impact of aspects of data acquisition that operators are often not even aware of is too great to ignore. The obtained results visualise the importance of creating awareness on the topic and the need to provide quantified and traceable uncertainty of such measurements. The reliability of any target data set depends on the certainty of its measurements.

To the best of our knowledge, the effect of different distances of the fibre optic tip to the reference panel and its influence on the measured spectral radiances has not yet been described in the literature. The calculated correction model and its associated *combined standard uncertainty* can be applied to obtained data sets in order to standardise acquired in-situ spectroradiometric measurements. However, the applied uncertainties still have to be treated with caution, as they are most likely an underestimation of the associated uncertainties due to the imperfect fit of the function to the data values, the omission of the covariance matrices and the unknown uncertainties (e.g., the additional introduced uncertainty due to the broken fibres).

Also, as mentioned in Section 1.3, uncertainty calculations can be performed almost to infinity due to the large number of influencing factors. Unfortunately, it is rarely possible to quantify all influencing factors and hence the uncertainty of a targeted measurand in its entirety. A perfect holistic and not under- or overestimated uncertainty budget requires large amounts of time, computational and knowledge resources, which are rarely all accessible together.

## 9 Outlook

To further advance the topic of uncertainties in field spectroscopy measurements, the comprehensive aim would be to establish a complete uncertainty budget and provide correction models where necessary. Also, a standardised field protocol for the acquisition of spectroradiometric ground measurements would benefit the cause and the community.

To achieve this, all parameters that influence the in-situ measurements must be isolated and analysed for their effect on the measurements. Thus, more experiments have to be conducted and potential correction models with associated uncertainties have to be developed.

Operator awareness of the supposed simplicity of spectroradiometric data acquisition also needs to be created. Due to the deceptively simple character of the measurements, too many (unintentional) errors happen in the field that could be avoided.

In the specific case of estimating the influence of the distance of the fibre optic tip to the surface of the white reference panel, the following improvements can be made in further studies:

First of all, the study was only conducted once. Therefore, a significant number of repetitions would increase the validity of the study and confirm the results. Furthermore, a repetition of the experiment would also provide clarity on the phenomena that occurred at the distance of 10 cm to the panel (outlier or plateau-effect). Consideration may also be given to repeating the study using a fore optic with a narrower *FOV*. This could reveal different effects than those observed in this study and could possibly have an influence on the *SSE*. A higher number of reference measurements would also be beneficial for the experiment. This would lead to a more precise evaluation of the fluctuations of the solar irradiance over time and hence lead to a more accurate detrending of the experimental data set. The use of a larger reference panel should also be considered to further investigate the effect of greater distances than 28 cm to the panel and to find the ideal normalisation basis. Intact and reliable instruments (e.g., no broken fibres) would also benefit the study to have less uncertainty in the data. In the manual of the *ASD FieldSpec 3* [2], e.g., it states that for each broken fibre, a loss of signal of approximately 5% has to be taken into account.

For data analysis, it may be considered to use a function that can be fitted more precisely to the data. An S-shaped function should be applied if repeated experiments present the same results as obtained in this study (indicating a plateau for some wavelength ranges). The estimation of the *combined standard uncertainty* of the correction model would be improved by calculating the estimated covariances of the input variables, but also by quantifying further uncertainties unknown up to this point ( $u(0)$ ).

In a more general and forward-looking context, the topic would benefit from several implementations:

With the further exploration of larger distances to the panel and also the confirmation of a potential normalisation basis for some wavelength ranges, the correction factor could also become applicable to airborne or space-based sensors. Sensors at greater distances from the Earth's surface are also impacted to some extent (in some wavelength ranges more than in others) by the effects observed in this study. With an extrapolation of the correction factors to such large distances, they can be added to the uncertainty budget of airborne and space-based sensors. However, the results of this study should first be further validated by repeating the experiment to gain more certainty about the findings.

The extent of the influence of diffuse and direct radiation as a function of wavelength and distance to the reference panel should also be subject of further research. More knowledge about the relationship of radiation and the distance of the sensor aperture to a target matter is created by differentiating dominant radiation influences more precisely. This can be done, for example, by implementing a physical model in which functions representing diffuse and direct radiation can be fitted to the spectral radiance measured at different distances. This then provides the percentages of the individual influences of the different radiation components.

Uncertainty in field spectroscopy is a topic that should generally receive more attention. Many aspects have not yet been analysed in detail, although they are of great importance for any further product based on field spectroscopy measurements. Further research on this topic would benefit the entire community working with optical remote sensing data.

## Acknowledgements

In the course of writing my Master's thesis, I was able to count on the support of numerous people. First of all, many thanks to my supervisor Andy, who always had an open ear and took the time for countless team meetings even in stressful times. He always came up with clever ideas, has great guidance skills and never lost interest in the topic. I learnt a lot!

Secondly, thanks to all the people whose advice I sought from time to time; that is Nikola, who helped me solve numerous logical and mathematical problems when it came to the calculation of the model and also validated my ideas; Marius, Dario, Joan and Simon for relevant inputs and feedback at certain points in the process. And once more Nikola, Mike and Marius, who volunteered to read the whole (!) thesis and give feedback! What an effort, thanks a lot!

Last but not least, I would also like to thank Emma Woolliams and Chris MacLellan from NPL who sacrificed their lunch break to talk to us about spectroradiometers and uncertainties and provided very relevant inputs.

Many thanks to all of you!



## References

- [1] RS 3™ User Manual. Technical report, Analytical Spectral Devices, Inc. a Malvern PANalytical company, 2008.
- [2] FieldSpec 3 User Manual. Technical report, Analytical Spectral Devices, Inc. a Malvern PANalytical company, 2010.
- [3] FieldSpec 4 User Manual. Technical report, Analytical Spectral Devices, Inc. a Malvern PANalytical company, 2016.
- [4] Field spectroscopy guide with SVC i-series spectroradiometers. Technical report, Spectra Vista Corporation (SVC), 2019.
- [5] A. Agapiou, D. G. Hadjimitsis, D. D. Alexakis, and G. Papadavid. Examining the phenological cycle of barley (*Hordeum vulgare*) using satellite and in situ spectroradiometer measurements for the detection of buried archaeological remains. *GIScience and Remote Sensing*, 49(6):854–872, 2012.
- [6] D. G. Altman and J. M. Bland. Standard deviations and standard errors. *BMJ: British Medical Journal*, 331(7521):903, 2005.
- [7] K. Anderson and E. J. Milton. On the temporal stability of ground calibration targets: Implications for the reproducibility of remote sensing methodologies. *International Journal of Remote Sensing*, 27(16):3365–3374, 2006.
- [8] D. W. Ball. *Field guide to spectroscopy*, volume 08. Spie Press, Bellingham, Washington, 2006.
- [9] M. Bart, E. W. Van Der Ham, and P. Saunders. A new method to determine the size-of-source effect. *International Journal of Thermophysics*, 28(6):2111–2117, 2007.
- [10] D. Beal and M. Eamon. Preliminary results of testing and a proposal for radiometric error correction using dynamic, parabolic linear transformations of “Stepped” Data (PCORRECT.EXE). *Analytical Spectral Devices, Inc*, 2009.
- [11] S. Bell. Good practice guide no. 11 - The beginner’s guide to uncertainty of measurement. *National Physical Laboratory*, (2):1–34, 2001.
- [12] A. Białek, T. Goodman, E. Woolliams, J. F. Brachmann, T. Schwarzmaier, J. Kuusk, I. Ansko, V. Vabson, I. C. Lau, C. MacLellan, S. Marty, M. Ondrusek, W. Servantes, S. Taylor, R. V. Dommelen, A. Barnard, V. Vellucci, A. C. Banks, N. Fox, R. Vendt, C. Donlon, and T. Casal. Results from verification of reference irradiance and radiance sources laboratory calibration experiment campaign. *Remote Sensing*, 12(14):2220.1–18, 2020.
- [13] J. Bilbao, R. Román, C. Yousif, A. Pérez-Burgos, and M. A. De. Global, diffuse, direct, and ultraviolet solar irradiance recorded in Malta and atmospheric component influences. *Energy Procedia*, 57:1206–1210, 2014.
- [14] A. Burkart, S. Cogliati, A. Schickling, and U. Rascher. A novel UAV-based ultra-light weight spectrometer for field spectroscopy. *IEEE Sensors Journal*, 14(1):62–67, 2014.
- [15] B. Curtiss and A. Goetz. Field spectrometry: Techniques and instrumentation. In *International Symposium on Spectral Sensing Research*, pages 31–40, 1994.

- [16] A. J. Deadman, I. D. Behnert, N. P. Fox, and D. Griffith. Laboratory panel and radiometer calibration. In *2011 IEEE International Geoscience and Remote Sensing Symposium*, pages 3883–3886, 2011.
- [17] K. Elmer, R. J. Soffer, J. Pablo Arroyo-Mora, and M. Kalacska. ASDToolkit: A novel MATLAB processing toolbox for ASD field spectroscopy data. *Data*, 5(4):96, 2020.
- [18] Gamma Play. Bubble Level (Android Application), 2015.
- [19] A. F. H. Goetz. Making accurate field spectral reflectance measurements. *ASD Inc. a PANalytical company*, (October):16, 2012.
- [20] Group on Earth Observations (GEO) / Committee on Earth Observation Satellites (CEOS). A quality assurance framework for earth observation: Operational guidelines. Technical report, 2009.
- [21] D. Haboudane, J. Miller, N. Tremblay, E. Pattey, and P. Vigneault. Estimation of leaf area index using ground spectral measurements over agriculture crops: Prediction capability assessment of optical indices. In *XXth ISPRS Congress: "Geo-Imagery Bridging Continents"*, pages 12–23, Istanbul, Turkey, 2004.
- [22] D. C. Hatchell. ASD technical guide. *Analytical Spectral Devices, Inc. (ASD)*, (4th Ed.):144, 1999.
- [23] T. H. Hemmer and T. L. Westphal. Lessons learned in the postprocessing of field spectroradiometric data covering the 0.4-2.5- $\mu\text{m}$  wavelength region. *Algorithms for Multispectral, Hyperspectral, and Ultraspectral Imagery VI, International Society for Optics and Photonics*, 4049:249–260, 2000.
- [24] T. Hoffmann. SunCalc - [suncalc.org](http://suncalc.org), 2015.
- [25] R. Hollmann, C. J. Merchant, R. Saunders, C. Downy, M. Buchwitz, A. Cazenave, E. Chuvieco, P. Defourny, G. De Leeuw, R. Forsberg, T. Holzer-Popp, F. Paul, S. Sandven, S. Sathyendranath, M. Van Roozendaal, and W. Wagner. The ESA climate change initiative: Satellite data records for essential climate variables. *Bulletin of the American Meteorological Society*, 94(10):1541–1552, 2013.
- [26] A. Hueni and A. Bialek. Cause, effect, and correction of field spectroradiometer interchannel radiometric steps. *IEEE Journal of Selected Topics in Applied Earth Observations and Remote Sensing*, 10(4):1542–1551, 2017.
- [27] A. Hueni, A. Damm, M. Kneubuehler, D. Schlapfer, and M. E. Schaepman. Field and airborne spectroscopy cross validation - Some considerations. *IEEE Journal of Selected Topics in Applied Earth Observations and Remote Sensing*, 10(3):1117–1135, 2017.
- [28] Joint Committee for Guides in Metrology. Evaluation of measurement data — Guide to the expression of uncertainty in measurement. 100(September):120, 2008.
- [29] Joint Committee for Guides in Metrology. Evaluation of measurement data — Supplement 1 to the “Guide to the expression of uncertainty in measurement” — Propagation of distributions using a Monte Carlo method. 101:82, 2008.
- [30] D. S. Kimes, J. A. Kirchner, and W. W. Newcomb. Spectral radiance errors in remote sensing ground studies due to nearby objects. *Applied Optics*, 22(1):8–10, jan 1983.

- [31] L. Kooistra, J. Wanders, G. F. Epema, R. S. Leuven, R. Wehrens, and L. M. Buydens. The potential of field spectroscopy for the assessment of sediment properties in river floodplains. *Analytica Chimica Acta*, 484(2):189–200, 2003.
- [32] G. Kopp. Magnitudes and timescales of total solar irradiance variability. *Journal of Space Weather and Space Climate*, 6(A30):11, 2016.
- [33] S. J. Koppal. Lambertian reflectance. In K. Ikeuchi, editor, *Computer Vision*, pages 441–443. Springer, Boston, MA, 2014.
- [34] M. Kuester, K. Thome, K. Krause, K. Canham, and E. Whittington. Comparison of surface reflectance measurements from three ASD FieldSpec FR spectroradiometers and one ASD FieldSpec VNIR spectroradiometer. In *IEEE 2001 International Geoscience and Remote Sensing Symposium (IGARSS)*, volume 1, pages 72–74, 2001.
- [35] Labsphere Inc. Technical guide - Reflectance materials and coatings. Technical report, 2011.
- [36] Labsphere Inc. HELIOS uniform source systems hardware reference guide - Manual number AQ-31000-000\_Revision\_03. Technical report, 2017.
- [37] Labsphere Inc. Ground, aerial, vacuum and space systems capabilities (Brochure). Technical report, 2018.
- [38] Labsphere Inc. Spectralon reflectance material care and handling guidelines. Technical report, 2019.
- [39] T. Lillesand, R. W. Kiefer, and J. Chipman. *Remote sensing and image interpretation*. John Wiley & Sons, 7th edition, 2015.
- [40] L. Ma, Y. Zhao, E. R. Woolliams, C. Dai, N. Wang, Y. Liu, L. Li, X. Wang, C. Gao, C. Li, and L. Tang. Uncertainty analysis for RadCalNet instrumented test sites using the Baotou sites BTCN and BSCN as examples. *Remote Sensing*, 12(11):1696–1726, 2020.
- [41] A. Mac Arthur. Field guide for the ASD FieldSpec Pro - Raw DN mode. *Field Spectroscopy Facility, Natural Environmental Research Council*, 2(November):1–7, 2007.
- [42] A. Mac Arthur, C. J. MacLellan, and T. Malthus. The fields of view and directional response functions of two field spectroradiometers. *IEEE Transactions on Geoscience and Remote Sensing*, 50(10):3892–3907, 2012.
- [43] A. Mac Arthur and I. Robinson. A critique of field spectroscopy and the challenges and opportunities it presents for remote sensing for agriculture, ecosystems, and hydrology. *Remote Sensing for Agriculture, Ecosystems, and Hydrology XVII*, 9637(October):963705–1–11, 2015.
- [44] T. Malthus, C. Ong, I. Lau, P. Fearn, G. Byrne, M. Thankappan, L. Chisholm, L. Suarez, K. Clarke, P. Scarth, and S. Phinn. *A community approach to the standardised validation of surface reflectance data. A technical handbook to support the collection of field reflectance data*. Number 2.0. CSIRO, Australia, 2019.
- [45] MeteoSchweiz - Bundesamt für Meteorologie und Klimatologie. CLIMAP-net, 2020.
- [46] E. J. Milton. Field spectroscopy. *Geoinformatics, Encyclopaedia of Life Support Systems (EOLSS)*. Oxford, UK: EOLSS Publishers, pages 1–28, 2004.

- [47] E. J. Milton, M. E. Schaepman, K. Anderson, M. Kneubühler, and N. Fox. Progress in field spectroscopy. *Remote Sensing of Environment*, 113(0034-4257):92–109, 2009.
- [48] National Physical Laboratory (NPL). TRUTHS - Traceable Radiometry Underpinning Terrestrial- and Helio- Studies, 2021.
- [49] F. E. Nicodemus, J. C. Richmond, J. J. Hsia, I. W. Ginsberg, and T. Limperis. Geometrical considerations and nomenclature for reflectance. *National Bureau of Standards, US Department of Commerce, Washington D.C.*, (October):1–52, 1977.
- [50] R. Pachauri, M. Allen, V. Barros, J. Broome, W. Cramer, R. Christ, J. Church, L. Clarke, Q. Dahe, and P. Dasgupta. Climate change 2014: Synthesis report summary chapter for policymakers. Technical report, IPCC, Geneva, Switzerland, 2014.
- [51] J. M. Palmer and B. G. Grant. *The art of radiometry*. Society of Photo-Optical Instrumentation Engineers (SPIE), 2009.
- [52] S. Phinn, P. Scarth, T. Gill, C. Roelfsema, and M. Stanford. Field spectrometer & radiometer guide. Version 7(May):1–37, 2007.
- [53] A. Pimstein, A. Karnieli, and D. J. Bonfil. Wheat and maize monitoring based on ground spectral measurements and multivariate data analysis. *Journal of Applied Remote Sensing*, 1(013530):1–16, 2007.
- [54] plaincode app development + tech blog. Clinometer (Android Application), 2010.
- [55] E. M. Rollin, D. R. Emery, and E. J. Milton. Reference panel anisotropy and diffuse radiation - Some implications for field spectroscopy. *International Journal of Remote Sensing*, 21(15):2799–2810, 2000.
- [56] R. Routledge. Central limit theorem, 2020.
- [57] G. Schaepman-Strub, M. E. Schaepman, T. H. Painter, S. Dangel, and J. V. Martonchik. Reflectance quantities in optical remote sensing - Definitions and case studies. *Remote Sensing of Environment*, 103(1):27–42, 2006.
- [58] M. Seeley and G. P. Asner. Imaging spectroscopy for conservation applications. *Remote Sensing*, 13(2):292–308, 2021.
- [59] F. Seidel, J. Nieke, D. Schläpfer, R. Höller, W. von Hoyningen-Huene, and K. Itten. Aerosol retrieval for APEX airborne imaging spectrometer: A preliminary analysis. In *Remote Sensing of Clouds and the Atmosphere X*, volume Proc. SPIE, pages 1–10, 2005.
- [60] R. Soffer. Contamination of ground spectral measurements due to operator proximity. In *IGARSS 2014 / 35th Canadian Symposium on Remote Sensing*, pages 1–4, Quebec, Canada, 2014.
- [61] J. C. Solorio-Leyva, J. G. Suarez-Romero, J. B. Hurtado-Ramos, E. Tepichin Rodriguez, and J.-G. R. Cortes-Reynoso. The size-of-source effect in practical measurements of radiance. In *5th Iberoamerican Meeting on Optics and 8th Latin American Meeting on Optics, Lasers and Their Application*, volume Proc. SPIE, pages 1243–1248, 2004.
- [62] S. Sterckx, I. Brown, A. Kääb, M. Krol, R. Morrow, P. Veeffkind, K. F. Boersma, M. De Mazière, N. Fox, and P. Thorne. Towards a European Cal/Val service for earth observation. *International Journal of Remote Sensing*, 41(12):4496–4511, 2020.

- [63] B. N. Taylor and C. E. Kuyatt. Guidelines for evaluating and expressing the uncertainty of NIST measurement results - 1994 edition. Technical report, 1994.
- [64] The MathWorks Inc. MATLAB, 2020.
- [65] United Kingdom Accreditation Service (UKAS). M3003 the expression of uncertainty and confidence in measurement. Technical Report October, 2019.
- [66] A. J. Walsh, G. Byrne, and M. Broomhall. A case study of measurement uncertainty in field spectroscopy. *Preprint submitted to Remote Sensing of Environment (2020)*.
- [67] R. Widenhorn, M. M. Blouke, A. Weber, A. Rest, and E. Bodegom. Temperature dependence of dark current in a CCD. *Sensors and Camera Systems for Scientific, Industrial, and Digital Photography Applications III*, 4669(April):193–201, 2002.
- [68] E. Woolliams, A. Hueni, and J. Gorroño. Uncertainty analysis for earth observation (Instrument calibration). *MetEOC project (EMRP)*, 01:1–129, 2014.
- [69] H. W. Yoon, D. W. Allen, and R. D. Saunders. Methods to reduce the size-of-source effect in radiometers. *Metrologia*, 42(2):89–96, 2005.

# Appendices

## A Correction Model: Individual Wavelength Ranges

### A.1 Fitted Mean Quadratic Functions of the Correction Model

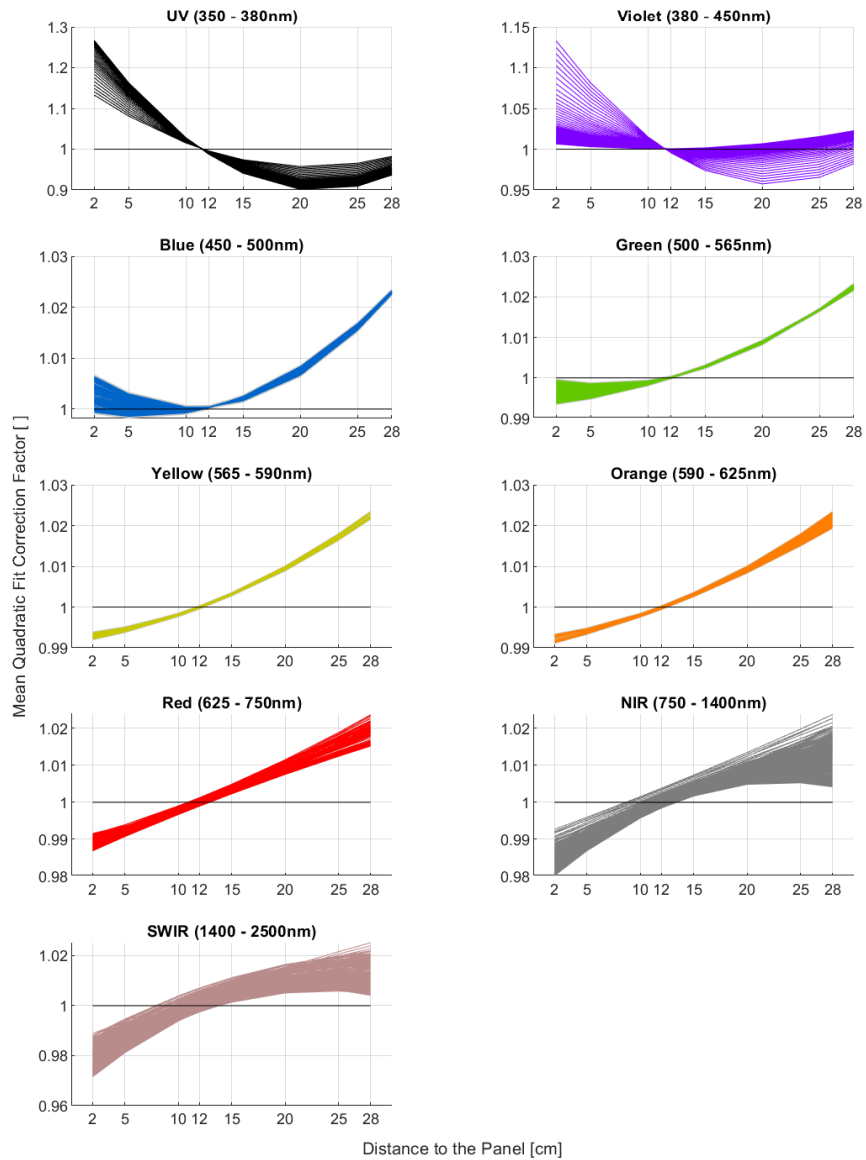


Figure 26: The mean quadratic functions of the correction model per wavelength range accompanied by their *combined standard uncertainty*.

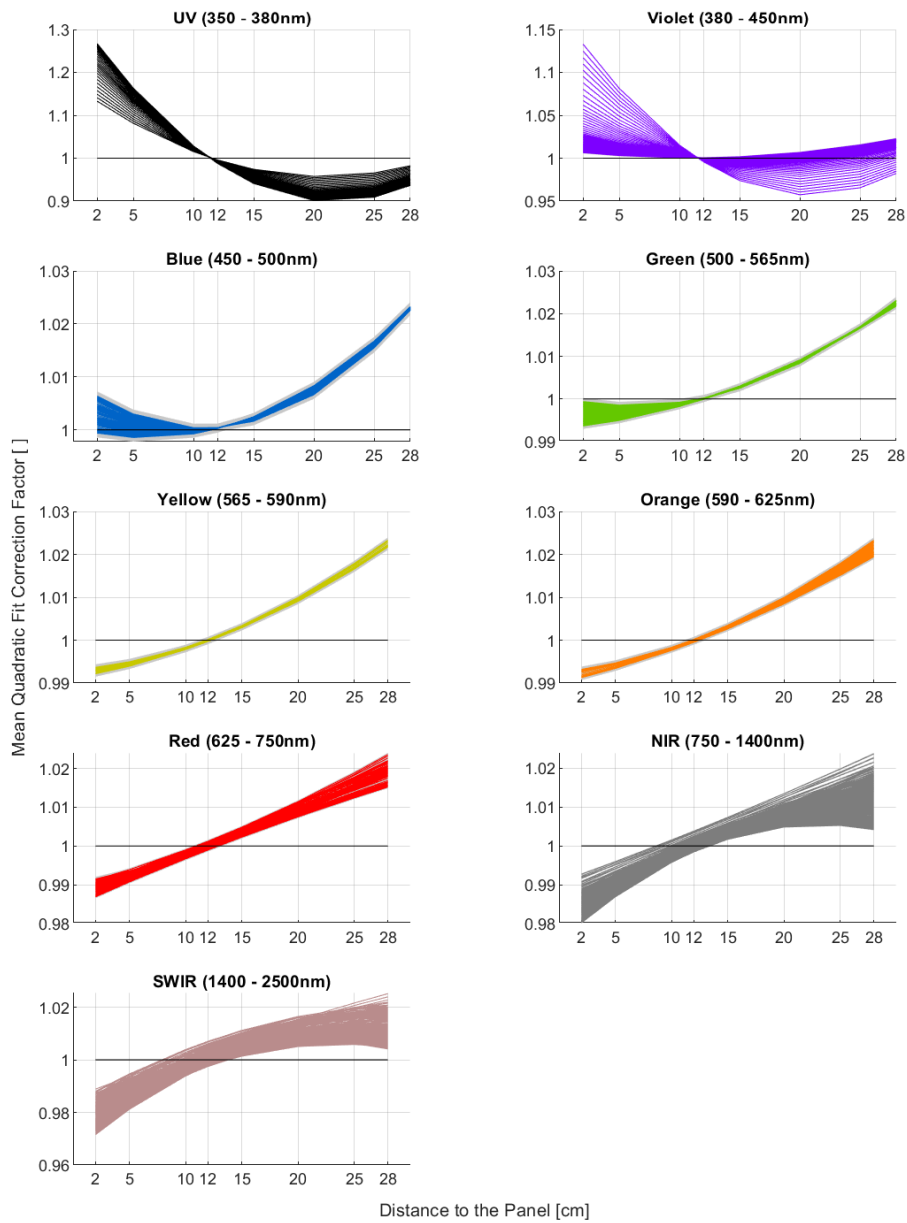


Figure 27: The mean quadratic functions of the correction model per wavelength range accompanied by their *expanded uncertainty*.

## A.2 Mean *Monte Carlo* Values

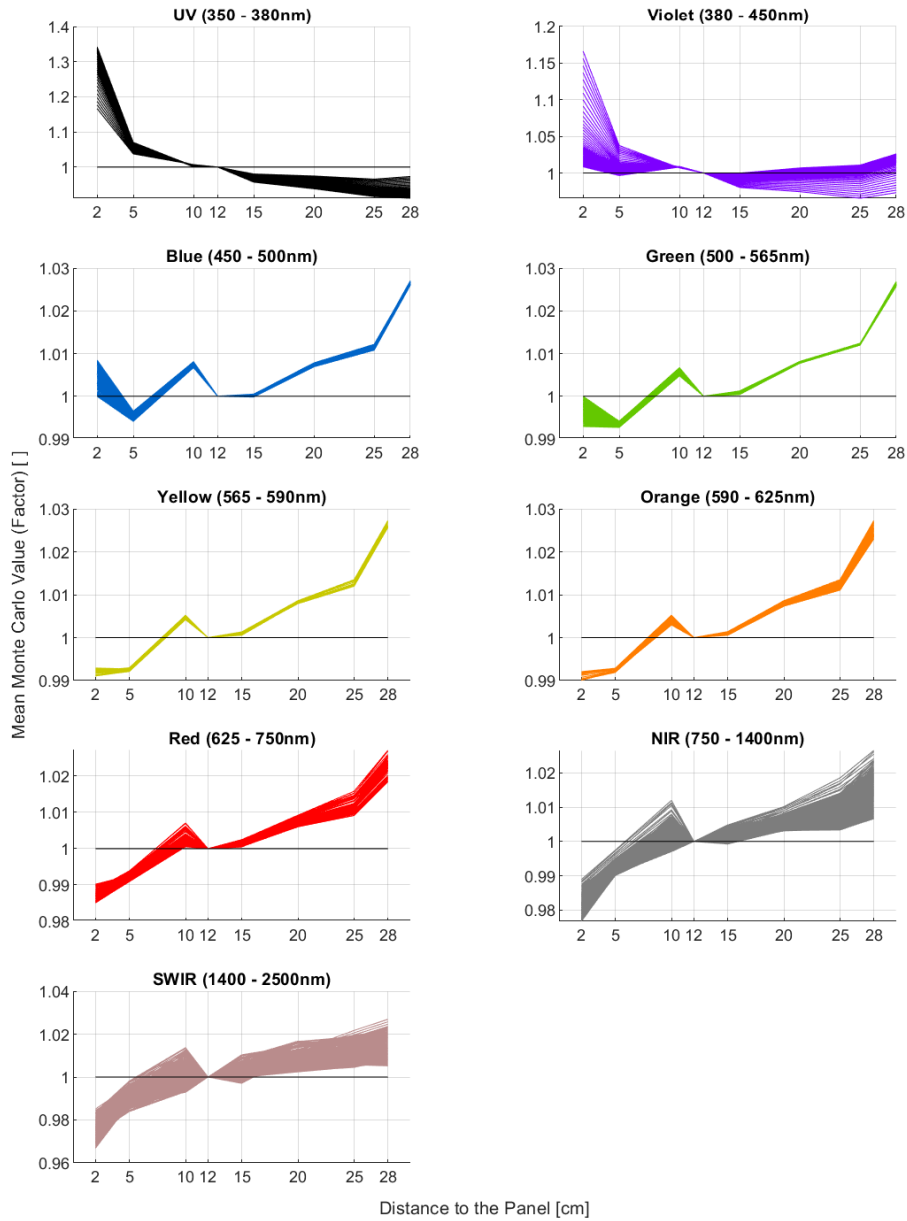


Figure 28: The mean *Monte Carlo* values to which the functions per wavelength range were fitted.



### A.3 Residuals (Correction Model)

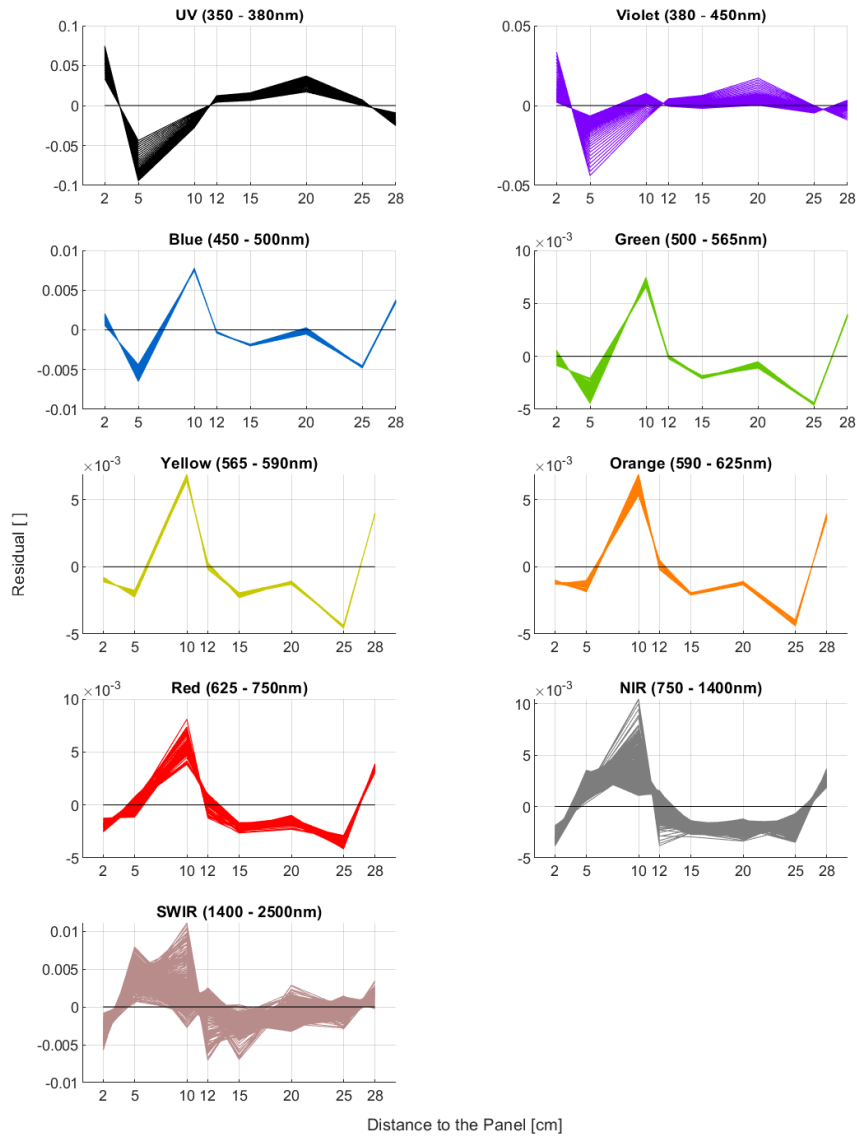


Figure 29: The residuals (difference between the mean quadratic fits of the correction model and the mean *Monte Carlo* values).

## B Uncertainty Model: Individual Wavelength Ranges

### B.1 Fitted Mean Quadratic Functions of the Uncertainty Model

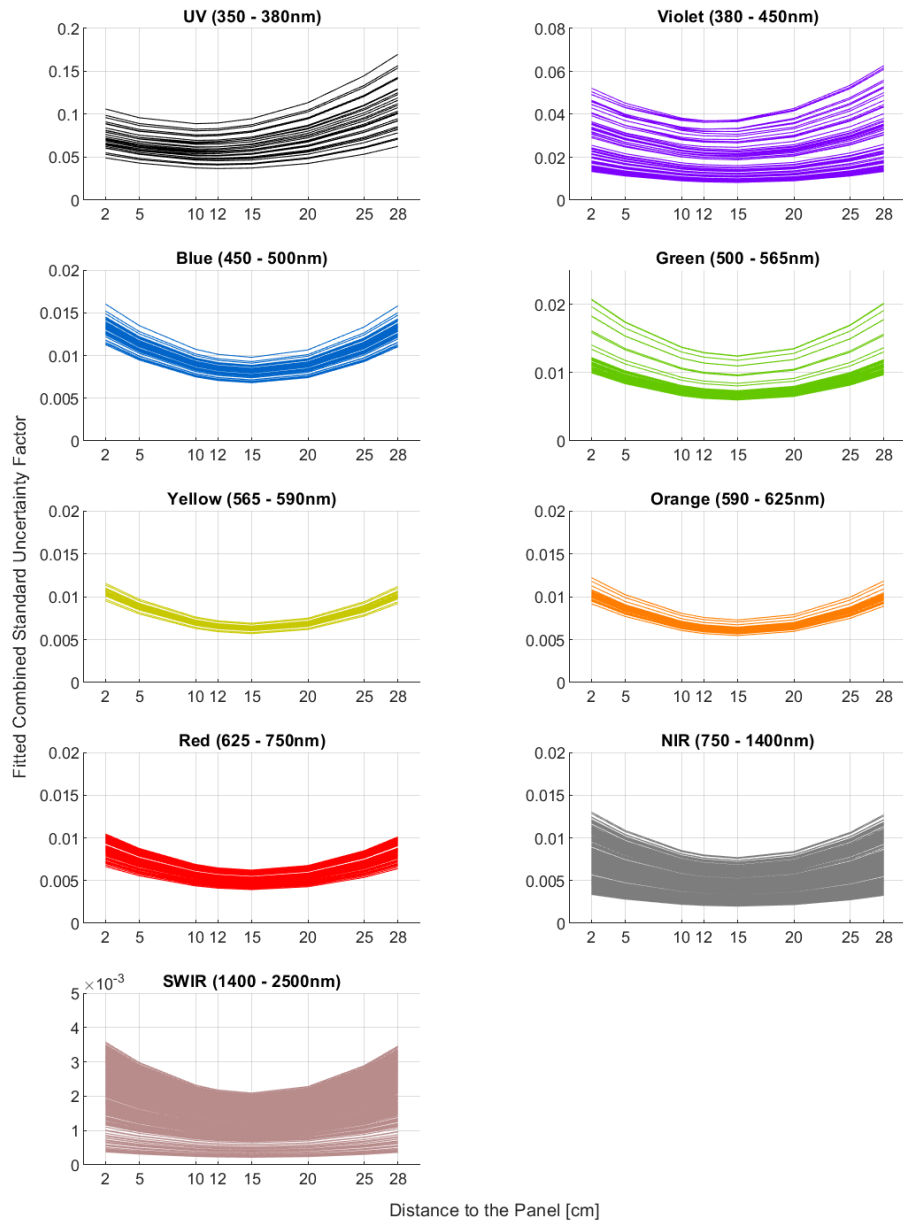


Figure 30: The mean quadratic functions of the uncertainty model per wavelength range.

## B.2 Combined Standard Uncertainty Values for the Initial Eight Distances

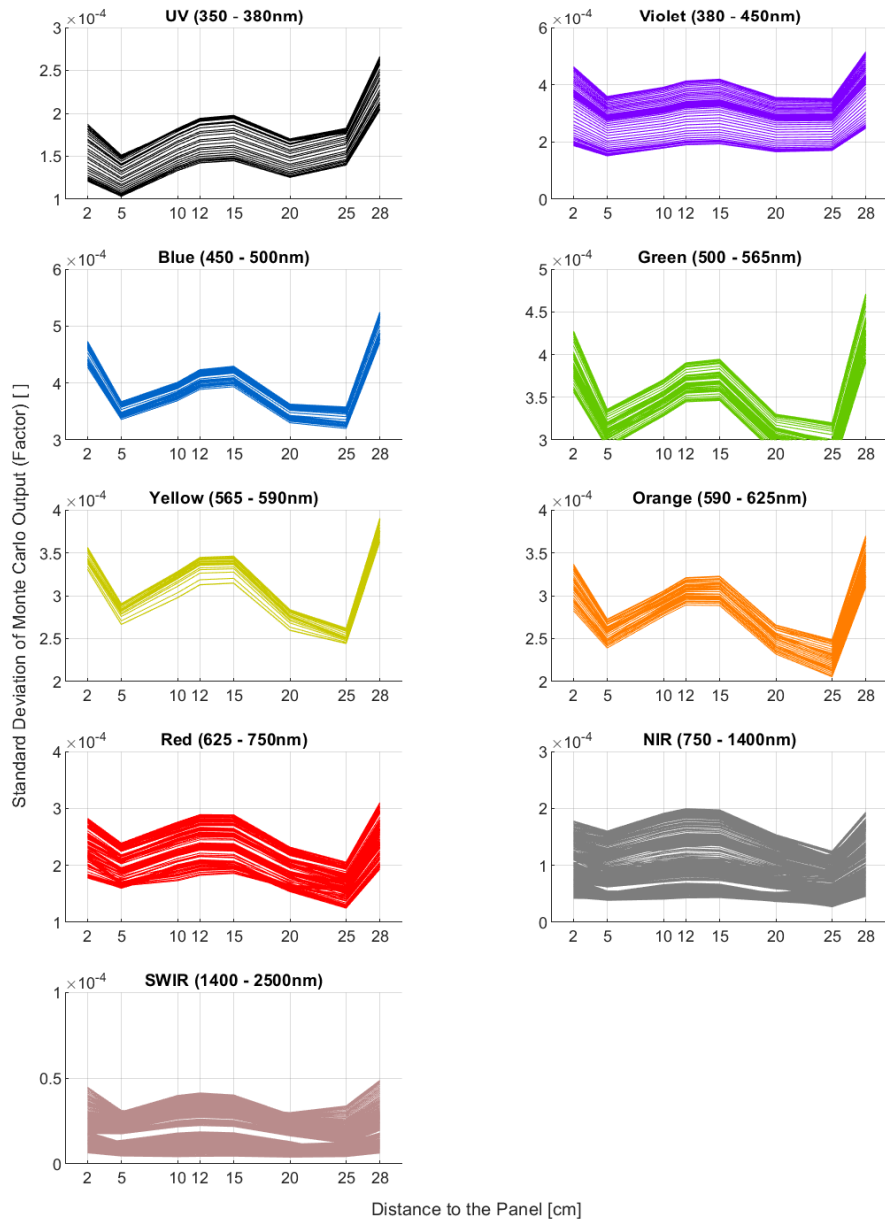


Figure 31: The initial eight *combined standard uncertainty* values to which the functions per wavelength range were fitted.

### B.3 Residuals (Uncertainty Model)

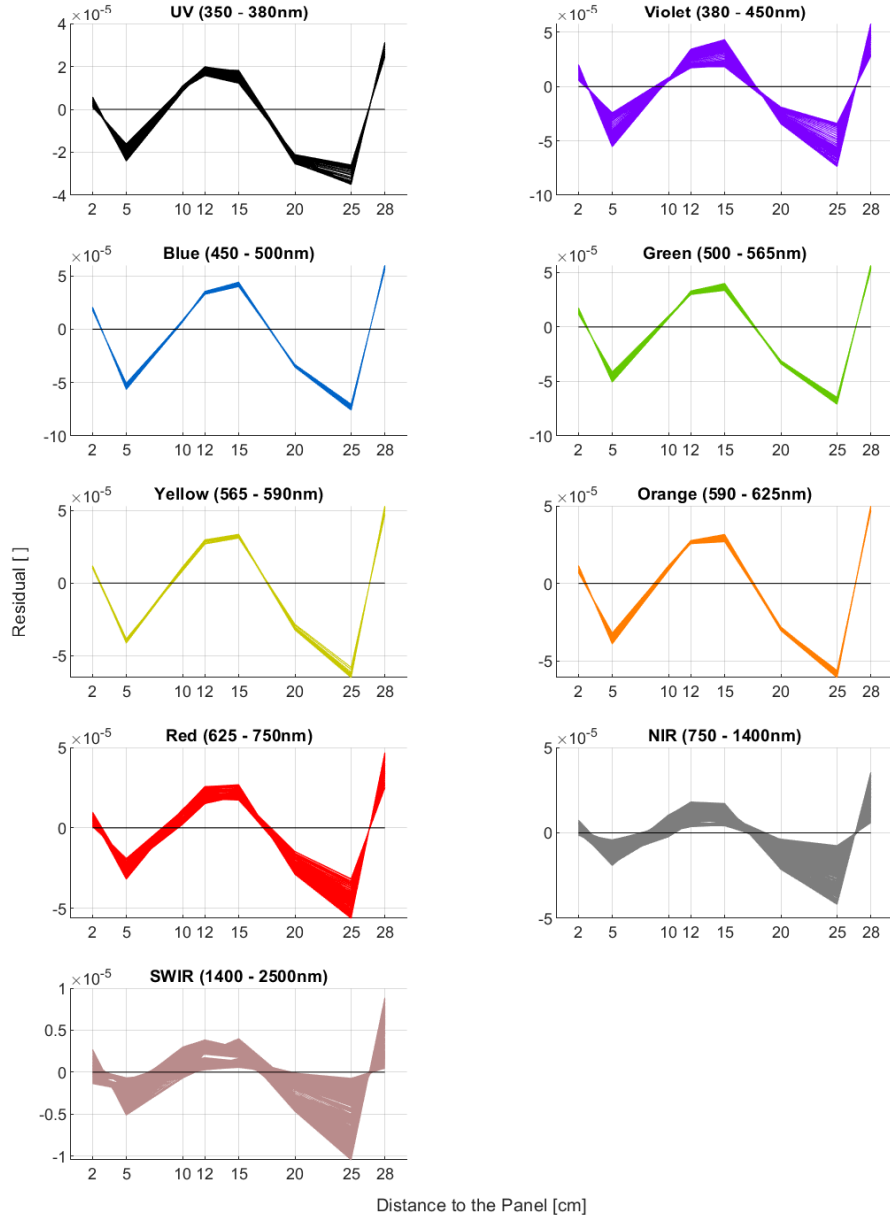


Figure 32: The residuals (difference between the mean quadratic fits of the uncertainty model and the initial eight *combined standard uncertainty* values).

## C Conducted Experiments

This part of the appendix presents the description of all experiments that were carried out and mentioned in Section 2.2 but not analysed. The procedure for performing the experiments is shown.

### C.1 Tilted Versus Levelled Reference Panel

2. *Measurements were carried out for a comparison of the measured spectral radiances on an inclined reference panel versus a levelled panel.*

#### Experimental Procedure

This experiment was conducted on the 13<sup>th</sup> September 2020, a day that offered sunny conditions and a blue sky with no formations of individual clouds, but generally a lot of haze in the atmosphere. The maximum temperature on this day was 26°C (Zurich Fluntern weather station, N 47.37794, E 8.56575 [45]) and the location where the experiment was performed was the standard location: the roof of building Y25 of the *University of Zurich's* Irchel Campus (N 47.396759, E 8.549472). The standard installation of the reference setup was set up: The *ASD FieldSpec 4 #18130* was warmed up for at least one hour before the first use as the reference instrument. The usual setup was applied (see Section 2.4). For the experimental setup, a second tripod was installed approximately three metres away from the reference installation. The *ASD FieldSpec 3 #16007* was also properly warmed up and installed on a similar setup to the reference setup, consisting of a black fixing plate mounted on a tripod. The fixing plate served as a support surface for the white reference panel. This installation was mounted in a way that the surface of the reference panel, when levelled, hence perpendicular to the force of gravity, was at a height of 100 cm  $\pm$ 0.1 cm. The fibre optic cable was fed into a pistol grip which was screwed to a horizontal rod. This rod was in turn attached to a vertical rod screwed into the black mounting plate. The two shiny rods were covered with a black tarpaulin material to eliminate possible unwanted reflectances. The distance of the fibre optic tip to the levelled panel was 12 cm (default distance), pointing nadir and to the centre of the white reference panel.

Before the actual experiment started, a cross-calibration of the instruments and reference panels was performed. Both fibre optic cables of the two instruments were fed into the fibre holder to project a very similar *FOV*. Thirty (x25 internal averages) readings of the white reference panel used with the reference setup were acquired simultaneously with both field spectroradiometers. The white reference panel used with the reference setup was exchanged with the white reference panel used in the experimental measurements and further thirty (x25 internal averages) spectra were collected simultaneously with both field spectroradiometers. After the cross-calibration, the experimental measurements began: in a levelled initial position (perpendicular to the force of gravity (0°)), a first thirty readings (x25 internal averages) of the experimental *Spectralon* panel were acquired.

Further, four positions were defined to test the influence of a tilted white reference panel (see Fig. 33). These four positions were determined with respect to the angle of the sun: the first state was a tilt of the panel towards the sun. The second state, away from the sun, the third away from the pistol grip and the fourth and last position towards the pistol grip. Measurements were taken at different angles for all four positions: inclinations of 5, 10, 15, 20 and 25° were realised. For each inclination (and position), another thirty (x25 internal averages) measurements were collected. Due to the limited mobility of the rods,

the pistol grip did not always point nadir, but always to the reference panel. However, wherever possible, the pistol grip was oriented towards nadir. Once all acquisitions were carried out for all four directions and the five different angles, another cross-calibration was performed. This was done in the same way as the cross-calibration before the experimental measurements. Throughout the experimental period, continuous reference measurements were always carried out.

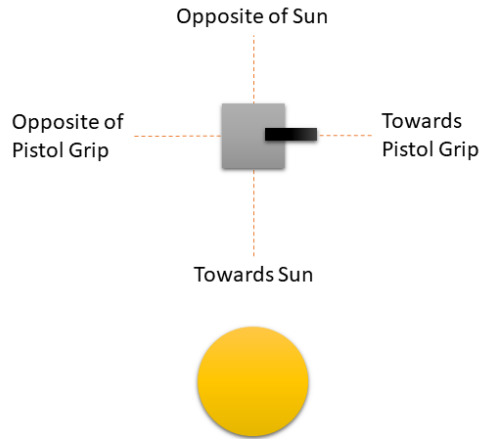


Figure 33: A sketch of the experiment investigating potential differences between a tilted and a levelled reference panel.

## C.2 Distance of the Operator to the Panel

3. An experiment was conducted on the operator’s influence in terms of the distance to the white reference panel.

### Experimental Procedure

This experiment was performed twice, on the 5<sup>th</sup> and the 6<sup>th</sup> of August 2020. The environmental conditions for the measurements were favourable in both cases: a blue, clear sky with a maximum temperature of 22.8°C and 25.8°C respectively (Zurich Fluntern weather station, N 47.37794, E 8.56575 [45]). Occasional haze appeared over the course of the day, which dissipated within a few minutes. The location where the experiment was performed was once more the roof of building Y25 (Irchel Campus, *University of Zurich*, N 47.396759, E 8.549472). The reference setup corresponded to the default setup (see Section 2.4) and the experimental setup was the same as used for the experiment investigating the distance of the fibre optic tip to the panel (see Section 3) for both measurement days. Once more, cross-calibration measurements were conducted before and after the experimental measurements applying the same procedure as for the two previously presented experiments. For the experimental measurements, the height of the fibre optic tip above the panel was adjusted to the default height of 12 cm above the panel, using the scale already written on the rod to create the same circumstances as the default setup. Both instruments (*ASD FieldSpec 3 #16007* and *ASD FieldSpec 4 #18130* respectively *ASD FieldSpec 4 Hi-Res #18739* instead of *#18130* for the 6<sup>th</sup> of August) were warmed up for two hours prior to the experimental measurements. Continuous reference measurements were always acquired during the entire experimental time period.

Data were collected for the two positions that were perpendicular to the solar principal plane. The first position was the operator standing in the East and the second position was opposite the first position, hence in the West. The first position was also the side of the panel at which the poles of the pistol grip appliance were attached (see Fig. 34). Spectral data were collected at eight different distances to the panel per perpendicular position. The greatest distance from the centre of the panel was 200 cm. Further, the distances were decreased in steps of 25 cm until the distance to the panel was 25 cm (see Table 7). The distance accuracy is +/- 5 cm with the centre of the operator’s foot approximately at the distance mark on the ground.

|                               |     |     |     |     |     |    |    |    |
|-------------------------------|-----|-----|-----|-----|-----|----|----|----|
| Distance to panel centre [cm] | 200 | 175 | 150 | 125 | 100 | 75 | 50 | 25 |
|-------------------------------|-----|-----|-----|-----|-----|----|----|----|

Table 7: The different distances to the panel at which measurements were collected.

The operator who conducted the experiment was 170 cm tall and wore a dark blue jumper. For each of the eight different distances, a measurement series of thirty spectra (x25 internal averages) was collected. The test person held the laptop close to the body and always on the side facing away from the sun to execute the measurement command. Hence, for the East position the laptop was held in the right hand and for the West position in the left hand. This procedure was applied for both positions.

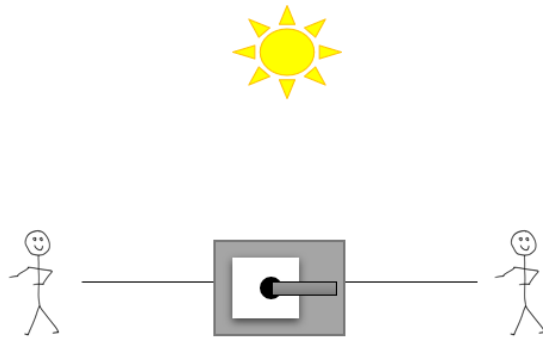


Figure 34: A sketch of the experiment that investigates potential interference effects when the operator stands in close proximity to the reference panel.



### C.3 Position of the Operator in Relation to the Sun

4. The potential influence on the spectral measurements due to the position of the operator in relation to the sun was investigated.

#### Experimental Procedure

The experiment was performed on the 6<sup>th</sup> of August 2020 on the roof of building Y25 of the *University of Zurich's* Irchel Campus (N 47.396759, E 8.549472). The weather during the experiment was stable and sunny with blue skies. Occasionally there was a slight haze, but it dissipated within seconds to a few minutes. The air temperature was approx. 25.8°C at maximum (Zurich Fluntern weather station, N 47.37794, E 8.56575 [45]).

The two setups consisted of the same installations as used for the experiment in the previous section (Section C.2). Hence, the default setup (see Section 2.4) was used for the reference measurements and the setup with the pistol grip attached to the pole was used for the experiment setup. For the reference measurements the *ASD FieldSpec 4 Hi-Res #18739* was used and for the experimental measurements it was once more the *ASD FieldSpec 3 #16007*. Both instruments were warmed up for at least one hour in advance. The setups were installed at a distance of about three metres from each other. As usual, cross-calibration measurements were conducted before and after the experimental measurements by simultaneously acquiring spectra with both instruments. Hence, a first data collection was obtained with the panel used with the reference setup and further with the one used with the experimental setup. The experimental data acquisition was conducted as follows: three measurements were conducted for each cardinal direction and for the four intercardinal directions. The first set of data was collected at a distance of 100 cm to the centre of the panel ( $\pm 5$  cm), then 50 cm ( $\pm 5$  cm) and 25 cm ( $\pm 5$  cm). The operator (hence, the test subject) wore a dark blue jumper and carried the laptop at the side, always using the hand operating the laptop facing away from the sun. The order of the measurement positions is shown in the drawing below (Fig. 35).

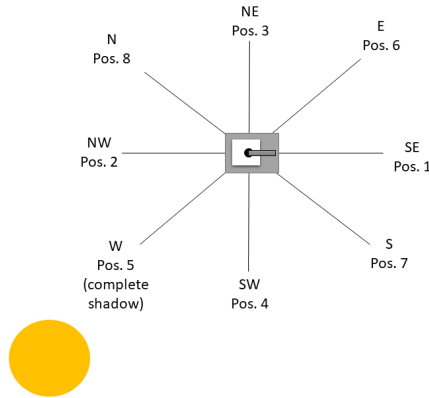


Figure 35: A sketch of all the operator's cardinal and intercardinal positions where the measurements were obtained, together with the azimuth position of the sun at that time.

For each of the three different distances per position, 30 spectra (x25 internal averages) were collected. At position 5 (see Fig. 35), the test person's shadow covered the panel almost completely (~90%) at a distance of 50 cm and completely at a distance of 25 cm. Continuous reference measurements were acquired during the entire measurement period.

## C.4 Rest vs. Free-Hand Operating

5. Data were collected to compare the use of a rest for the data acquisition versus holding the pistol grip containing fibre optic cable by hand.

### Experimental Procedure

This experiment was conducted once on the 4<sup>th</sup> of September 2020 as well as on the 9<sup>th</sup> of September 2020. To maintain consistency, the usual experiment location was used, hence the roof of building Y25 of the *University of Zurich's* Irchel Campus (N 47.396759, E 8.549472). The weather conditions were favourable in both cases. For the 4<sup>th</sup> of September, it was a sunny day with blue skies and some small clouds on the horizon. No haze was observed. The same conditions applied to the 9<sup>th</sup> of September, with the difference that no clouds were reported. However, the visibility decreased slightly towards the horizon. The maximum air temperatures measured at the nearest meteorological station (Zurich Fluntern weather station, N 47.37794, E 8.56575 [45]) were 26.2°C and 25.2°C respectively. Once more, the *ASD FieldSpec 4 #18130* was used for the control measurements and the *ASD FieldSpec 3 #16007* for the experimental measurements. Both instruments were warmed up for at least one hour before the first measurement was conducted. The following preparations were made: An installation of the default setup (see Section 2.4) was prepared for the reference measurements, as well as a second setup consisting of a self-designed appliance (see Fig. 36) screwed to a tripod serving as the experimental setup. The latter was positioned at a distance of approximately 3 m from the reference setup.



(a) The designed pristine appliance.



(b) The appliance covered with black tarpaulin material and in use for the experimental measurements.

Figure 36: The designed appliance to serve as a rest for the monopod.

The appliance allowed the operator to position a monopod to which the pistol grip containing the fibre optic tip was attached on the angular piece and pointing it nadir to the surface of the white reference panel. The *Spectralon* panel in turn was positioned in the slot provided by the appliance to always maintain the same position and align the pistol grip well above the panel. The monopod was used to provide sufficient distance between the operator and the white reference panel. The distance from the surface of the white

reference panel, positioned in the slot of the appliance, to the ground was once more  $100\text{ cm} \pm 0.1\text{ cm}$ . The entire appliance was levelled perpendicular to the force of gravity with a deviation of  $\pm 1^\circ$ . The material used for the designed appliance was a very shiny aluminium. To prevent this material from reflecting unwanted radiation into the sensor aperture, the entire appliance was covered with black tarpaulin. As usual, in order to conduct the experimental measurements, a cross-calibration of the two instruments and reference panels was first performed. The reference setup acquired data throughout the acquisition of the experimental measurements. To simulate a procedure closely resembling an acquisition in the field, a target in the form of a black tarpaulin stretched on a 1x2m wooden frame was placed at a distance of approximately 1.5m from the experimental setup.

The experiment took place as follows: One complete data set consisted of a series of measurements in which the monopod was operated hand-held and a series of measurements in which the rest for the monopod was used. This means that in the first case, five (x25 internal averages) white reference measurements were obtained where the operator was standing perpendicular to the solar principal plane and operating the fibre optic cable from a distance using the monopod. Operating hand-held implies trying to point the tip nadir at an appropriate height (trying to reach 12cm) above the white reference panel without using the rest (the latter was removed for this purpose). Furthermore, fifteen (x25 internal averages) measurements of the target (the black tarpaulin) were collected (hand-held). As a last step, again five (x25 internal averages) measurements of the *Spectralon* panel were once more acquired, applying the same procedure as before.

For the second part of one data set, the same procedure was applied, this time using the rest of the appliance. Hence, the monopod was placed in the angular piece of the rest, stabilising the pistol grip in its vertical axis as well as in the yaw and the pitch axis and to some extent in the horizontal axis. Only the roll axis remains to be unstabilised. The pistol grip was pointed nadir at the centre of the white reference panel.

This procedure was applied a total of six times, resulting in six sets of data, with once a hand-held series of measurement and once a series of measurements using the rest.

After the experimental measurement series, the second cross-calibration of the two panels and instruments was conducted.

## C.5 Ideal Number of Target Measurements

6. An experiment on the ideal number of target measurements to be obtained was carried out.

### Experimental Procedure

A first data collection of this experiment was conducted on the 14<sup>th</sup> of September 2020 on a sunny day with blue sky and possibly some haze in the atmosphere. The maximum air temperature measured at the station in Fluntern on this day was 28.3°C [45]. A second series of measurements of this experiment was conducted on the 15<sup>th</sup> of September 2020. On this day, the maximum temperature reached 28.5°C. The atmosphere showed near perfect conditions with blue skies, a cloud coverage of zero percent as well as no haze was observed. For both measurement acquisitions the usual location was chosen: the roof of the building Y25 of the *University of Zurich's* Irchel Campus (N 47.396759, E 8.549472). The usual reference setup was installed in its entirety (see Section 2.4): The *ASD FieldSpec 4 #18130* was used as the reference instrument and was properly warmed up for one hour before the first data collection. The instrument for the experiment was once more the *ASD FieldSpec 3 #16007*, which was also warmed up one hour in advance. This combination of instruments was used on both measurement days. For the experimental setup, a second tripod was installed on which a fixing plate was mounted. A rod was screwed into the centre of this black fixing plate, which was coated with a black tarpaulin material to prevent it from reflecting unwanted radiation. The entire black fixing plate with the rod attached to it was tilted for 90° so that the rod was aligned horizontal (perpendicular to the force of gravity). A pistol grip was attached to the end of the rod with a bubble level integrated at the top of it. The fibre optic tip of the *ASD FieldSpec 3 #16007* was inserted into the pistol grip, which pointed nadir to the ground (see Fig. 37). Two tarpaulins (one grey and one black) with dimensions of 1x2m, were stretched on wooden frames and placed interchangeably under the hovering pistol grip. They served as the targets to be measured and were centred on the ground at a distance of 55 cm  $\pm$  1 cm from the fibre optic tip.



Figure 37: The experimental setup to investigate the matter of the ideal number of target measurements to be obtained.

The measurement procedure was executed as follows: an initial cross-calibration of only the instruments was performed using the reference setup and hence the reference panel (30 spectra, times 25 internal averages, were acquired simultaneously by both spectroradiometers). For this experiment, only one reference panel was needed, since one can use the

same spectra collected during the cross-calibration to calculate the reflectance factors of the target measurements. After the cross-calibration, the spectroradiometer used for the experimental measurements (*ASD FieldSpec 3 #16007*) was moved to the experimental setup and the fibre optic tip was installed in the pistol grip. First, 200 (x25 internal averages) spectra were collected from each of the targets (the grey and the black tarpaulins) performing a static one-point acquisition technique. Since these two measurements took a while, another cross-calibration was then executed on the same white reference panel as used before. Further, a second collection of experimental measurements was conducted, this time consisting of 100 (x25 internal average) hand-held acquisitions of each of the two targets. A random smearing approach was performed as the sampling technique, with the operator standing perpendicular to the solar principal plane and operating the pistol grip using a monopod and as far away as possible. The distance to the tarpaulin was less than 55 cm, always projecting the complete *FOV* on the tarpaulins. As a last step, a post cross-calibration was performed once more, acquiring 30 (x25 internal average) readings of the white reference panel with both ASDs. For both days of the experimental measurement series, reference measurements were continuously obtained with the reference instrument while the experimental measurements were conducted.

## C.6 Measurement Patterns for the Target Acquisition

7. A data collection was carried out on the potential influence on the measurements by applying different acquisition patterns.

### Experimental Procedure

To evaluate different acquisition strategies, a collection of experimental data was obtained on the 15<sup>th</sup> of September 2020. Naturally, the same maximum temperature (28.5°C) was reached and the same favourable conditions of zero percent cloud coverage as well as no haze in the atmosphere prevailed as in the experiment of Section C.5. Once more, the usual location was used for the experiment: the roof of building Y25 of the *University of Zurich's* Irchel Campus (N 47.396759, E 8.549472). The installation of the reference setup was built up as described in Section 2.4. The reference instrument used was once more the *ASD FieldSpec 4 #18130* and the instrument used for the experiments was the *ASD FieldSpec 3 #16007*. Both devices were warmed up one hour in advance. Not much installation was required for the experimental setup. The grey and black tarpaulins stretched on the 1x2m wooden frames as well as the gravel covering the roof served as targets. The white reference panel of the control measurement setup was also used as the pre and post white reference panel of the experimental instrument. Hence, the data collection started with the usual cross-calibration of the two sensors on the one control reference panel by acquiring thirty simultaneous measurements (x25 internal averages).

Three different acquisition methods were applied: a random smearing across the entire target area, a sinusoidal line approach across the entire target area and a static measurement of one same area of the target. For each method and target type (gravel, black and grey tarpaulin), thirty measurements (x25 internal averages) were obtained. The random smearing acquisition was executed by moving the pistol grip (with the fibre optic tip fed in) over the target in a random pattern (as random as a human can). For the sinusoidal line method, the pistol grip was moved in a slalom pattern over the target. The static approach, on the other hand, was performed holding the pistol grip in one location over the target trying not to move. All acquisition techniques were executed with the operator standing perpendicular to the solar principal plane and operating the pistol grip with an outstretched arm. The attempt was made to maintain a distance of 55 cm from the fibre optic tip to the target throughout the data acquisition, with the best possible human effort. The different acquisition techniques were performed one target type at a time (hence, first all techniques using the black tarpaulin, then the grey and finally the measurement with the gravel). Between the change of targets, thirty (x25 internal averages) white reference measurements were collected on the control panel with the experimental instrument, accompanied by simultaneous measurements of the control instrument. Hence, these data sets could be used to calculate reflectance factors as well as to serve as cross-calibration measurements. During the acquisition of the experimental measurements, the reference setup continuously collected measurements of the white reference panel. After the last experimental data set was collected, a final cross-calibration of the two spectroradiometers was performed.

## C.7 Warm-Up of the Instrument

8. Data were gathered on potential differences in acquired spectral radiances due to the instrument not being properly warmed up.

### Experimental Procedure

In order to obtain spectral radiance data from the warm-up period of a field spectroradiometer, three instruments conducted continuous spectral radiance measurements under laboratory conditions. All the three instruments listed in Table 2 were used, hence the *ASD FieldSpec 4 #18130*, the *ASD FieldSpec 3 #16007*, as well as the third spectroradiometer the *ASD FieldSpec 4 Hi-Res #18739*. They were set up on a bench in a laboratory with their fibre optic tips inserted into the fibre holder (see Fig. 38). The fibre holder itself was attached to two poles coated with black tarpaulin, which were positioned perpendicular to each other. The whole mount was placed in front of an integrating sphere (*HELIOS Uniform Source System* [36]) manufactured by *Labsphere Inc.*. The system's xenon lamp (*HELIOS XEL - Xenon External Lamp* [36]) served as a stable artificial light source for the measurements. The three spectroradiometers were switched on and the software and instrument were prepared as quickly as possible, which took a total of about 7 min for all three spectroradiometers. The settings were adjusted to an integration time of zero with the usual 25 internal averages per spectrum, which corresponds to the procedure established by *RSL*. As soon as the instruments were prepared, the collection of the data sets began. The *DC* was obtained by default once at the beginning of the measurement because of the change from *DN*s to spectral radiances. For the two *FieldSpec 4* instruments, it was measured continuously over two hours. This complied with the manufacturer's recommendation to warm up the instrument for at least one hour, and also allowed to see how it performed after this warm-up phase (hence, whether there was a point at which it stabilised). In the case of the *FieldSpec 3*, the instrument saturated after approximately 40 min at a number of 679 spectra obtained up to that point. Therefore, the analysis of the warm-up data can only be performed for these 679 spectra for the 3<sup>rd</sup> generation instrument.



Figure 38: The installation of the three field spectroradiometers for the warm-up experiment and the use of the integrating sphere.

## C.8 Ideal Time Frame of Acquisition

*9. Investigations were made on an ideal time frame of an acquisition.*

### Procedure

For this experiment, any of the obtained reference measurements from all the other experiments can be used. Intervals of different lengths (e.g., 30, 25, 20, 15, 10 and 5 min) of pre and post reference measurements can be defined. If the measured values were actual field measurements, target measurements would have been recorded between the pre and post reference measurements. Therefore, interpolation methods can be applied to generate values at hypothetical acquisition times of target measurements. It can hence be investigated what would be an ideal length of interval for a field spectroscopy measurement. Different interpolation methods can also be applied in order to test for the best possible algorithm for this application. The interpolations are further compared to the actual measured spectral radiance values.

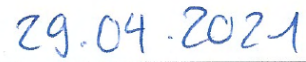


**Personal declaration:**

I hereby declare that the submitted thesis is the result of my own, independent work.  
All external sources are explicitly acknowledged in the thesis.



\_\_\_\_\_  
Author



\_\_\_\_\_  
Date